MICRO MECHANISMS AND MECHANICS OF DUCTILE FRACTURE SEPARATION

Samuel Leonard Creswell

Thesis submitted for the Degree of

Doctor of Philosophy

The University of Aston in Birmingham

OCTOBER 1979

ACKNOWLEDGEMENTS

I would like to take this opportunity to thank all the members of the Department of Metallurgy and Materials of the University of Aston in Birmingham for the help they have given to me during the period of this work. My thanks especially to my supervisor Dr. J. A. Wright for his continual help and encouragement and also to Professor J. T. Barnby and Professor I. L. Dillamore for many helpful discussions.

MICRO MECHANISMS AND MECHANICS OF DUCTILE FRACTURE SEPARATION

Samuel Leonard Creswell

Thesis submitted for the Degree of
Doctor of Philosophy

S U M M A R Y

Ductile fracture occurs as a result of the nucleation, growth and coalescence of voids. The rate at which these processes take place in mild steel has been studied under various states of stress and strain. The void spacings, as described by the parameter Average Nearest Neighbour Distance (A.N.N.D.), and the void sizes have been measured at applied plastic strains ranging from zero to 0.3 true strain. The voids were produced in uniaxially stressed parallel tensile bars, uniaxially stressed single and multiple notched tensile bars, and in three point bend specimens.

The void spacing was found to be a linear function of strain. The variation of spacing with strain under conditions of uniaxial tensile testing is in agreement with the observations made near notch tips once corrections have been made for the differences in strain concentrations. The void growth increases exponentially with the triaxial stress component of the stress state, which is in agreement with the available theoretical predictions, although these predictions were found to give an over-estimation of void growth rates.

It has been demonstrated that the occurence of a ductile fracture is controlled more significantly by the amount of plastic strain than the magnitude of the triaxial component of the stress.

The implications of this conclusion have been discussed in terms of the mechanisms of ductile fracture and the methods used to design against failure.

KEY WORDS:- DUCTILE FRACTURE, VOIDS, TRIAXIAL STRESS,

STRAIN CONCENTRATION, MECHANICAL PROPERTIES.

1. INTRODUCTION

In modern engineering structures and components the tendency to select tougher and more ductile materials has, in general, led to a reduction in the number of catastrophic failures by classical brittle fracture.

As one might expect the use of such materials has not completely solved the problem of premature material failures, e.g. metal separation due to accidental overstressing or tearing along paths of maximum resolved shear stresses.

In these ductile modes of failure, the material parts by internal tearing to form holes, or cavities. When these holes or cavities, have reached a large enough concentration a new surface may easily be formed due to internal rupture in between these cavities, thus giving material separation.

These processes of internal damage may start at various stages of a components life. An example of this is seen when there is a complex stress distribution such as occurs beneath a right angle joint in a fabrication which is subjected to applied stresses only just above its elastic limit. Because of the presence of stress concentrations some of the processes

that may lead to ultimate ductile failure of the component may begin at surprising low levels of applied stress. Ductile failure may be initiated during the fabrication of a component, for instance in the bending or pressing of a plate or sheet of material into its final form. In this case the applied stresses are creating work hardening in the material, and a traditional view is that this improves the strength without any other serious consequences. However materials, such as steels, contain small particles that act as sources of stress concentration around which the first signs of ductile failure may be initiated in the creation of holes or cavities. Thus fabrication of a component can induce regions of permanent damage on a microscopic scale which can grow to a large scale if over a period of time stress relaxation has not occurred.

In some instances fabrication practices call for deliberate overstressing 'or plastic realignment' and although it is the intention of the procedure to preserve the integrity of the structure, the microscopical damage that is an inherent part of the eventual ductile failure can develop in a cumulative fashion during these procedures.

The purpose of this thesis is to study ductile fracture in such a way as to examine each of the microscopical

events that have to take place before metal separation occurs. In particular emphasis will be placed upon studying the fine details of the development of tiny cavities at applied stress levels between the elastic limit and the U.T.S. of the material. The aim is to provide evidence that can help to draw conclusions about the safety of the manufacturing procedures.

2. LITERATURE REVIEW

2.1 Overview

This phenomena, known as ductile fracture, is now generally accepted as being the end result of a process of nucleation, growth and coalescence of voids (1,2).

In general it has been found that these voids are nucleated at interfaces of various kinds, for example between two ductile phases (3), although the most common type of nucleation is between the matrix and a relatively hard inclusion or second phase precipitate (1,4-10).

The concept that voids can be nucleated at inclusions originated with the observations of Tipper (12), although what she and Puttick (11,12) observed would now be called nucleation at macroinclusions, i.e. inclusions $\geq 5\mu m$ diameter. Although these macroinclusions play an important role in the fracture (13,14) they do not generally control the details of the process (13), particularly the size and spacing of the coalesced voids or dimples which are observed on the fracture surface. Rodgers (16) first recognised that the voids formed at macroinclusions need not coalesce, but that

they are frequently linked by sheets of very small voids which form in shear bands between the macroinclusions. This process has been demonstrated by Cox and Low (17) and others (16,18,19).

In its most general form then, ductile fracture can occur as a two step process:-

Nucleation of voids at macroinclusions, followed by the formation of shear bands (containing void sheets) linking up the voids formed at macroinclusions. If there is a large volume fraction of macroinclusions the voids nucleated at them will coalesce (Fig.1) before the second process can occur. If macroinclusions are substantially absent shear band localisation with the associated void sheet formation will dominate the fracture process (Fig.2).

The voids found in the shear bands may themselves have caused the shear band, due to strain softening (20), or the shear band may have formed due to local instabilities and then the voids formed and coalesced within that band (21).

2.2 Homogeneous nucleation of voids

The most commonly proposed alternative to void nucleation at particles is that of vacancy condensation to form voids (26). In a deformed metal the principle sinks for vacancies are dislocations rather than other vacancies (29) so vacancy aggregation will depend critically on experimental variables, e.g. reduced temperature will increase net vacancy production rates primarily because migration to sinks is slower. For this very reason of reduced mobility, the rates of vacancy aggregation and void formation should be similarly slower (29,30). Thus if vacancy nucleation were to be found then it would follow that:-

a) Increasing cleanliness and purity of metal would cause increased ductility due to decreasing particle nucleation up to the point at which vacancy condensation becomes dominant beyond which fracture ductility from hole growth would be roughly independent of purity.

or

b) In very pure metals a reduction in temperature should reduce the incidence of vacancy nucleation of cavities and may cause an increase in ductility should vacancy growth and coalescence take place.

or

c) The mechanical anisotropy expressing prior working history, familiar in engineering materials (31) should be absent.

In practice none of these are found to be the case:-

a) Increased cleanliness leads directly to rupture (by up to 100% R of A) with there being no evidence (30,31) for any vacancy nucleated voids.

b) Reduction in temperature increases void formation and decreases ductility in very pure metals of low flow stress which exhibit rupture at room temperature (30,32), this can be explained by the increase in matrix flow stress with decrease in temperature which overcomes the particle-matrix interfacial bonding energy.

c) Mechanical anisotropy is as well known in pure metals as in engineering ones(31).

All these features are consistent with particle nucleation being the sole process i.e. there is no homogeneous void nucleation from vacancy condensation.

2.3 Small particles in ductile fracture

When shear band localisation and void sheet formation play a major role in ductile fracture the behaviour of the small inclusions or second phase particles ($< 1\mu m$) must be considered. The first question to be posed is how small can such a particle be and still nucleate voids. Voids have been observed (19,22) on particles as small as 50 Å, which is in agreement with the analytical conlusion (4) that particles in the 75 to 100 Å range should be capable of forming voids. Thus void sheets could arise from only a small volume fraction of about 10^{-6}, which would be very difficult to detect even by electron microscopy. If therefore one wishes to demonstrate that in a relatively clean material that inclusions have nucleated all the dimples on a fracture surface the task would be a difficult one. Quantitative demonstrations of this type have to date only been performed for appreciable values of volume fractions (13,23,24,25), also relatively loose bonded particles often cannot be detected on the fracture surface even when they are known to have nucleated voids (2).

The converse is also true, the above comments on purity and particle size indicate that it is unsuitable to conclude either on the basis of purity (26), or on observations at moderate magnification to determing the presence of

particles or their spacing (27,28), that particles are not responsible for void nucleation. Evidence of the size and size distribution of the entire inclusion and second phase particle population and its spatial variation (4) would be required on an exhaustive scale before such a conclusion could be reached.

2.4 Quantitative analysis of ductile fracture

Probably the first quantitative investigation into ductile fracture to be carried out was by Gurland and Plateau in 1963 (5), where they found a relationship between the volume fraction of inclusions (or second phase particles) and the strain to final rupture:-

$$\varepsilon_r = \varepsilon_o + \tfrac{1}{3} \log \left[1 + \tfrac{2}{3} \frac{k_2^2}{k_1^2} \left(\frac{1+f}{f} \right) \right]$$

where

ε_o = nucleation strain

ε_r = strain to rupture

f = volume fraction of inclusions or second phase particles

k_1 and k_2 = constants

i.e. the only variable is volume fraction.

This relationship is represented graphically in Fig.3 together with the results obtained by Edelson and Baldwin (14) from tensile tests on various copper alloys.

Although this analysis is in good agreement with the available practical results (14) it has generally been recognised, as mentioned earlier, that there are three separate events during the formation of a ductile fracture:-

a) Nucleation of Voids

b) Growth of Voids

c) Coalescence of Voids

Each one of which requires its own quantitative analysis and cannot easily be combined with any of the others.

2.5 Nucleation of Voids

For all practical purposes nucleation of voids may be exclusively connected with hard rigid inclusions or second phase particles (1, see section 2.2).

The distribution of particles which may be considered to have formed the final fracture surface (via void nucleation, growth and coalescence) is of obvious interest in the study of ductile fracture. Several recent investigations (51,92) on several different types of material have yielded some interesting results. Burghard (51) noted that in certain low strength aluminium alloys with evenly distributed second phase precipitates of uniform size, voids were initiated at only a few of the precipitate sites. The final fracture then resulting from the growth and coalescence of these few voids. Burghard supported this by the fact that the void sizes on the final fracture surface were well in excess of the particle spacings. Widgery and Knott (92) in their investigations into steel weld metals produced results which pointed to the opposite effect to that observed by Burghard. In that the dimples on the final fracture had closer spacings than the voiding particles in the original matrix. This they

explained by the volume over which a fracture acts i.e. the particles (and their voids) at some considerable distance either side of the fracture plane are involved in the final fracture. From their quantitative observations Widgery and Knott suggested that inclusions which originally resided at a distance of up to six times their diameter from the fracture plane could be directly involved in the formation of the final fracture surface.

In considering these two conflicting pieces of information the basic differences between the materials used must be considered. On the one hand Burghard was using a very ductile material with relatively well bonded particles within it, whilst Widgery and Knott used a material with appreciably less ductility and very loosely bonded void nucleating particles. If these factors are considered together with the observations then the problem reduces more to a question of void nucleation. If there are few voids nucleated then only these few can take part in the fracture but if many voids are nucleated they may be drawn into the final fracture from some considerable distance away from the fracture plane.

Both practical observations and theoretical models show a large amount of variation in their eventual conclusions, particularly with respect to whether or not a particular particle will nucleate a void after a given amount of plastic deformation (i.e. strain).

Inoue and Kinoshita (25) observed void nucleation on spheroidised carbides in steel and concluded that voids were formed in the later stages of deformation (i.e. at large strains), when the stresses around particles would be large. They concluded that the strain to nucleate these voids increased with increases in interparticle spacing. This they explained on the basis of stress relaxation around the carbide particles. They assumed that voids were nucleated at a critical dislocation density so that as the interparticle spacing increased the dislocation density around each particle decreased and thus larger strains would be required to achieve the necessary dislocation density to cause nucleation.

Brindley and Lindley (33) observed long thin grain boundary carbide films in low carbon steels and concluded that there was a significant difference in

the carbide cracking, as a function of applied matrix strain, depending upon the size of the carbides. Of the two size populations examined they found that the thinner carbide films cracked at a lower matrix strain than the larger or thicker ones.

Lindley, Oates and Richards (8,47) studied similar particles to those considered above by Brindley and Lindley (33) and came to virtually the same conclusions with respect to size effects. They also noted that there was a tendency for cracks to be preferentially nucleated in the longer carbides which were oriented with their major axis in the direction of tension. These cracks were also predominantly found towards the centre of these long carbides. Lindley et al. explained these effects by the use of a fibre loading model, this model would give the stress distribution along a particle which is shown in Fig.4a. As the strain in the matrix increases the end effects of the fibre loading model predominate and the stress in the centre of the plate increases until the situation of Fig.4b is reached. This type of stress distribution indicates that there must be an increased chance of the carbides fracturing near the centre of its length, by the mere fact that there is a greater stress

acting in that region, although changes in cross section and internal defects must play a significant and obvious role. They (Lindley et al.) use this model property and observation agreement as the basic proof of their argument but also go on to explain their other observations. The fibre loading mechanism depends upon the macroscopic plastic strain and as the tensile strain is a maxima along the direction of loading, the observed tendency for carbides oriented along the tensile axis to crack more readily is indicated by this model. High aspect ratio particles (i.e. those which are either long or thin) will generate higher stress levels within themselves. Long ones because the maximum stress will be cut off at a later stage (i.e. higher stress level) by the increasing end effects (Fig.4c) and thus have a higher stress acting on their central regions. Thin ones because the fibre loading model is based upon the load acting on the fibre, caused by the surface shearing, which is proportional to the surface area, and as thin films have large surface to cross section ratios the stress acting will be much higher than for a comparatively thick particle.

Thus all of their observations can be explained by the fibre loading model which is put forward.

It is interesting to note that this model gives the apparently odd result that both 'small' (thin) particles and 'large' (long) particles will both be cracked at a comparatively early stage in the deformation of the material.

Broek (34) observed in aluminium alloys that voids initiated late in deformation but also noted that voids were formed at isolated large particles at much lower strains, although it must be noted that these large particles were inclusions and the small particles which later formed voids were precipitates i.e. like was not compared to like. In fact this was probably an observation of initial void nucleation of macrovoids followed by void sheeting to connect these large early formed macrovoids (see section 2.1).

Butcher (35) who looked at copper-oxygen alloys observed that voids were formed both by cracking of the particles and by interface decohesion. On measuring the size distributions he found that the cracked particles had a larger average size than the ones which had failed at the interface and also that the particles that were still bonded had an even smaller average size i.e. an observation of large particles forming voids first. Butcher explained this by considering the stress concentration around a particle

(on a macroscopic scale rather than as a dislocation model). The assumptions that he made were that the bond strength was less than the particles fracture strength and this difference was less than the difference between the tensile stresses at the mid-point and at the ends (the tensile stresses at the mid-point being enhanced by additional shear stresses at the interface). He then plotted these as a function of particle size (Fig.5). As the stresses on the particle increase the diverging lines move up the diagram so that with a large particle the tensile stress of the mid-section will reach the fracture before the end stress reaches the debonding stress, the reverse being true for small particles.

One of the earliest quantitative theoretical models was formulated by Gurland and Plateau (5) who considered a rigid elastic spherical inclusion in an infinite matrix. They used the obvious and simple energy criterion that the stored elastic energy (U) should be greater than the surface energy (s) of the void about to be formed.

Thus they formulated the following relationship for cavity nucleation:-

$$U \geq S$$

$$\frac{(q\sigma)^2}{E} a^3 = \gamma a^2$$

or

$$\sigma_{crit} = \frac{1}{q}\left(\frac{E\gamma}{a}\right)^{1/2}$$

where

σ_{crit}	=	remote stress to nucleate a void
q	=	stress concentration factor
E	=	weighted average of elastic moduli
a	=	diameter of particle

i.e. there is an inverse square root relationship between ease of void formation and size - large particles forming voids first.

This is only applicable to large particles as it only considers a macroscopic stress concentration factor.

Smith and Barnby (36) considered a model of nucleation which involved the detailed consideration of dislocation pile-ups acting on finite barrier of width d, this analysis gave the effective shear stress (τ_ε) required for the cracking of a particle as:-

$$\tau_\varepsilon = \left[\frac{d}{l+d}\right]^{1/2}\left[\frac{2\gamma\mu}{\pi(1-\nu)l}\right]^{1/2}$$

where

γ = surface energy

μ = matrix shear modulus

ν = Poissons' ratio

l = length of pile-up

It is interesting to note that if the barrier is large (i.e. $d \rightarrow 1$) then this reduces to a relationship similar to that derived by Stroh (37) for crack formation from dislocation interactions in a homogeneous body.

Smith and Barnby's relationship is plotted out in Fig.5 where it can be seen that this theory predicts the cracking of small particles at lower values of shear stress than that required to nucleate voids at larger particles.

Thus this theory is in disagreement with the analysis of Gurland and Plateau (5), although it must be noted that the Smith and Barnby theory is involved with the cracking of thin barriers (i.e. long thin particles) whilst the Gurland and Plateau analysis is concerned with spherical particles decohering from the matrix to form voids.

This type of analysis, based on dislocation pile-ups, may also be capable of explaining the effects observed by Lindley et al. (8,47) and explained by them using a fibre loading model. The predominance of the observed carbide plates to crack near to their centre could be due to cross slip around the ends of these plates, to give stress relief and thus similar effects to those described by Lindley et al.

Ashby (38) during his work on the dislocation theory of hardening due to second phase particles discussed a model for the onset of cavitation by the punching out of prismatic dislocation loops from the interface of the particle, thus reducing the local shear stresses, these loops then form reverse pile-ups (Fig.7) and build up increasing interfacial tensile stresses until they overcome the interfacial bonding energy between the particle and the matrix. This work

predicted the following relationship:-

$$\varepsilon_n = \frac{4k\gamma_\omega}{G x b}$$

where G = shear modulus

b = burgers vector

x = particle size

γ_ω = interfacial energy

k = particle spacing

This relationship is plotted in Fig.8 from which it can easily be seen that the strain to void nucleation from a particle varies continuously with the size of that particle, in such a way as larger particles will form voids first.

Tanaka et al. (39) used an energy criterion similar to that of Gurland and Plateau (5) to predict void nucleation at an elastic spherical particle in a plastically deforming matrix under uniaxial tension. They employed Eshelby's solution (40) for stresses and strains in an embedded particle and from this they derived an expression for the critical applied strain to form a void at any one particle.

$$\varepsilon_c \geq \beta\left(\frac{1}{\alpha d}\right)^{1/2}$$

where α = ratio of Young's Modulus of the particle to the matrix (α is >1.0)

β = function containing the stored elastic energy

Tanaka et al. then calculated a stress criterion, using a similar method to Ashby (38), which proved to be independent of particle size. As both of these conditions were considered to be necessary criteria for void formation both must be met, thus when they are both plotted on one graph (Fig.9) it can be seen that in the case of small particles (< 30 nm) even though the tensile stresses on the interface may exceed that stress which is nominally required to form a void, the particle will not form a cavity as there is insufficient stored elastic energy. However, for particles larger than these, stable voids will be formed when the interfacial strength is reached. Thus, although this approach appears to give an inverse dependency of nucleation on particle size, any realistic precipitate or inclusion

(> 30 nm) will not show any dependency on size as the upper condition (stress criterion) must also be met as well as the lower condition (energy).

The major criticism of this work is that it takes no account of plastic relaxation in the matrix.

Brown and Stobbs (41) also used an energy criteria to predict void nucleation, again using Eshelby's solution (40) to calculate the stress distribution at the particle, but in this case extending the analysis to include plastic relaxation in the matrix. They started from the basic concept:-

$$4\pi\mu r^3 \varepsilon_\rho'^{2/3} \geq \tfrac{4}{3}\pi r^2 \gamma$$

Stored elastic energy in the matrix - from Eshelby $\geq$ The interfacial energy of the particle - matrix bond

where
- r = particle radius
- μ = matrix shear modulus
- ε_ρ' = net strain in the particle
- γ = particle matrix interfacial energy

Using these two bounds and including plastic relaxation in the matrix they formulated the following:-

$$\varepsilon_c \geq \frac{3\pi\gamma}{8\alpha^2\mu b}\left(\frac{\alpha^2\varepsilon_p r}{8\pi b}\right)^{1/4}$$

where

b = burgers vector

α = work hardening exponent

ε_p = strain in the matrix

Which on examination only a weak dependency on size, in that smaller particles will form voids first.

Brown and Stobbs, however, concluded that this was against their own observations. Although this being only an energy criteria it is a necessary condition for nucleation and does not consider the exact physical process which will nucleate the voids and which may play an important role in the analysis. If the equation is included, although it reverses the size dependency to agree with their observations that large particles nucleate voids first, the question must be asked whether a mechanistic theory such as that of Ashby (38) be superimposed upon this energy balance to give an inverse size dependency upon voiding.

Kleverbring and Mahrs (42) used a fairly simple dislocation model of highly organised secondary slip caused by the punching out of dislocation loops from the interface of a round particle. These loops form reverse pile-ups and build up increasing interfacial tensile stresses until they reach the interfacial bonding strength of the particle and thus a cavity will be formed.

This analysis gave the following relationship:-

$$\sigma_c = \frac{K \varepsilon r}{b \Omega}$$

or

$$\varepsilon = \frac{\sigma_c b \Omega}{K r}$$

where ε = strain

K = constant

Ω = height of dislocation array

r = particle radius

This result is of course very similar to that obtained by Ashby (38) as the analysis is almost identical, again giving an inverse dependency of nucleation on applied strain.

Masayuki Toya (43) considered a rigid inclusion in an infinite elastic medium, based on Muskhishvilis complex variable method (44). He derived a decohesion criterion which depends upon the central angle subtended by the half length of the crack (or nucleated void). This was a new concept as all previous work was based on complete cavitation of the interface rather than partial decohesion of a spherical particle. For a constant crack shape Toya derived a dependence on particle size which is almost the same as Gurland's (5) and Tanaka's (39) stress criteria.

Toya's criterion:-

$$P_{cr} = \sqrt{\frac{8\mu\,(1+K)\,\gamma}{\pi K\,(1+4\lambda^2)\,\alpha a}}$$

where a = particle diameter

α = angle of decohesion

i.e.

$$P_{cr} \propto \frac{1}{\sqrt{a}}$$

Sundstorm (45), at about the same time as Toya, also considered the concept of crack size. He used a fracture-mechanics approach and derived the critical strain energy release rate (the G of Irwin (46)) for void (or rather crack) formation at the particle matrix interface. By this method Sundstorm obtained an inverse square root relationship between the strain to crack (or cavity) nucleation and the size of the particle:-

$$\varepsilon_{cr} \propto \frac{1}{\sqrt{r}}$$

where ε_{cr} = strain to nucleate a void

r = radius of the particle

This approach employed finite element analysis and because of this is, of course, limited to particles which are large enough for the application of continuum mechanics to be valid. Unlike some of the previous analyses Sundstorm's treatment does not allow for plastic relaxation in the matrix.

These are only a selection of the theories, models and observations available but they nevertheless show the different approaches which have been taken in attempting to quantify the order of nucleation events. On first examination it is difficult to obtain a clear picture of any trend or consistent observations which run through the literature, however the following themes can be extracted:-

a) In long thin plate like particles, such as those observed by Brindley and Lindley (33) and others (8,36,47), the observations indicate the preferential formation of voids at the thinner particles (and also the longer ones i.e. plates with high aspect ratios), with the nucleation of voids happening in larger particles at appreciably higher strains. These observations can be adequately explained by both the fibre loading model of Lindley et al. (8,47) and the dislocation pile-up model of Smith and Barnby, this latter theory being the more acceptable of the two as it can explain all of the

observed phenomena (48) and relies on a detailed microscale model rather than on one involving the continuum mechanics of fibre loading theory.

b) In the case of spheroidal particles the size dependency observed appears to be the reverse of the above, Brown and Stobbs (41) and others (13,35,49) all observed a tendency for the larger particles of the observed groups to form voids first, the only observation against this is by Easterling, Fishmeister and Navara (10) who detected a weak trend of small particles nucleating voids at lower strains. They also observed that widely differing sizes of voiding particles were apparent regardless of the applied strain. So it appears that the bulk of experimental evidence indicates that there is a preference for large spheroidal particles to form voids at an earlier stage in a materials deformation than smaller ones. The theoretical models and predictions are based on either an energy balance criteria or on a 'stress to overcome the bonding energy'

criteria, or on a combination of the two. The predictions of the results obtained in this way range from a weak direct dependency of the strain to nucleate a void on the particle size (Brown and Stobbs (41)) to virtually no size dependency (Tanaka et al. (39)) to the nucleation strain being inversely proportional to the nucleants size (Ashby (38), Kleverbring and Mahrs (42), Toya (43), Gurland and Plateau (5)).

2.6 Effect of interfacial bonding energy

Compared to the effect of size on the order of nucleation events the effect of the interfacial bonding energy (between a voiding particle and the matrix) is fairly clear cut and the results fairly predictable. Throughout all of the previously mentioned theories and models which involve debonding of the particle-matrix interface, all show that an increase in the bond strength leads to an increase in the deformation required to cause cavity nucleation.

The ease with which Rodgers (90) and Puttick (11) observed voiding in Cu alloys may easily be explained by the relatively weak interfacial bond between Cu and its oxide,

whilst in contrast the difficulty experienced by Chin et al. (32) in forming voids in their aluminium alloys may be explained by the good wetting between aluminium and its oxide (91).

This definite effect of bonding energy upon nucleation must always be remembered when considering the nucleation rates from a mixed group of particles. If this effect is not brought into the argument and the effect of more than one group of particles is not removed from the results than a very misleading picture of events may be given.

In considering all of these observations and theories on nucleation it is worthwhile remembering that in any material there will probably be more than one species of particle, and each species will have its own size distribution. An example of this is seen in inclusions and carbides in commercial steel. The inclusions are likely to have a distribution of sizes around a mean diameter in the region of 5 to 10 μm, whilst the carbides will be distributed about a much smaller average diameter ($\approx$ 2 μm). As the majority of the larger inclusions can be considered to be relatively loosely bonded to the matrix (50) this will lead to relatively early decohesion, which may swamp any real size effect and give the apparent result of larger

particles nucleating first. This type of dual nucleant effect has been noted in aluminium alloys by Broek (13) and by Burghard (51).

One other effect which is also worth remembering is the likelyhood of a particle having a surface defect which will cause premature fracture of the particle (9). The larger the particle the greater the chance of it having such a surface defect and thus the greater the chance of it fracturing, i.e. this will again superimpose the effect of large particles cavitating earlier in the process.

2.7 Growth of voids

Strong experimental evidence of the contribution of void growth to ductile fracture comes from many recent optical and electron metallographic studies (1,2,6,14,17,18, 52-62) where the necessity of some void growth from the initial nuclei is required before final metal separation takes place.

The growth of voids, in the context of ductile fracture, has been considered to be a problem in continuum plasticity, i.e. where homogeneity and texture effects are

ignored, as well as factors such as vacancy diffusion and dislocation effects.

The first major growth theory can be attributed to McClintock who formulated a growth theory (63,64), which he then used to predict the fracture of a material by this mechanism (i.e. the voids growing to touch one another).

He (McClintock (63,64)) considered a cylindrical hole with an elliptical cross-section in a material pulled in the direction of its axis, while at the same time being subjected to transverse tensile stresses. He assumed that failure of the material occurred when this hole grew to a point where it touched its neighbour, and thus formed a continuous fracture surface. McClintock assumed a square network of pre-existing holes of initial radius b_o and centre separation $2l_o$, so that the necessary amount of hole growth to cause fracture is given by the critical growth factor $F^f = l_o/b_o$. He then defined a damage parameter $d\eta = \ln F / \ln F^f$ where $F = bl_o/b_o l$ (b and l being the instantaneous hole radii and spacing respectively) and this damage function as a function of imposed equivalent strain ($d\varepsilon$) he gave as:-

$$d\eta = \frac{\sinh\left[(1-n)(\sigma_a+\sigma_b)/2\sigma/\sqrt{3}\right]}{(1-n)\ln F^f}\, d\varepsilon$$

where n = work hardening exponent

$$\sigma = \left(\tfrac{1}{2}\sum(\sigma_i-\sigma_j)^2\right)^{1/2}$$

σ_a and σ_b = transverse stress components

This expression can be integrated to give the strain to failure

$$\varepsilon_f = \frac{(1-n)\ln(l_o/b_o)}{\sinh\left[(1-n)(\sigma_a+\sigma_b)/2\sigma/\sqrt{3}\right]}$$

On examination these expressions show that void growth leading to failure will be much more rapid under conditions of high stress-triaxiality (i.e. as σ_a and σ_b increase in magnitude). Very approximately, then, the growth rate will be exponentially dependent upon the triaxiality of the acting stress state.

(The above interpretation of McClintock's analysis ignores the shape change factor which he introduced but makes little difference to the final solution).

Rice and Tracy's (65) model for void growth is based on the splitting up of an applied strain rate field into two separate parts:-

a) A spherically symmetrical velocity field corresponding to a change in volume of the void, but with no change in shape.

b) A velocity field which changes the void shape but not the volume.

Again it was found that the shape change part of the analysis was negligible in comparison to the volume change and could be ignored without introducing any major errors.

An approximation for their general growth relationship is:-

$$D = \frac{\dot{R}_o}{\dot{\varepsilon} R_o} = 0.568 \sinh\left(3\sigma_m/2\sigma_y\right)$$

where

$\mathcal{D}$	=	void growth rate
$\dot{R}_o$	=	average radial velocity of void
R_o	=	average radius of void
$\dot{\epsilon}$	=	remote strain rate field
σ^∞	=	remote tensile stress
τ_o	=	remote shear stress

This relationship is plotted out in Fig.10 together with their detailed analysis of several flow fields where it can be seen that there is no difference between this simplified approximation and their detailed analysis.

Again this analysis points to a more rapid rate of void growth under conditions of high triaxiality.

Tracy (66) using a similar analysis to Rice and Tracy, except that he considered the interaction between neighbouring voids using finite body analysis as an approximate method, formulated the following rather cumbersome integral:-

$$\frac{\sigma_r(\epsilon)}{\tau} = 2\int_{\frac{\tau_o}{b}\epsilon}^{1} \left[\frac{\gamma}{\sqrt{3}\epsilon}\right]^N \frac{\dot{H}(\epsilon)\ x\ dx}{\sqrt{3\dot{\epsilon}^2 + x^4\dot{H}^2(\epsilon)}}$$

where σ_r = radial stress

$\bar{\tau}$ = yeild stress

N = work hardening index

ϵ = strain

$\dot{H}$ = $\dot{\epsilon} + 2\dot{r}_0/r$

H = $\epsilon + 2\ln(r_0/r)$

x = r_0/r

When solved for the case N = 0.0 the above integral becomes:-

$$\frac{\sigma_r}{\bar{\tau}} \cdot \coth^{-1}\sqrt{\frac{1+3\dot{\epsilon}^2}{\dot{H}(\epsilon)^2}} - \coth^{-1}\sqrt{1+\frac{3\dot{\epsilon}}{\dot{H}(\epsilon)^2}\left(\frac{b}{r_0}\right)^4}$$

Again concluding that an increase in the triaxiality (represented by $\sigma_r/\bar{\tau}$) would give an exponential increase in the void growth rate.

Both McClintock's (63,64) and Tracy's (66) results can be used to predict failure by coalescence by estimating the strain required, under a given stress system, for the voids to grow

sufficiently to touch one another. If the initial void diameters and spacings are assumed to be that of the inclusions or second phase particles which will be responsible for void nucleation and this nucleation is assumed to occur at $\varepsilon_p = 0$, then the strain to failure can be plotted against the initial volume fraction of particles. As can be seen in Fig.11, where these results have been plotted, the void growth to failure theories over estimate the ductility of Edelson and Baldwin's (14) alloys by a considerable amount. If a realistic nucleation criteria were also to be included into these analyses (i.e. nucleation strain $\neq 0.0$) then the over estimation would be even greater. Although it is interesting to note that the general shape of both of these theoretical curves is fairly close to the shape of the envelope of available experimental data.

In using these theories in this way the gross stresses are the only stresses used in the calculation. Hancock and Mackenzie (67) suggested that the influence of the voids on the local stress distribution should be considered as well as the gross stresses, i.e. if there is a stress amplification between two adjacent voids then this stress should be used as the acting stress and there will be an increase in the growth rates of these voids.

Using a stress analysis of the region around a void which was derived by Orr and Brown (68), Hancock and Mackenzie calculated the increase in growth rate of a McClintock (63,64) type void. Fig.12 shows the accelerated void growth rate, which they calculated, as a function of distance from the other void. This plot quite clearly shows that the nearer the two voids become the faster they grow, for a constant gross applied stress.

Although this acceleration can be quite high it will only be of any appreciable amount in the very last stages of void growth when the voids are quite close. As an increase in growth rate in excess of two is required (see Fig.11) this effect on its own cannot fully explain the shortfall of these theories.

2.8 Coalescence of voids

Tracy (66) in his discussion of his own growth theory suggests that the process of growth by the effect of an imposed hydrostatic tension is the appropriate mechanism up to $x/l = 0.6$ to 0.75* but for larger values of x/l

---

* When x is the diameter of the void and l is the centre to centre spacing between adjacent voids i.e. when $x/l = 1.0$ the voids are touching and the material has separated.

(i.e. up to 1.0) the process is one of coalescence rather than growth.

Berg (20) first considered the problem of coalescence in the late 1960's when he considered the problem of dilational plasticity.

He postulated a dilational band of material which has surfaces of zero extension and a zero (or - ve) rate of bulk strain hardening (Fig.13). This strain softening being caused by a decrease in the load carrying capacity of the band, and being brought about by the decrease in net section area due to the growth of voids, i.e. in the simplest terms the ligaments in between voids become plastically unstable in a similar way as a necking tensile bar becomes unstable. Presumably this strain softening will also be increased by stress state softening as the stress system goes from one of plane strain to plane stress, i.e. any constraint forces in the intervoid ligaments will reduce as the width of that ligament decreases thus decreasing the effective flow stress of that section, causing further softening.

Berg represents this mathematically by considering the yield locus of a material containing voids.

In this case the yield locus will not extend to infinity along the axis of positive triaxial stress (when plotted in 3D stress space), as is normally expected under constant volume, but will close at some point along that axis. It is assumed that the cross section of this yield locus (taken on a plane normal to the axis of pure triaxial stress, the π plane) is a circle.

Using the stress deviator S_{ij}, which is related to the stress components σ_{ij} :- *

$$S_{ij} = \sigma_{ij} - \tfrac{1}{3}\,\sigma_{kk}\,\delta_{ij}$$

and the mean triaxial stresses given by:-

$$p = \frac{\sigma_{kk}}{3}$$

---

* Using conventional Cartesian tensor notation δ_{ij} represents the Kronecker delta. Repeated indices indicate summations.

the yield locus can be written in the form

$$S_{ij} S_{ij} + g(p) - K^2 = 0$$

where g, the function of mean triaxiality, also involves the number and distribution of voids.

g(p) can be considered to remain at zero until some finite value of p (pi) when the void population will become significant.

i.e. the yield locus will be

$$S_{ij} S_{ij} - K^2 = 0 \qquad p \leqslant p_i > p_o$$

which is the conventional Von Mises cylinder of radius S_y, and when dilation begins to dominate the system

$$S_{ij} S_{ij} + \frac{K^2(p-p_i)^2}{(p_i - p_o)^2} - K^2 = 0 \qquad p_i \leq p \leq p_o$$

when

p_i = triaxiality beneath which dilation domination may be ignored.

p_o = limit at which pure plastic dilation takes over

According to this last equation the classical Von Mises yield cylinder is terminated by an elliptical cap (Fig.14).

This is only a rough approximation as the character of the yield locus of a particle containing material may change rather strongly when a larger number of these particles are no longer attached to the matrix but are in the centre of voids which have effectively replaced them.

Thus Berg derives a first model for dilational plastic yielding.

Using a much simpler model of load instability Thomason (69) considered the possible instability of a square array of cavities as shown in Fig. 15. This array he considered to be subjected to stresses σ_x and σ_y with an all round hydrostatic pressure P.

He described σ_n , the stress to cause internal necking, by considering a constant volume velocity field for the configuration shown in Fig. 15, and applying lowest energy criteria to give a relationship between σ_n and a/b (a function of the cavity spacing). This relationship is shown in Fig.16 where it can be seen that σ_n rapidly drops in value with the initial increase in a/b and then levels off at about a/b = 1.0.

Thus the stress to cause internal necking between cavities may be greater or smaller than the flow stress depending upon the value of a/b:-

Load to deform one element

$$Lu = \sigma_z \, \delta x$$

Load to cause necking in one row

$$L_n = \sigma_n (\delta x - n\omega) + P\delta x$$

Uniform flow will continue until $L_n < L_u$

i.e.

$$\sigma_n (\delta x - n\omega) + P\delta x < \sigma_z \delta x$$

or

$$\sigma_n (1 - \sqrt{V_f}) + P < \sigma_z$$

as

$$V_f = \left(\frac{n\omega}{\delta x}\right)\left(\frac{ny}{\delta y}\right) = \left(\frac{n\omega}{\delta x}\right)^2$$

From Von Mises

$$\sigma_z = 2K + \sigma_x$$

thus we have a criteria for instability

$$\frac{\sigma_n}{2K}\left(1-\sqrt{v_f}\right) + \frac{P}{2K} < \frac{\sigma_x}{2K} + 1$$

When the above criteria for coalescence of cavities is not met uniform flow will continue. The changing geometry of the matrix between the cavities, for this particular model, is given by:-

$$\frac{a}{b} = \exp\left(2\varepsilon_z\right)\sqrt{v_f} \Big/ \left(1-\sqrt{v_f}\right)$$

The matrix will deform according to this relationship until the value of σ_n (as defined by a/b in Fig.16) falls to a sufficient level for the above instability criteria to become valid.

Thomason plotted the strain to instability in the Z direction (ε_z), as defined by producing a sufficient value of a/b to satisfy the instability criteria via σ_n (Fig.16), against the initial volume fraction of cavities. His results for P = 0 are shown in Fig.17. This plot also shows the effect of transverse stresses where a marked drop in ductility can be seen as the hydrostatic tension increases (i.e. σ_∞ changes from -3K/4 to K/2).

Thus Thomason comes to the same general conlusion as Tracy (66) and Berg (20) in that the growth is terminated at some value of cavity separation around x/l = .6 to .75, and the voids then coalesce in a single void sheet to give final failure.

Hancock (70) attempted to define flow localisation by considering the problem 'in reverse' i.e. he derived the required conditions for localisation by imposing the required strain increments on a single cylindrical void (Fig.18) and then calculated the ncessary stress state to obtain these strains.

He derived the radial and axial stresses as:-

$$\sigma_r = \int_A^R \frac{2}{3} \frac{(\varepsilon_\theta - \varepsilon_r)}{\varepsilon} \bar{\sigma} \, d \ln R$$

$$\sigma_z = \frac{2}{3} \frac{(\varepsilon_z - \varepsilon_\theta)}{\bar{\varepsilon}} \bar{\sigma} + \sigma_r$$

Investigating these equations iteratively Hancock derived the strains to reach a radial load maxima. This maxima is plotted out in Fi.g19 as a function of volume fraction of holes. Assuming that a radial load maxima corresponds to the onset of flow localisation, this curve again shows that at some finite stage in hole growth the process of flow localisation, instability, dilational banding or whatever name is chosen, becomes dominant and, on a macro scale, terminates the ductility of the material.

The above theories are based on the critical applied load to cause localisation, which may be considered fundamentally unsound as this is only a necessary condition for localisation and not a criteria.

Thomason (71) rather than proving instability devised a criteria for the limit of stability using Hills (72) general theory of uniqueness and stability in rigid-plastic solids. This stability Thomason represented by a three dimensional principal stress construction based on the equivalence between virtual modes of void coalescence and dilational plasticity. The element enclosing the incipient ductile fracture surface is regarded as undergoing a discontinuous transformation from incompressible plastic to dilational plastic yielding.

This differs fundamentally from Bergs (20) analysis in that his (Bergs) analysis was concerned with establishing a smooth development of the yield locus from incompressible plastic to istropic dilational yielding within defined bands. Whilst in contrast this work Thomason (71) is concerned with the instantaneous development of an isotropic mode of void coalescence which is not confined to characteristic surfaces of the existing plastic field.

Thomason started from Hills basic stability theorem in that, for any small displacement from the existing equilibrium state, the internal energy stored or dissipated (I) should exceed the work done on the body by the external loads (E).

$$I - E > 0.0$$

The first order expression for I and E in a virtual mode of void coalescence V_1^{lc} of time increment δt are given by:-

$$I = F_1^{lc} V_1^{lc} X_2 \quad \delta t$$

$$E = F_1 V_1^{lc} X_2 \quad \delta t$$

where F_1^{lc} is the traction to operate the virtual mode (see Fig.20)

F_1 is the equilibrium traction and is completely discordant with F_1^{lc}

Substituting the above into Hills basic equilibrium equation we obtain for stability:-

$$(F_1^{lc} - F_1)V_1^{lc} > 0.0$$

Although the virtual mode of void coalescence differed widely from the stable mode of plastic flow, this stable flow can change the voids geometry and spacing (63,64,65,66)

so that F_1^{lc} reduces to the same magnitude as F_1 and stability has broken down, giving way to fracture by void coalescence.

To derive a workable value of F_1^{lc} Thomason (73) considered the probable slip line field in between two adjacent voids (Fig.21). By using the Rieman method of integration he determined the mean tractions (F_1^{lc}) on the element in a mode of void coalescence, thus obtaining workable values of F_1^{lc} for various void geometries. These results are shown in Fig.22 where they are plotted against b/w (Fig.21) for various values of a/b. This shows a rapid drop in F_1^{lc} with an initial increase in b/w and then a levelling off of the curve when the value of F_1^{lc} is near the flow stress.

To clarify the model Thomason considered the above criteria with respect to a simplified two dimensional model when the stability criteria reduces to:-

$$(\sigma_1^{lc} - \sigma_1)\ \dot{\varepsilon}_1^{lc} > 0.0$$

where σ_1 = stable maximum principle stress ($\equiv F_1$)

σ_1^{lc} = dilational element of the principle stress ($\equiv F_1^{lc}$)

$\dot{\varepsilon}_1^{ic}$ = dilational element of the principal strain rate

i.e. for fracture to occur

$$(\sigma_1^{ic} - \sigma_1)\,\dot{\varepsilon}_1^{ic} = 0.0$$

This relationship may be equated back to three dimensions as

$$(\sigma_i^{ic} - \sigma_i)\,\dot{\varepsilon}_i^{ic} = 0.0$$

(for fracture)

(i = 1,2,3)

By the assumption that during dilation there is only one non zero principal strain rate component ($\dot{\varepsilon}_1^{ic}$) it is implied that the dilational yield surface at the point of instability is in the form of a plane of the form :-

$$f_o^{ic} = (\sigma_1 - \sigma_i^{ic}) = 0.0$$

This plane having outward normals parallel to the σ_1 axis.

This plane, together with the yield locus, can be plotted in three dimensional principal stress space to give a graphical representation of the stability/instability discontinuity (Fig.23).

The effect of different void volume fractions (or rather size, shapes and spacings) can easily be demonstrated by considering the effect of different void geometry on F_1^{lc} (Fig.22) ($\equiv \sigma_1'^{c}$) on the position of the plane fo^{lc}. As the intervoid spacing reduces (increase in b/w) the value of F_1^{lc} ($\equiv \sigma_1'^{c}$) reduces (for a given value of a/b) and thus the plane fo^{lc} will withdraw along the axis σ_{11} of Fig.23 i.e. the state of stress to cause fracture will decrease in severity.

Very little practical information has been published about coalescence as, by its very nature of instability, it is difficult to observe the event.

Roberts, Lehtiness and Easterling (74) pulled pieces of polished steel strip to failure in the chamber of a stereoscan electron microscope and watched voids develop around surface inclusions and coalesce. The series of events they observed are shown in a generalised form in Fig.24 which shows a change over from smooth void growth to necking down of the remaining ligaments leading to void coalescence.

Although these observations are of voids on the surface they nevertheless give a qualitative view of the actual events of coalescence.

Naguno (75) drilled .30mm dia. holes into a strip tensile specimen and observed the fracture of the specimen across the section concluding that the holes grew until some time when they were joined by shearing across the ligament. Although Naguno considered this to be the act of void coalescence it is, in fact, the growth of macrovoids (in this case 300 μm dia.) followed by shear band localisation (16-19). The mechanisms operating within the shear bands being those involved with the unstable act of coalescence.

2.9 Mechanics of ductile fracture

Standard linear elastic fracture mechanics and general yield fracture mechanics parameters can of course be used to describe ductile fracture but conventional tests to give these parameters are rather bulky, i.e. a conventional compact tension test piece for some high toughness high ductility steels may weigh several tonnes, and thus be rather difficult and expensive to test.

Within the previously mentioned parameters of stress states, particle distributions and sizes several attempts have been made to describe suitable parameters which may be linked with the conventional toughness measurements (K_{1c}, C.O.D., J.).

Hancock, Mackenzie and co-workers (67,76,77,78) have considered the stress state dependence of a materials ductility and from this estimated conventional fracture mechanics parameters (δ_{IC} and K_{IC}).

These workers used round tensile test pieces with pre-machined circumferential notches cut in them, the notches having varying notch root radii (1.27mm to 3.8mm) thus varying the stress state of each specimen. These specimens

were pulled in tension to instability and the ductility measured as:-

$$\varepsilon_f = 2 \ln (R/R_o)$$

where R_o = radius of original ligament

R = final radius of ligament at instability/fracture

They found from metallography that the failure of these test pieces initiated in the centre of the specimen and thus selected the stress analysis of Bridgman (53) (cf) to estimate the effective stress state in the region of failure.

The stress state can be expressed as two parameters:-

$$\sigma_m = \frac{\Sigma \sigma_{kk}}{3}$$

$$\bar{\sigma} = \left[\tfrac{1}{2} \Sigma (\sigma_i - \sigma_j)^2 \right]^{\frac{1}{2}}$$

These two values can be combined into one single stress state parameter.

$$\frac{\sigma_m}{\bar{\sigma}}$$

Which is a measure of the stress states triaxiality (as $\sigma_m/\bar{\sigma}$ increases, the triaxiality of the system increases).

This parameter was then plotted against ε_p^f and gave the type of curve shown in Fig.25 where the ductility can be seen to reduce with increasing triaxiality ($\sigma_m/\bar{\sigma}$).

As the micro-mechanisms observed in this case do not operate at a point but over a finite volume of material the necessary values of $\sigma_m/\bar{\sigma}$ and ε_p^f must be met over that volume of material. Hancock et al. estimated this volume, or rather in two dimensions this length, to be 200 μm, as this was the length associated with most of the features of failure in their material.

Using the slip line field solution of Green (79) for a 3 point bend specimen with a key hole notch the values of $\sigma_m/\bar{\sigma}$ and ε_p, together with an estimate of δ (the crack opening displacement) for values of ε_p at the surface were calculated for the notch plane of such a specimen (Figs. 26,27,28).

Hancock et al. then used these in the following way:-

The initial radius of the key hole in 1400 μm (Ro). The 'characteristic material length' (from metallography) is 200 μm.

Thus:-

$$\frac{R}{R_o} = \frac{1400 + 200}{1400} = 1.14$$

$$\frac{\sigma_m}{\bar{\sigma}} \text{ at } \frac{R}{R_o} = 1.14 = 0.68$$

$$\text{and } \frac{\varepsilon_p}{\varepsilon_{surface}} = 0.76$$

Referring back to Fig.25

at $\sigma_m/\bar{\sigma}$ of 0.68 the value of ε_p to cause fracture (ε_p^f) is

= 0.18

thus ε surface $= \frac{0.18}{0.176} = 0.24$

From Fig.28 δ = 1.3mm ε_s = 0.24

As this value of δ does not include any elastic displacements 0.2mm should be added to it to account for this error.

Therefore δ lc = 1.5mm

An actual test was carried out using a three point bend key hole notched specimen of the above geometry from which the C.O.D. was found to be 1.7mm which is in good agreement with the theoretical prediction of 1.5mm.

Although this approach appears to yield good results it does have several weaknesses. The major one of which is the rather arbitary choice of the 'characteristic material length', they chose 200 μm because this is the

distance between inclusion colonies in the steel they used, and the critical event in the fracture appeared to be the linking up of these colonies. Thus the choice of 200 μm is more subjective than objective, and also leaves the question of what this distance would have been if the inclusions had been randomly distributed rather than being found in colonies.

Rice and Johnson (80) considered the interaction of a crack tip with the nearest voiding particle. Using a modified slip line field for a blunt crack tip (Fig.29), which unlike the standard Prandtl field for a slit crack, shows an area of intense strain concentration in front of the tip in area D (Fig. 29). If the crack tip blunts to a semi-circle of diameter δ_t , region D would have exponential spiral slip lines and extend a distance.

$$\left(e^{\pi/2} - 1\right) \delta_t/2 \quad = \quad 1.9\, \delta_t$$

ahead of the crack tip.

Thus a very simple version of the model put forward by Rice and Johnson is that the crack would open up until region D is over a voiding particle which then rapidly grows to coalesce with the crack tip. From this over simplification of Rice and Johnson's work we might assume that the C.O.D. (δ_t) would be of the order of the distance between voiding particles (Xo).

In fact the detailed analysis which they carried out gave results very near to this. Fig.30 shows these results in a normalised form and $\delta t/Xo$ does indeed vary from 1.0 at high volume fractions of particles to 2.0 at low volume fractions.

This model is valid for fracture from macro-inclusions where the large particles do in fact join up, as one might expect in dirty steels or weld-ments, and these results do indeed fit quite well with practice (81) for such materials. Unfortunately most materials fail by void sheet localisation at some point before coalescence and thus this model can only be an upper bound for δt.

2.10 Stresses under a notch tip

As indicated in sections 2.5, 2.7 and 2.8 the stresses and strains acting over an area of material are of great importance when considering either the likelyhood of ductile fracture occurring in that area or the stage that the damage leading to such a fracture may have reach.

High levels of both stress and strain concentrations are found in structures at points of sharp dimensional change, such as right angle joints, key ways or notches. Thus if one wishes to investigate ductile fracture an adequate analysis of the situation at one such discontinuity would be of great value. As a sharp notch is the easiest of these discontinuities to produce in a test piece a further discussion of the stresses and strains acting beneath it are appropriate.

The problem of the stresses acting under the tip of a notch have not yet been completely solved for the situation of general yield, but the solution under the elastic regime on one hand and the solution for the stress distribution under an unstable neck in a tensile bar have both been adequately solved.

a) Elastic stresses under a sharp notch

One of the accepted analysis of this situation is due to Neuber (82) whose treatment gives the distribution of the three principal stresses shown in Fig.31, the distribution shown here is for the specific case of the stresses acting on the notch plane in a circumferentially notched tensile specimen but an almost identical distribution can be obtained for all notches. The important feature of this analysis is that the radial stress rises rapidly under the notch to a maxima at some finite distance under the notch and then falls off with increasing distance from the notch tip.

Neuber (83) further suggests that the elastic solution can be extended into the plastic regime by the following relationship:-

$$\left(K_{\sigma_p} \cdot K_{\varepsilon_p}\right)^{1/2} = K_T$$

where K_τ = elastic stress concentration factor

$K_{\epsilon p}$ = plastic strain concentration factor

$K_{\sigma p}$ = plastic stress concentration factor

Thus providing that the strain concentration is known the elastic stress concentration can be converted to plastic stress concentrations.

This relationship has been shown to work well under several geometries by Gerewall and Weiss (84).

b) Plastic stresses under the neck of a tensile specimen

The analysis which is used in this situation can be attributed to Bridgman (53) whose work led him to the following relationships for radial (σ_r), hoop (σ_θ) and axial (σ_a) stresses as a function of position across the section.

$$\sigma_a = \bar{\sigma}\left[1 + \ln\left(\frac{d^2 + 2dR - r^2}{2dR}\right)\right]$$

$$\sigma_r = \sigma_\theta = \bar{\sigma}\ln\left(\frac{d^2 + 2dR - r^2}{2dR}\right)$$

where R = profile radius of the neck

d = radius of minimum cross section

r = position from the centre line

$\bar{\sigma}$ = effective stress = $\left[\frac{1}{2}\sum(\sigma_i - \sigma_j)^2\right]^{\frac{1}{2}}$

These relationships are plotted out in Fig.32 from which it can be seen that the stresses rise rapidly from the edge of the material to reach a maxima in the centre of the specimen.

Although this analysis was originally performed for a necked tensile specimen it can easily be applied to the case of a pre-notched specimen after fully plastic conditions have been reached. Earl and Brown (85) and Brown and McMeeking (86) have both shown that this analysis works well for the central region of such a specimen.

2.11 Strain concentrations (plastic) under a notch or crack

Weiss (87) following on from Neuber's work analysed the strain concentrations under a plastically deformed notch which he related to the elastic stress concentration factor (K_T) as follows:-

$$\varepsilon_y/\varepsilon_n = \left(K_T\sqrt{\rho/4}\right)^{2(n+1)^{-1}} \cdot x^{-(n+1)^{-1}}$$

where

ε_y = strain at point X under the notch

ρ = notch root radius

ε_n = remote strain

n = work hardening index

i.e.

$$\varepsilon_y = \varepsilon_n \left(K_t \sqrt{\rho/4} \right)^{2(n+1)^{-1}} \quad x^{-(n+1)^{-1}}$$

He found this relationship predicted the strain at notches in round bars to a good degree of accuracy.

Lie et al. (88) have also successfully used this relationship to predict strains in notched plates under tension. They also point out that this relationship is very similar to that indicated by Rice and Rosengreen (89) for the strain singularity ahead of an elastic/plastic crack:-

$$\varepsilon = F\,(r)^{-(n+1)^{-1}}$$

where F = Function of both applied stress and geometry

r = Distance from the crack tip

n = Strain hardening exponent

2.12 Summary of literature

In the next seven pages a brief summary of the more important points of the literature are given in tabular form. These tables are necessarily brief and only give the most general points of each entry.

Author	Type of Particle	Size Dependency of Nucleation	Type of Work	Other Comments	Relationship
Brindley and Lindley (33)	Long thin films of carbibe in steel	Small particles void first	Observation	Small ≡ Thin	$\varepsilon_f \propto f(r)$
Lindley, Oats and Richards (8) (47)	Long thin films of carbide in steel	Small particles void first & an increased chance if oriented in axis of tension	Observation & Theoretical model	Small ≡ Long & Thin	$\varepsilon_f \propto f(r)$
Smith & Barnby (36)	Long thin films of carbide in steel	Small particles void first	Observation and Theoretical model	Small ≡ Thin	$\widehat{\tau_c} = \left[\frac{d}{d+l}\right]^{1/2}\left[\frac{2\gamma\mu}{\pi(1-\nu)l}\right]^{1/2}$
Brown & Stobbs (41)	Spherical elastic second phase particle	Small particles void first, but only a weak dependency	Theoretical model	Disagree with their own obse-rvations	$\varepsilon_c = \frac{3\pi\gamma}{8\alpha^2\mu b}\left(\frac{\alpha^2\varepsilon_{pr}}{8\pi b}\right)^{1/4}$

Author	Type of Particle	Size Dependency of Nucleation	Type of Work	Other Comments	Relationship
Inoue & Kinoshita (25)	Spherical carbides in steel	Small closely spaced carbides void first	Observation & a qualitative model	Carried out at const. vol. fraction	$\varepsilon_f \propto$ Particle Spacing
Tanaka et al. (39)	Elastic spherical particle well bonded to the matrix	Large strains to void very small particles but larger particles independent of size	Theoretical model	Combined two criteria, both of which must be met	$\varepsilon_f \propto f(1/\sqrt{r})$ r is small $\varepsilon_f \neq f(r)$ r is large
Brown and Stobbs (41)	Spherical elastic second phase particle	Large particles void first	Observation	Disagree with their own theory	$\varepsilon_f \propto f(1/r)$
Easterling, Fishmeister and Navara (10)	Spherical carbides in steel	Small particles void first but only a weak relationship, & a large spread of	Observation		$\varepsilon_f \propto f(r)$

Author	Type of particle	Size dependency of nucleation	Type of Work	Other Comments	Relationship
		sizes regardless of strain			
Broek (34) (13)	Inclusions and second phase particles in Al alloys	Large particles void first then small particles void in sheets just before fracture	Observation	Macro voiding followed by void sheeting. An effect of cohesive bond strength rather than a size effect	
Gurland & Plateau (5)	Spherical elastic coherent particle	Large particles void first	Theoretical model		$\varepsilon_f \propto f(V_f)$ or $\sigma = \frac{1}{2}\left(\frac{E\gamma}{a}\right)^{1/2}$
Ashby (38)	Spherical elastic coherent particles	Large particles void first	Theoretical model	Based on back forces of secondary dislocation loops	$\varepsilon_f \propto f(V_f)$ or $\varepsilon_n = \frac{4k\gamma_o}{Gxb}$

Author	Type of Particle	Size Dependency of Nucleation	Type of Work	Other Comments	Relationship
Butcher (35)	CuO precipitates in Cu	Voids always associated with larger particles	Observation and theoretical model	Probably only applicable to large particles	$\varepsilon_f \propto f(1/r)$
Kleverbring and Mahrs (42)	Spherical elastic second phase particles	Large particles void first	Theoretical model	Similar analysis to Ashby's (38)	$\varepsilon_f \propto f(1/r)$ or $\varepsilon = \frac{\sigma_c b \Omega}{\kappa r}$
Toya (43)	Spherical particle	Large particles form voids first	Theoretical model	Considers a 'crack' at the interface rather than complete decohesion	$P_{cr} \propto f(1/\sqrt{r})$
Sundstorm (45)	Spherical particle	Large particles form voids first	Theoretical model	Again considers crack formation at the interface rather than complete decohesion	$\varepsilon_{cr} \propto f(1/\sqrt{r})$

Author	Type of Void	Shape Change	Effect of Stress State on Growth	Relationship
M^{c}Clintock (63) (64)	Cylindrical hole with an elliptical cross section	Small enough to be ignored	Growth rate is proportional to the sinh of the hydrostatic stress	$d\eta \cdot \frac{\sinh\left[(1-n)(\sigma_a+\sigma_b)/2\bar{\sigma}\sqrt{3}\right]d\varepsilon}{(1-n)\ln F^3}$
Rice and Tracy (65)	Initially spherical	Small enough to be ignored	Growth rate is proportional to the sinh of the hydrostatic stress	$D=\frac{\dot{R}_o}{\dot{\varepsilon}R_o} = 0.56\,\sinh\left(3\sigma^{m}/2\sigma_y\right)$
Tracy (66)	Initially spherical and considering interaction with other voids	Can, again, be ignored	Growth rate is proportional to the cosh of the hydrostatic stress	$\frac{\sigma_r}{\bar{\tau}} = \coth^{-1}\sqrt{\frac{1+3\dot{\varepsilon}^2}{1+(\dot{\varepsilon})^2}} - \coth^{-1}\sqrt{\frac{1+3\dot{\varepsilon}}{1+(\dot{\varepsilon})^2}\left(\frac{b}{r_o}\right)^4}$

Author	Basis	Conclusion
Berg (20)	Dilational plasticity and strain softening	The classical yield cylinder is capped. The position of this cap is controlled by the void volume fraction. An increase in the triaxiallity of the stresses will increase the ease of dilational banding, i.e. causing failure at a lower strain.
Thomason (69)	Load instability	An increase in the hydrostatic tension leads to a marked drop in ductility.
Hancock (70)	Strain to cause a radial load maxima.	Increase in void volume fraction exponentially decreases the ductility.
Thomason (71)	Investigates the limit of stability using Hills (72) theories.	The classical yield cylinder is cut by failure planes. The position of these planes is controlled by the size and spacing of the voids. An increase in the hydrostatic stress brings the material nearer to the failure planes, thus decreasing the materials ductility.

Author	Method Used	Accuracy of Result
Hancock et al. (67) (76) (77) (78)	Empirical relationship between σ_m/σ and ε_f is used via a 'characteristic material length' to give a value of C.O.D.	Predicts the actual C.O.D. to within 15% but relies heavily upon the rather vague value of 'characteristic material length'
Rice and Johnson (80)	Slip line field solution for a blunt crack is used to predict C.O.D. as a function of particle spacing	Predictions fit well for dirty steels but not when the mechanisms of fracture are other than by macrovoid coalescence with the crack tip

3. MATERIAL

The material used in this work falls into the following categories.

3.1 Mild steel bar stock

Mild steel bar stock corresponding to BS 970 - 22M07 was used for preliminary investigations, this steel having first been given a spheroidising treatment of two hours at 650°C.

The specification of this material is:-

C	Mn	S
0.1%	1.0%	0.25% max

3.2 1.25% Mn steels

A series of 1.25% Mn steels with carbon contents ranging from 0.10 to 0.30% C were produced from electrolytic iron melted in 5Kg batches (with the appropriate Mn and C additions). These steels were cast into blocks 25mm square and 200mm long,

which after reheating to 900°C were hot rolled to give a 50% reduction in thickness, (to dispose of the cast structure) before being heat treated.

The three main steel produced in this way had the following compositions:-

Steel	Mn%	C%
H1	1.32	0.15
H2	1.26	0.23
H3	1.12	0.10

A similar steel to the above was produced which had a high sulphur content (0.75%), this steel was designated HSO.

These steels were given the following heat treatment:-

Austenitised at 900°C for two hours and then water quenched to give a martensitic structure. This was followed by tempering at 625°C for eight hours to give a final structure of randomly distributed spheroidised carbides.

3.3 Commercial steel

These above mentioned laboratory produced steels fall very close to one commercial steel BS 4360 grade 50D (0.15 to 0.25% C, 0.1 to 0.5% Si. 1.5%Mn) which will probably be one of the main structural steels to be used in the construction of off-shore structures. A 25mm thick plate of which, in the as rolled condition, was acquired from the British Steel Corporation Laboratories in Middlesborough.

3.4 Sheet aluminium

Commercial purity aluminium sheet specimens were also produced from 1mm thick annealed sheet.

4. SPECIMENS

4.1 Parallel tensile specimens

Six parallel sided, 12.5mm dia. tensile bars were produced from the low carbon steel bar stock (BS 970 - 22M07), which were fully annealed before testing.

4.2 Single circumferentially notched specimens

A series of tensile specimens with a single circumferential notch were produced from the high sulphur steel (HSO) the dimensions of which were:-

Dia	12.5mm
Notch Depth	2.5mm
Flank Angle	60°
Notch Root Radii	0.125mm

4.3 Multi notched tensile specimens

Tensile test pieces, each with six circumferential notches, were produced from the mild steel bar stock and from the 'H' series steels. The test piece dimensions are shown in

Fig.33, and a photograph of one such specimen shown in Plate 1. The multi notched specimens with the suffix '30' have notch root radii of 0.75mm as opposed to the standard radius of 0.125mm.

The basic concept of these test pieces is that each notch is cut slightly deeper that the preceding one, so that when these specimens are subjected to tensile stresses above the yield point each notch causes different plastic strain concentrations along the plane of that notch.

All of these multi notch specimens were cut from the longitudinal direction (i.e. the rolling direction) of the material under study.

The main reason for choosing a specimen of this design is to minimise any variations which naturally exist in any material. In this case the two most important ones being the possible compositional and heat treatment variations which could occur across a comparatively large amount of material.

4.4 No.14 Hounsfield specimens

Several modified Hounsfield tensile test pieces were produced from each steel so that uniaxial stress-strain data for the materials under study could be obtained. Again they were cut from the longitudinal direction of the material. The modification of test pieces was simply an increase in gauge length from 23mm to 50mm so that a displacement measuring transducer could be attached along the gauge length.

4.5 Charpy test pieces

Several standard CharpyV notch specimens were also produced from each steel.

4.6 Single circumferential notched tensile bars with varying notch profiles

A series of such specimens were produced from the BS 4360 50D plate. The dimensions were as follows:-

Bar dia. 12.5mm

Notch Depth 2.5mm

Notch Root Radii 0.15mm

0.20mm

0.25mm

0.40mm

0.55mm

1.00mm

1.10mm

2.50mm

3.25mm

5.70mm

Again all of these specimens were cut from the longitudinal (rolling) direction of the plate.

4.7 Three point bend specimens

Several three point bend specimens were crudely prepared by sawing a notch into a 160mm length of 20mm dia. mild steel bar stock (BS 970 - 22M07). This material was in the normalised condition.

The notch dimensions were as follows:-

Depth 12mm

Root Radii 0.50mm

4.8 Sheet aluminium specimens

These specimens were prepared from 1mm thick sheets of commercially pure aluminium. The specimens were 25mm wide and 75mm long. An array of artificial voids were produced in the central region of the specimen using a small punch with a tip diameter of 0.5mm. These artificial voids were placed at random in an attempt to simulate real voids in a material.

5. MEASUREMENT OF STRESS AND STRAIN

In all the above cases the gross stress and strain acting on the test piece is of little specific interest as the mechanisms under study occur only over a small region of the test material, thus the true stresses and true strains over that small area are the only ones of any real interest.

5.1 Strain

The strains in the notched bars were measured as the change in diameter across the notch root:-

$$\varepsilon_p = 2 \ln(d_o/d)$$

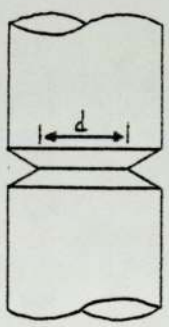

where d_o = original diameter

d = diameter after straining

In cases of strain gradients over a small region of material the strain was taken as being the gradient of displacement:-

$$e = \frac{d\delta}{dx} \qquad \delta = \text{displacement}$$

$$x = \text{positioning}$$

$$\therefore \quad \varepsilon_p = \ln\left(\frac{d\delta}{dx} + 1\right)$$

or if the measurements are radial

$$\varepsilon_p = 2\ln\left(\frac{d\delta}{dx} + 1\right)$$

5.2 Stresses

The true stresses in the above bars were, wherever possible, measured as the instantaneous load divided by the area under the notch.

6. VOLUME FRACTION MEASUREMENTS

Volume fraction measurements were carried out in the following ways:-

a) By the use of an Image Analysing Computer at magnifications of X1285 and X2570. This Image Analysing Computer was calibrated using on screen measurements to an estimated accuracy of $\pm$ 1%.

b) Extraction replicas taken from polished and etched sections. The replicas being removed from the sections by standard electrolytic etching techniques (electrolytically etched at 4.5 volts in a solution of 10% HCl in alcohol). This technique may be considered to lift 95 to 100% of all particles from steels. These replicas were then examined under a Transmission Electron Microscope (Joel JEM 100B) and these images then used to give the required parameters.

7. RESULTS

7.1 Parallel tensile specimens

The silhouettes of the 'necks' of these test pieces are shown in Fig.34 from which it can be seen that a considerable amount of localised deformation took place before final fracture.

A metallographic examination of a section of the final fracture was carried out and a typical area shown in plate 2, where it can be seen that the fracture is one of void coalescence with a final void size range of 4 to 20 μm, the voids that exist slightly away from the fracture surface have a size range of 1 to 3 μm, but a similar spacing (and therefore concentration).

The mean void centre spacing is:-

Fracture surface 14 μm

Surrounding area 12.5 μm

Plate 3 shows the equivalent necked section of a specimen just prior to fracture, when the void spacing is:-

Mean void centre spacing 25 μm

7.2 Single circumferentially notched tensile specimens

The stress extension and potential drop curve is shown in Fig.35 from which it can be seen that the extension to failure is 1.5mm with a true stress of 520N/mm^2 and the potential drop only showing a significant rise after instability was reached. General views of the fracture surface, using an S.E.M. and taken from the centre of the bar, are shown in plate 4. This shows failure by void coalescence at a final void size of 16 to 80 μm (Mean size = 30 μm). The particles around which these large voids formed are clearly visible in the centres of most of the voids and have themselves a size range of 10 to 50 μm. Also on this fracture surface smaller colonies of voids can be seen whose coalescence diameter is less than 5 μm (plate 4, area A) and whose nucleating particles are difficult, if not impossible, to see.

7.3 Multi notch tensile specimens

The stress and strain data obtained from the shadow-graphs of the specimens, taken both before and after stressing, is laid out in Tables 1a to 1g. This data is also represented graphically in Figs.36a, b, c, d, e, f and g. The line representing the stress-strain history of the deepest notch was calculated from the output from the clip gauge which was attached across that notch during testing. From Fig.36 it can be seen that the various notches cover most of the curves, except possibly for a gap just before final fracture. Changes in notch root radius are also laid out in this table, these having been measured by overlaying replicas onto the shadow-graphs of the specimens.

After straining the notches were broken open at -196°C. These fracture surfaces were then examined under an S.E.M. and found to have a topography of mainly cleavage with a few voids visible on the cleavage facets. An example of which is shown in plate 5 where many voids can be seen on the fracture surface.

A series of random photographs were then taken of the central* area of each fracture at known magnifications and known beam angles, so that accurate quantitative measurements could later be made. (The magnifications were generally between X1000 and X2000, with beam angles between 30° and 50°). A series of consecutive photographs were also taken of the areas immediately under the notches, again at known magnifications and beam angles. The S.E.M. magnifications were calibrated using a diffraction grating of known line spacings.

Of the specimens which fractured during testing all had a final fracture surface consisting of an outer ring of ductile fracture (i.e. void coalescence) with an inner core of cleavage.

As the S.E.M's. electron beam is not at right angles to the specimen surface the image has different magnifications

---

* 'The central area' in this case means within the area a quarter of the distance between the centre and the edge of the fracture surface.

along each axis. Thus to measure the true area over which the above photographs were taken a correction factor is necessary:-

If the beam angle is θ (Fig.37) and the image is Xmm wide by Ymm high then the actual area under examination is:-

$$\text{Actual area} = \frac{1000X}{M} * \frac{1000Y}{M \cos \theta} \ (\mu m)^2$$

where M = Magnification

or if $\theta = 45^{\circ}$

$$\text{Actual area} = \frac{1000X}{M} * \frac{2(1000Y)^2}{M} \ (\mu m)$$

Two sets of measurements were taken from these sets of photographs of the central area:-

a) The voids which can be seen on the fracture surfaces (plate 5) can quite simply be counted on each photograph, and as the true area of each photograph is known an estimate of the number of voids per unit area can be made for each

area of each fracture surface examined. This measure can be expressed in many ways but possibly the easiest is the average nearest neighbour distance which is:-

$$\text{Average Nearest Neighbour Distance} = \frac{\sqrt{\text{Area}}}{\sqrt{\text{No of Events}}} \quad \mu m$$

These results are listed in Table 2a to 2g and shown graphically as a function of applied plastic strain in Figs.38a, b, c, d, e, f and g which show good straight line relationships with correlation coefficients of .97 to .99. Each point on these graphs represents the average of 6 to 10 separate observations.

b) The size of the above mentioned voids can also be measured from these central area photographs. The size ranges found on each surface are given in Tables 3a to 3f, and plotted in Figs. 39a, b, c, d, e and f, from which it can be seen that the minimum observed void sizes remain constant whilst the maximum size increases with strain.

An analysis of the void concentrations of the area just beneath the notches was made using 10μm strips running parallel to the notch root (see plate 6). Examples of such an analysis are shown in Fig.40a, b, c, d, e and f where the Average Nearest Neighbour Distance (ANND) appears to run at a minimum for some distance under the notch tip before rapidly increasing at some distance from the tip.

The polished sections were examined both optically and under an S.E.M. with particular attention being paid to the near notch area of the section. Examples of these areas are shown in plate 7 where damage can be seen around the notch tip area, the central region of these specimens was also examined but no comparable damage could be found.

7.4 No.14 Hounsfield tensile tests

The uniaxial stress strain curves obtained from these tensile specimens are shown, for steels H1, H2, H3 and BS 4360 50D, in Figs.41a, b, c and d. The relevant points of which are laid out in Table 4.

7.5 Charpy V notch specimens

Standard Charpy impact tests, carried out at 20°C, yielded the results laid out in Table 5 for steels H1, H2, H3 and BS 4360 and 50D. It is noticeable that 50D shows a dramatic change in impact resistance depending upon the orientation of testing, and in fact the fracture surfaces of the samples also show considerable differences (see plate 8) depending upon this orientation.

7.6 Single circumferential notched tensile bars with varying notch profiles

The stress/strain measurements taken during the testing of these specimens are shown in Table 6 together with the stress complexity factor ($\sigma_m/\bar{\sigma}$) associated with each of these notches.

$\sigma_m/\bar{\sigma}$ is taken as being the stress complexity in the central region of the bar i.e. from Bridgman's (53) stress analysis:-

$$\sigma_r = \sigma_\theta = \bar{\sigma} \ln\left(\frac{d^2 + 2dR - r^2}{2dR}\right)$$

$$\sigma_z = \sigma_r + \bar{\sigma}$$

In the centre of the bar ($r = 0$)

$$\sigma_\theta = \sigma_r = \bar{\sigma} \ln\left(\frac{d^2 + 2dR}{2dR}\right) = \sigma_z - \bar{\sigma}$$

Thus:-

$$\frac{\sigma_m}{\bar{\sigma}} \text{ max} = \frac{1}{3} + \ln\left(\frac{d}{2R} + 1\right)$$

All of these specimens which were tested to fracture failed by fully fibrous (i.e. ductile) fracture. It was also noticed that these fracture faces also showed a high degree of orientation (plate 9 for a typical fracture).

Fig.45 shows the failure strain of each of the specimens plotted against the appropriate value of σ_m/ε, calculated as shown above.

Some of these test pieces were not tested to fracture but stopped at instability, these specimens were then sectioned along their centre lines and carefully polished and etched. The near notch regions were then examined for strain concentrations.

Plate 10 shows one such region where it can be seen that the steel has a structure of highly banded pearlite. These bands, in the near notch region, are no longer straight, as they are in the matrix, but are curved thus demonstrating the strain concentrations under these notches.

If the displacement of each one of these bands is measured with respect to its position beneath the notch a graph of displacement against position can be constructed from this, and as strain is the gradient of displacement (see section 5.1), a graph of strain against position can be made (Fig.42).

The predicted strain concentrations, calculated from Weisses (87) formula are also plotted on these graphs.

7.7 3 point bend specimens

Plate 11 shows the surface of the fracture after it has been broken open under liquid nitrogen (Fig.43 is a diagramatic representation of this fracture surface). This shows an area of voiding at a distance under the notch of about 1mm, with no detectable signs of equivalent voiding in the area leading up to it.

Although the deformation of this sample was not recorded the area under the notch to the opposite surface had undergone considerable plastic straining (i.e. the bar was left permanently deformed, with a bend of about 30°).

7.8 Sheet aluminium specimens

These specimens were strained until they reached instability and the resulting deformation is represented in Fig.44 where the imminent fracture can be seen running through some of the artificial voids. The angles of these shears are shown in Fig. 44 and have a spread from 32° to 72° from the normal to the direction of loading.

7.9 Particle analysis

a) Inclusions

All of the H series steels were found to contain a few inclusions but in all three (H1, H2 and H3) the average size was found to be just over 1 μm. The average inclusion sizes and their spacings, for all three steels, are as follows:-

Steel	Size (μm)	A.N.N.D. (μm)
H1	1.37	26
H2	1.13	22
H3	1.43	23

The above analysis was carried out using an image analysing computer.

These inclusion concentrations represent a volume fraction of approximately 0.0015.

b) Carbides

Using transmission electron metallography on extraction replicas from the H series steels the sizes and distributions of the spheroidised carbides were measured.

These measurements are laid out in Table 7.

Examples of the electron micrographs are shown in plate 12.

8. DISCUSSION

8.1 Parallel tensile specimens

8.1.1 The stresses acting in the 'neck'

The stress system operating under the neck of such specimens as these is, as already mentioned, best described by the Bridgman analysis (53):-

$$\sigma_r = \sigma_\theta = \bar{\sigma} \ln\left(\frac{a^2 + 2aR - r^2}{2aR}\right)$$

where

σ_r = radial stress

σ_θ = hoop stress

$\bar{\sigma}$ = flow stress

R = neck profile radius

a = radius of minimum cross section

r = position from centre line

Considering the centre of the section (r = 0), where the radial and hoop stresses are a maxima (see Fig.32). As the neck forms:-

R will decrease rapidly (from infinity)

a will decrease comparatively slowly

Therefore as the neck forms there is an increase in the radial and hoop stresses under the neck, i.e. the hydrostatic tension will increase and continue to be a maximum in the centre.

8.1.2 Effect of the stresses acting in the 'neck'

Assuming that voids have already been nucleated during the stable plastic deformation they will start to grow rapidly under the hydrostatic tension (63,64,65,66) and thus should grow faster in the centre of this necked region until such time as they coalesce to form the final fracture. As already stated (section 2.7) the existing growth theories fall short sometime just before coalescence and thus the voids 'growing' to coalescence overestimate the strain to fracture considerably, as shown in Fig. 11 where these theories are compared to the results of Edelson and Baldwin (14).

Considering the above, the expected fracture would be one of initiation and growth from the centre of the bar, which compares well with the final fracture shown in Fig.34 which shows a central region of fracture by void coalescence with shear lips at the edge, i.e. the fracture started in the centre and grew outwards.

8.1.3 Geometric considerations

It is interesting to note that in a cup and cone fracture, such as this, it is kinematically necessary that an area of pure dilation should occur in the centre of the bar (the flat plateau in the centre of the final fracture) before the shearing off of the edge occurs. This is required because it is geometrically impossible for sliding to occur over closed conic surfaces of zero extension whilst sliding over open conic surfaces is indeed possible. It is therefore required that for flow localisation to occur along these surfaces of zero extension an open region must develop at the axis of the bar. Since no sliding is allowed prior to the development of this region, it must develop purely by dilational flow localisation. This can occur only on a plane perpendicular to the axis which by symmetry does not require any sliding. An open surface, as such, may not be necessary as the amount of porosity at the neck may itself be large enough to allow sliding along the closed conic surfaces. Whichever of these two is necessary it is obvious that there must be a considerable amount of void nucleation, growth and possible coalescence in the central region of the bar before the final cup and cone fracture can develop.

8.1.4 Comparison with metallography

From the photomicrographs of this specimen shown in plate 2 and the data given in section 7.1 where the fracture surface is compared to a section just before fracture it can be seen that the formation and growth of voids appears to be a continuous process up to a certain point when some of the voids suddenly grow to coalescence and form the fracture surface. These voids did not grow at random but in a plane normal to the applied stress.

The reason for this sudden acceleration in growth rate cannot be explained by the effect of the macrotriaxial stresses on the growth rates because these stresses are still increasing at the same smooth rate (with the change in neck dimensions) so other mechanisms must be considered.

8.1.5 Possible mechanisms of the final fracture

One possibility is an increase in the local stress concentration due to the presence of the voids i.e. the $K\sigma_p$ value associated with the small voids may cause a stress interaction between them, which would accelerate the growth in the radial direction to cause a coalescence. This concept has been investigated by other

workers (67,68) who calculated the likely growth acceleration caused by this type of interaction (see Fig.12), which could be as high as times two, but only when the voids have grown very close together (in our case < 5μm apart). This is much closer than they are just before fracture (plate 2), when their spacing was measured as 14μm. As this idea would rely on both the size and spacing of individual voids other sites of void coalescence might be expected besides that of the final fracture.

Another possibility is one of conventional plastic instability in the ligaments between the voids, as proposed by Berg (20) and Thomason (71), where the load bearing capacity of the ligaments has decreased to such an extent by void growth that there is necking between the voids and thus simple necking to failure. The material is, after all, undergoing exactly this in forming the unstable neck.

Let us consider the known series of events leading up to the fracture in the context of Thomason's three dimensional principal stress construction (Fig.23). The neck formation increases the ddegree of stress complexity acting under it, thus causing the locus in Fig.23 to move out along the surface of the yield cylinder, in the

direction of positive triaxial stress. As the same time, because of this increased triaxial stress, the voids themselves are growing (63,64,65,66), thus reducing the surface tractions necessary to cause instability in the remaining ligaments, i.e. the dilational yield surface ($fo^{lc} = 0$ in Fig.23) is being moved back down the principal stress axis (σ_{II} in Fig.23). Thus we have a dynamic situation where the active stress-state and the necessary stress state to cause instability (or dilational yielding) are both moving towards each other and at some point they will obviously meet and failure will occur by the formation of a dilational band, within which there is material instability and the voids will coalesce. As soon as the dilational band begins to form the geometrical considerations preventing the cone part of the fracture taking place are removed and the shear lips associated with this type of fracture may form.

This latter approach seems the more likely as it goes quite some way to explain the sudden change from stable void growth to coalescence as has been observed.

8.1.6 Summary of the events leading to fracture

The process appears to have been one of void nucleation (possibly continuous, as there is an increase in concentrations with strain, i.e. a spacing of 25μm in the unfractured neck at a strain of 0.65 dropping to 14μm near the fracture surface at a strain of 0.70), followed by void growth as the neck forms. This neck increases the triaxial stresses in the centre of the bar (thus the void growth rate becomes more rapid in the centre of the bar). As the voids grow and the triaxial stresses increase the dilational yield surface and the active stress system move towards each other (in 3D stress space) until they meet and the intervoid ligaments become unstable forming a dilational band. All the deformation is concentrated into this dilational band in which the voids coalesce to cause failure. As there is a difference in the rate at which these events occur, depending upon the position across the section (the centre will proceed at a much higher rate for the reasons state above) a difference in fracture across the section may be expected. At the start of the final fracture the necessary conditions for failure will only be met in the centre of the bar, as this material fails the stresses acting on the outer ring of material will be reduced

in complexity moving this material further away from the state of dilational banding. As the same time the geometrical constraints preventing conical sliding from taking place are removed making the formation of the shear lips possible. Thus it is not surprising that classical cup and cone fractures occur (see Fig.32).

8.2 Single notch tensile specimen

8.2.1 The fracture surface

From the fracture surface of this specimen (plate 4) it is obvious that the final fracture was by void coalescence. The voids having been formed on the large inclusions which can be seen in the centre of some of these voids, these voids having then grown and coalesced. In this case the fracture did not initiate in the centre of the bar, but at the notch root, as observed during the test.

8.2.2 Probable stress distribution

This situation does not coincide with the analysis of stress used in the previous case, assuming that the final fracture is initiated in the region of highest hydrostatic tension, i.e. in this case the region with the highest hydrostatic tension must be

near the notch root and thus the above mentioned stress analysis of Bridgmans cannot be used. The elastic stress distribution due to Neuber (82,83) is probably nearest to this situation (this type of stress distribution is shown in Fig.31).

8.2.3 Detection of the onset of coalescence

In Fig.35 the potential drop curve is shown together with the stress-extension curve and only shows a significant rise at instability (in this case the onset of final fracture when the crack tip was seen to start from the notch root). As this type of equipment can detect a 0.5% change in the length of a crack (93) this can be considered to signify that no appreciable void coalescence had taken place until this point (assuming that internal cracking would show the same effect as an external crack, which would be expected with this type of D.C. potential drop equipment).

8.2.4 Formation of small voids and void sheets

In the fractograph of this specimen (plate 4) colonies of small voids ($< 5\mu m$ dia.) were found (area A). The presence of these smaller voids is difficult to explain with respect to the rest of the fracture except that they lie in

relatively inclusion free areas. As the growth of the larger voids can be explained in terms of their stress strain histories an examination of the possible stress strain histories of these smaller voids may be helpful. If it is assumed that both their size and concentration indicate that they were formed fairly late in the process, when the growth of the larger voids was in a fairly advanced stage then the interacting stress concentrations of these larger voids may have reached such a level as to cause small pre-existing voids to grow rapidly, until they become a significant factor in the imminent fracture, i.e. this is a case when the stress concentrating effect of two neighbouring voids is of significant effect.

8.2.5 Advance of the final fracture

As no detectable void, or crack, growth was recorded on the potential drop equipment until a crack was seen to form at the notch root, the final fracture cannot be considered to be void coalescence by simple growth but by the advance of a crack from the root of the notch and thus fracture from the outside rather than from the centre. The advance of such a crack being controlled by the stresses and strains in front of the crack i.e. as the already growing voids come under the

influence of the comparatively high triaxial stresses generated by the growing crack their growth will be accelerated until they coalesce with the tip of the crack.

Thus the model we have for this fracture is one of voids initially growing from the large inclusions until such a time as the notch tip starts to propagate a crack which greatly increases the triaxiality of stresses, thus exponentially increasing the growth rates of the voids (63,64,65,66) which themselves will interact to cause smaller voids to grow in between them.

8.2.6 The micromechanisms operating

Let us return to Thomason's (71) 3D stress-space construction (Fig.23) and consider these last events again. At some point just before the formation of these smaller voids the materials active stress will plot at some point on the yield cylinder below the dilational surface, the position of which is governed by the void population, when these small voids are formed in between the larger ones the position of the dilational surface will be radically altered and jump some considerable distance down the axis of maximum principal stress. Possibly to some point

below the point of active stress such that the system will become unstable and fail by a dilational band, thus propagating the crack into the next region of material to repeat this action and continue to propagate the crack.

8.2.7 Effect of these mechanisms on the mechanics of failure

Here we have a possible explanation for the void sheets which are frequently found on fracture surfaces (16,17,18,19) linking up larger macro-inclusions. The above observations are also of great interest when considering the mechanics of failure, especially from the point of view of the Rice and Johnson model (80) where they proposed that:-

$$\delta = AXo$$

where δ = C.O.D.

A = constant depending upon the spacing of voiding particles (A varies from 1 to 2)

Xo = spacing of particles

But, as we discussed in section 2.9, this model is only appropriate for a system where the failure is by macro-void coalescence. If the above mechanism of void sheeting is considered then this model of Rice and Johnson's should be modified to:-

$$\delta = A(Xo - Xs)$$

where Xs = ligament diameter at which void sheeting takes place.

This assumes that the void sheeting itself adds nothing to the value of δ, but if it were to, then:-

$$\delta = A(Xo - Xs) + A'X'o$$

where $X'o$ = the spacing associated with the void sheet nucleants

The problem would, of course, be to formulate an appropriate value of Xs, but if the strain to form the voids from the void sheet nucleants was known then a value of Xs could possibly be estimated.

8.3 Single circumferential notched tensile bars with varying notch profiles

8.3.1 Polished sections and strain concentrations

Fig.42 shows the strain concentrations calculated from these sections along with the the theoretical curves obtained from Weiss's relationship (87) (see section 2.11). It can be seen from these plots that there is an exceptionally good agreement between the predictions and the observations. Thus for any future estimation of strain concentration beneath a notch of this type Weiss's analysis may be relied upon as being reasonably accurate.

The other point of importance here is that the total extra displacement caused by this strain concentration is so small that in measurements of total ligament strain no correction for this extra displacement is necessary.

8.3.2 Strains to failure

Fig.45 shows the stress complexity factor for each notch ($\sigma_m/\bar{\sigma}$) plotted against that notches strain to failure.

From this plot it can be seen that the failure strain decreases with an increase in the stress complexity factor, in a similar way to that found by Mackenzie et al. (76) (see Fig.25).

8.3.2.1 Selection of a characteristic material length

If an attempt is made to analyse this data in the same way as that employed by Mackenzie et al. (see secion 2.9) the first problem to be overcome is the choice of a characteristic material length. Referring to plate 9 where a typical fracture surface of this material is shown, a highly orientated structure can be seen with many large elongated voids. The semi major axis of these elongated voids are aligned in the materials long transverse direction. If it is assumed that these large voids play an important part in the fracture, and the material between them is the region over which the final fracture occurs, then perhaps their spacing can be taken as being the 'characteristic material length'. A rough average of these voids spacings, measured in the short transverse direction (horizontally on plate 9) is about 600μm.

8.3.2.2 Using the characteristic material length to give conventional parameters

Thus with a characteristic material length of 600μm an attempt can be made to follow the procedure described in section 2.9:-

Again using the key hole notch with an initial radius of 1400μm

$$R/Ro = \frac{1400 + 600}{1400} = 1.42$$

From Fig.26

$$\sigma_m/\bar{\sigma} \text{ at } R/Ro \text{ of } 1.42 = 1.1$$

From Fig.27

$$\text{and } \frac{\varepsilon_p}{\varepsilon_p} \text{ surface} = 0.58$$

From the data in Fig.45, when $\sigma_m/\bar{\sigma}$ has a value of 1.1 the necessary value of ε_p to cause fracture (ε_p^f) is:-

$$\varepsilon_p^f = 0.21$$

Thus ε surface = $\frac{0.21}{0.58}$ = 0.36

From Fig.28

δ = 2.40mm when ε_s = 0.36

If the appropriate elastic displacement of 0.2mm is added this value of C.O.D. becomes 2.60mm.

It is interesting to note that if this procedure is followed through using both 400μm and 800μm as the 'characteristic material length' the result is almost identical to the above (2.40 + 0.2mm elastic and 2.3 + 0.2mm elastic respectively). Also doubling Mackenzie's (76) value of 'critical material length' from 200μm to 400μm for his material only causes a change of 13% in his value of C.O.D.

Thus the value of the 'characteristic material length' does not appear to be as sensitive as was first assumed and can, in fact, be varied quite considerably without introducing anything other than quite small errors into the calculated value of C.O.D. Thus, if over quite a large range of values of 'characteristic material length' the resulting C.O.D. is roughly constant then the stress state to failure plots may be considered to describe a materials toughness in the same unique way as a C.O.D. value.

8.3.2.3 The strain to failure plot as a design curve

In many ways this type of curve may be of more use than a conventional fracture toughness value for this type of ductile fracture. The main use made of a fracture toughness parameter is to construct a design curve for safe/non-safe working conditions, but this type of stress state to failure plot is in itself a safe/non-safe design curve which may be used directly on any structure - providing that a reliable stress-strain analysis is available for the particular structure or component. This does not give this method a particular disadvantage over conventional parameters as they too require good stress strain analysis of components before they can be considered useful. The problem of a characteristic material length again appears when considering these curves in this way. In the C.O.D. analysis a wide range of values resulted in the same C.O.D. value, although the 'characteristic material length' can perhaps be given a lower bound i.e. the lowest value which does not introduce a large variation from the 'plateau' value. In the case of the C.O.D. analysis above, if the characteristic material length is reduced below 400μm there is a considerable change in prediction from the plateau of 2.4 + 0.2mm elastic. Thus if the lower bound of this plateau is used then we may have a 'critical' characteristic material length. By choosing a critical length in this way the problem of having to make a rather vague choice of some likely physical length which the material may demonstrate in some other way is avoided.

8.3.2.4 Comparison of this failure curve to the micro-mechanisms causing the fracture

It may be useful to consider these stress state to failure plots with respect to the mechanisms of ductile failure, i.e. the nucleation, growth and coalescence of voids. Very simply, an increase in strain will lead to an increased void population whilst an increase in the stress state complexity ($\sigma_m/\bar{\sigma}$), which in effect can be considered to be an increase in the positive hydrostatic stress, will lead to a greater void growth rate (see sections 2.7 or 2.12). It will also lead to an 'earlier' coalescence of these voids (see section 2.8 or 2.12). Since these stress state to failure plots are, in the limit, concerned with the final fracture, i.e. the coalescence of voids, let us look at the situation from Thomason's (71) model of void coalescence. The 3D stress space construction (Fig.23) requires the materials acting stresses to plot at some point on the surface of the yield locus, the higher value of $\sigma_m/\bar{\sigma}$ the further out along this locus in the direction of positive triaxial stress will the acting stresses plot. The position of the failure plane (fo^{1c}) - the dilational yield surface - is governed by the void populations size and spacing, the size of the voids being dominated by the triaxiality of the stresses acting upon them (see section 2.12) whilst their number (or spacing) is mainly controlled by the

strain the material has undergone. Thus for a material being strained at a low value of $\sigma_m/\bar{\sigma}$ the acting stress point will plot at a fairly low point on the yield locus and the failure plane, which initially would be at some distance away along the appropriate stress axis, will start to move towards it as there is an accumulation of damage (void nucleation and growth), this damage being controlled by both the stress state and the strain. This plane will continue to move towards the acting stress states position until it reaches it and failure by dilation occurs. If the material is strained at a higher value of $\sigma_m/\bar{\sigma}$ the acting stress will plot at a position some distance along the yield locus from the position in the previous case. The failure plane will start moving from the same initial position as above but because of the increased rate of damage accumulation caused by the higher value of $\sigma_m/\bar{\sigma}$ this failure plane will move towards the acting stress point at a comparatively high rate. Thus in this second case the material will fail at a much lower strain because a) the distance the failure plane is required to move to cause failure is less and b) because the rate at which it moves along this distance is greater. Thus the effect of changing the value of $\sigma_m/\bar{\sigma}$ can be demonstrated. The above arguments indicate that the effect of changing $\sigma_m/\bar{\sigma}$ will not be linear against strain to failure but will show an

exponential decay type curve, as $\sigma_m/\bar{\sigma}$ has two separate effects upon failure and also because the damage caused by void growth will be exponentially dependent upon $\sigma_m/\bar{\sigma}$ (see section 2.12). From this, curves similar to those found in practice would be expected (Figs. 25 and 45).

8.4 Multi notch tensile specimens

As can be seen from the stress strain graphs of these specimens (Fig.36a, b, c, d, e, f and g) the various notches cover virtually the whole of the stress-strain history of each of the final fractures, and also each of the points falls very close to the curve i.e. a high degree of confidence can be placed upon the measurements as they agree with the history of the notch measured during testing. Thus each of the notches from a material can be considered to represent various points in the life of the final fracture of that material.

8.4.1 Effect of strain on the average void spacing

Referring to Figs.38a, b, c, d, e, f and g it can be seen that the Average Nearest Neighbour Distance (A.N.N.D.) between voids decreases continuously with strain, but at a

different rate depending upon the material. The linear relationships obtained cross the zero strain axis at varying values ranging from 10.5μm to 32μm, this was in fact checked by taking samples at zero strain, these results were found to be in good agreement with the relationships obtained. There are two possible reasons for this value a) this is the damage associated with the testing procedure (i.e. during the cleaving open of the notches at -196°C) or b) this is the damage formed during the history of the material (i.e. during manufacture).

When there is a higher density of carbides present in the material, the value of the A.N.N.D. decreases at a more rapid rate with increasing strain. This can be seen by comparing the results of steel H1 (medium carbide content, medium slope) with steel H2 (higher carbide content, steep slope). The converse can also be seen by comparing steel H1 with steel H3 (low carbide content, shallow slope).

Every time observations of voids are made there is a size limit below which a void is undetectable and so one possible explanation of the above is that with increasing strain the growth of the voids under the action of hydrostatic

stresses has caused a greater number to be within the detectable size range. Hence the density of voids appears to increase. Alternatively, there could be additional void nucleation events taking place with increasing strain and that the increase in void density is due to more voids being present in the material.

However, because of the relationship between carbide particle densities and the rate of change of the A.N.N.D. values of the voids, the latter explanation is the more likely. The reason for this being that the size of a carbide particle is large enough to be detected by the stereoscan technique and that the size of a void nucleated by a particle is of the same order of size as the particle itself.

Further support of this is found in the lack of difference between the H and H 30 plots for each material (Fig.38b, c, d and Fig.38e, f, g respectively). If the voids were pre-existing at an undetectable size and then growing to detection the H 30 plot would be expected to be appreciably different to the H plots as the hydrostatic tension acting on the central section of their notch planes is appreciably lower (from a Bridgman (53) type stress analysis c.f. section 8.4.2).

This lower value of hydrostatic tension would lead to a slower growth to detection in the H 30 specimens than in their equivalent H specimens thus giving a lower slope to their A.N.N.D. plots.

Thus the only way in which there could be an increase in the A.N.N.D. value is through a process of continual nucleation of new voids at carbide particles with increasing strain.

8.4.2 Effect of strain on the range of void sizes

From Fig.39a, b, c, d, e and f it can be seen that at low strains the size range of voids varies from 0.3μm to 0.7μm. As the amount of plastic strain increases the size range increases because of a gradual enlarging of the upper limit of void sizes. The lower limit remains constant with increase in strain.

This is indicative of two processes occuring together. The lack of change in the lower limit is consistent with the concept of the continuous nucleation of voids with strain at sources of stress concentrations (see section 8.4.1).

It is believed that the principal sources of stress concentrations are the carbide particles in the spheroidised steels which have size ranges of 0.4μm to 0.8μm for H1, 0.3 to 0.65μm for H2 and 0.3μm to 0.55μm for H3, which tie in well with both the constant lower limit observed and with the initial size range.

Secondly the increase in the upper limit of size ranges with strain is thought to be a consequence of void growth during straining. This growth being brought about by plastic deformation of the metal under the action of combined hydrostatic and shear stresses.

All the above measurements were carried out on observations of voids in the centre of the fractured area so that the stress and strain histories of all of the measurements would be consistent. As can be seen from Fig.32, where the Bridgman (53) stress analysis is plotted against position, any area in the central quarter of the specimen will have a virtually identical stress history.

8.4.2.1 <u>The upper limit of void sizes as a void growth curve</u>

If the upper limit of these size ranges can be considered to be representative of the growth history of the

first void nucleated during the deformation we have, using the upper limit line only, a set of curves for the growth of voids under known applied plastic strains, and if a suitable stress analysis of this region can be obtained these will be growth curves under known stress and strain systems.

8.4.2.2 Stress analysis of the central region of the specimen

The appropriate stress analysis for this instance is probably that the Bridgman (53) (see section 2.10).

From the above mentioned stress analysis an estimate of the stress system in the central region of the bar can be made:-

$$\sigma_\theta = \sigma_r = \bar{\sigma} \ln \left(\frac{a^2 + 2aR - r^2}{2aR} \right)$$

where a = ligament radius

R = notch root radius

r = position from centre line

at, or near, the centre of the bar we may consider r to be equal to zero

therefore:

$$\sigma_\theta = \sigma_r = \bar{\sigma} \ln\left(\frac{d}{2R} + 1\right)$$

or

$$\frac{\sigma_r}{\bar{\sigma}} = \ln\left(\frac{d}{2R} + 1\right)$$

8.4.2.3 Prediction of void sizes

From M^{c}Clintock's (64) analysis of hole growth we have the following expression

$$\frac{d\eta}{d\varepsilon} = \frac{\sinh\left[(1-n)(\sigma_a + \sigma_b)/2\bar{\sigma}/\sqrt{3}\right]}{(1-n)\ln F^f}$$

where

$$d\eta = \ln F / \ln F^t$$

$$F = b l_o / b_o l$$

$$F^t = l_o / b_o$$

b = void diameter

l = void centre spacings

σ_a , σ_b = transverse stress components

Cross multiplying we have:-

$$F = \exp\left\{ \frac{d\varepsilon \sinh\left[(1-n)(\sigma_a+\sigma_b)/2\bar{\sigma}/\sqrt{3}\right]}{(1-n)} \right\}$$

or

$$b = \frac{b_o l}{l_o} \exp\left\{ \frac{d\varepsilon \sinh\left[(1-n)(\sigma_a+\sigma_b)/2\bar{\sigma}/\sqrt{3}\right]}{(1-n)} \right\}$$

Assuming that, for our situation, $\sigma_a = \sigma_b = \sigma_r = \sigma_\theta$ and also assuming that $\varepsilon_2 - \varepsilon_1$ can be substituted for $d\varepsilon$ the expression becomes:-

$$b = \frac{b_o l}{l_o} \exp\left\{ \frac{(\varepsilon_2-\varepsilon_1) \sinh\left[(1-n)\sigma_r/\bar{\sigma}/\sqrt{3}\right]}{(1-n)} \right\}$$

Thus if the stress state for each small increment of strain is known the void size can be predicted using M^{c}Clintock's void growth theory.

Before this expression can be used in this way the following assumption concerning void centre spacings is required.

In the material being considered here, there appears to be continual void nucleation during straining, thus the value of l is changing for reasons other than the applied plastic strain. Because of this artificial values of l and l_o are necessary. If we assume an initial value of l of 20μm which will reduce with applied plastic strain ε_p :-

$$\frac{l_o}{\exp(\varepsilon_p/2)} = l_o'$$

Therefore, with the use of this substitution appropriate values of the centre spacings can be estimated, which are realistic for the model being used.

From the information laid out in Tables 1d to 1g it is possible, via the above mentioned Bridgman analysis, to calculate the stresses in the central section of each notch at any point in time. Graphs of the notch root radius (ρ) against the applied strain were plotted and from 'best fit' curves drawn through these points the notch root radius could be read off for any strain. These values were fed into a simple computer programme at strain intervals of 0.01, this programme embodied all the above calculations and thus for any initial void size it gives us predicted void sizes resulting from the notch deformation data fed into it. The results of these calculations are plotted out in Fig.46. The most obvious point of these plots is the fact that the two sets of specimens fall into two distinct sections, the H series predictions all show very similar curves but have a much higher growth rate than the H 30 series, which themselves all show similar growth predictions. These two sets of predictions quite simply demonstrate the expected effect of varying the hydrostatic tension upon the growth rate of the voids (see section 2.12). The difference within each of these groups could quite easily be due to the different starting points given to the computer programme, depending upon the amount of information available for each set of notches.

8.4.2.4 Comparison of predicted and observed void sizes

The observed void growth curves* of Fig.39a, b, c, d, e and f also show this grouping in that the curves of Fig.39a, b, c (the H series curves) show a markedly higher growth rate than those of Fig.39d, e, f (the H 30 series) i.e. these results point to the fact that the higher the hydrostatic tension the higher the void growth rate.

This particular observation agrees, in principle at least, with all of the known theoretical work carried out on the growth of voids (63,64,65,66) (see sections 2.7 and 2.12), where it is generally concluded that the void growth rate will be markedly increased by an increase in the hydrostatic tension acting on the material.

Although there is a qualitative agreement between the predictions of Fig.46 and the observations shown in Fig.39a to f there is a considerable discrepancy between the actual predicted sizes of the voids and these observations. If material H1 is

---

* Assuming that the upper limits of the void size envelopes can be considered to represent void growth curves.

considered at a strain of say 0.275 the actual void size is about 1μm whilst the void size predicted from M^{c}Clintock's (64) analysis (Fig.46) is about 3μm, i.e. an overestimation of the void's size by a factor of about three. This error is about the same for all three of the H series specimens at this order of strain, and increases with increase in strain. The predictions for the H 30 specimens are again overestimations, but not by such a large amount, H1 - 30 at a strain of 0.275 had an actual void size of about 0.8μm whilst the prediction suggests a void size of 1.25μm, i.e. only an overestimation of around 50%. All of the H 30 predictions overestimate the actual size by about the same amount, and again the error increases with increase in strain.

This discrepancy between the predicted and observed void sizes may not be entirely due to the growth theory being used, but could to some extent be due to the stress analysis being employed. Although recent (85,86) investigations of the applicability of the Bridgman (53) analysis to the type of pre-notched specimens used here have indicated that there is little error in his (Bridgman's) analysis when it is used to analyse the stresses at or near the centre of the bar. Therefore, for the H series specimens the overestimation of void sizes from M^{c}Clintock's analysis must be due to an oversensitivity of his

analysis to the hydrostatic tension acting on the material. In the case of the H 30 series, where the hydrostatic tension is lower, the error is much less and could perhaps be accounted for in the accumulation of several small errors, including errors in the stress analysis, although it does tend to again indicate an oversensitivity of the predictions to hydrostatic tension.

This observation is of importance when considering failure criteria based upon existing growth theories, i.e. in Fig.11 where such theories overestimate the failure strain by about a factor of two, but if the above observations were to be injected into this a growth to coalescence theory would overestimate the strain to failure by a far greater amount, especially under conditions of high triaxiality, thus underlining the importance of void coalescence as a separate and important mechanism.

8.4.2.5 The lower limit of void sizes as a representation of void nucleation

The lower bound to these void size envelopes (Fig.39a to f), as already briefly mentioned, is believed to represent the continual nucleation of voids at the carbide particles. This

line cannot be considered to represent all the voids being nucleated as there could be voids larger than this minima nucleated throughout the process, as there are at the start, i.e. when $\varepsilon_p = 0$ there is a spread of void sizes. Nevertheless these lines can be considered to represent the minimum size of void nucleated at each increment of plastic strain (given that they are not undetectable voids growing to detection, see section 8.4.1).

8.4.2.6. Comparison of this nucleation plot with the available theories

The available theoretical models of void nucleation for the system being considered here (see section 2.5 and the first four pages of section 2.12) indicate that there should be a size effect of void nucleation with respect to strain (38, 5, 42, 43), in that larger particles should form voids earlier in the process than smaller ones. From this it would be expected that the lower bound to the void size envelopes of Fig.39a to F would not be horizontal lines showing no size effect but should show a slope such that the size detected decreases with increase in strain. Although the lower lines of Fig.39 can only be considered to be the minimum size of void nucleated during straining this observation is in basic disagreement with these

theories. These observations, however, do agree with the predictions of Tanaka et al. (39) who, for the range of particle sizes being considered here, predicts no size dependency from a theory which requires both an energy and a stress criteria to be met before voiding can take place. Brown and Stobbs (41) in both their observations and theoretical model come close to the observations found here, in that they predict a weak dependency of nucleation strain on particle size (small particles voiding first), but observed a weak trend going the other way (large particles voiding first). The observations of Easterling, Fishmeister and Navara (10) may also agree with those found here in that they detected only a weak trend of small particles voiding first but also observed that widely differing sizes of voiding particles were apparent regardless of the applied strain. Thus a lower bound to Easterling et al's. observations could easily be very similar to that detected here.

Thus the lower bound to the void size envelope, which may be considered to be associated with the nucleation of voids, can be explained by some of the published material, namely the theoretical predictions of Tanaka et al. and the observations of Easterling et al. Although the majority of the published literature does not indicate this type of lower bound to the size envelope.

8.4.3 Notch sections

Similar notches to those which were cleaved open were sectioned and examined. These sections show small cracks being propagated from the root of the notch (plate 7) which, as is clear from the topography, are the result of void coalescence. The type of damage in the material from which this crack forms can be seen in plate 7a and can be seen to be all along the front of the notch tip (as one might expect from classical fracture mechanics theory where a blunt notch could be expected to have a large plastic zone). Damage, or rather voids, of this type could not be found in the bulk of the material, indicating that the stress and strains associated with the notch are controlling the fracture rather than those in the central region of the specimen i.e. this again suggests that the controlling stress system is nearer to that of the elastic situation than that of the necking tensile bar.

This notch damage, in general, being limited to a region less than 250μm in front of the notch tip.

Fig.47 shows the expected stress system operating under a notch, such as the ones discussed above, based on Neuber's

(82) elastic stress analysis which has been reduced to the plastic case by using his (Neuber's) relationship (83):-

$$\left(K_{\sigma_p} \cdot K_{\varepsilon_p}\right)^{1/2} = K_T$$

and Weiss's (87) strain concentration analysis for notches (see Appendix A for details).

This diagram indicates that as the notch blunts (i.e. the notch root radius increases) the position of maximum stress triaxiality changes. As the notch blunts the position of maximum triaxiality moves further away from the notch tip. Thus an area of accelerated damage would be expected to be found at some distance under the notch. The damage observed in plate 7a is plotted on this diagram (Fig.47) and it can be seen that there is a reasonable agreement between the damaged area and the positions traced out by the areas of high triaxiality during the straining (change in notch root radius) of the notch.

8.4.4 Edge analysis of cleaved notches

Fig.40a, b, c, d, e and f show the notch root damage in terms of the A.N.N.D. value associated with 10μm strips running parallel to the notch root. From these plots it can be seen that there is a constant amount of damage running for some distance in front of the notch before there is a smooth rise in the A.N.N.D. value i.e. the damage decreases.

8.4.4.1 Prediction of edge damage

Using the strain concentration analysis of Weiss and the damage rate equations formulated from the A.N.N.D. V's ε_p graphs (Fig.38) an attempt can be made to predict this damage concentration associated with the notch roots.

The strain concentration is

$$\varepsilon_y = \varepsilon_n \left(K_T \sqrt{\rho/4}\right)^{2(n+1)^{-1}} x^{-(n+1)^{-1}}$$

where ε_y = strain at a distance x beneath the notch

ρ = notch root radius

ε_n = remote strain

n = work hardening index

As the damage rate equations take the form:-

$$A.N.N.D. = A - B\ \varepsilon_p$$

where A and B are constants

ε_p is the applied strain

Substituting ε_y for ε_p the A.N.N.D. value for any position x beneath the notch tip can be calculated.

8.4.4.2 Comparison of predicted and observed damage

The results of these calculations for notches H1 - 5, H1 - 4, H1 - 3, H3 - 5, H3 - 3, H3 - 1 are shown in graphical form in Figs.40a to f superimposed upon the actual measured values obtained from micrographs of the appropriate areas.

As can be seen from these graphs the predictions are in good agreement with the curved section of the results graph but do not predict the horizontal, or maximum damage, part of the observations. Nevertheless these plots show that the linear damage equations are capable of being extrapolated, without loss of accuracy, to well beyond the limits of the original observations.

8.4.4.3 The maximum damage level

The maximum damage levels demonstrated by these observations do not appear to initially correlate to any of the carbide distributions, i.e. one might expect the maximum value of A.N.N.D. to be the same as the carbides planar spacing in a slice of material one carbide diameter deep (as found by Widgery and Knott (92) with inclusions in 'dirty' weld metals) but this would give a value of 0.5 and 2.0μm which is an under estimation of the minimum A.N.N.D. value found by a factor of about 2. Thus we are left with the conclusion that the damage rate equations are only applicable to some value of A.N.N.D. which is not the same as the minimum spacing of the nucleants.

This cut-off of void nucleation at a value of A.N.N.D. above any expected level based on the spacing of available nucleating particles is initially inexplicable. From the previous findings and published literature it would have been reasonable to expect the nucleation to continue until either all possible nucleation sites have voided or inter-void instability has intervened causing metal separation, and hence an end to any further deformation and nucleation. However most of the theories and models for void nucleation only consider one voiding particle in an infinite matrix, if two neighbouring voiding particles are considered then their reaction on each other must be considered,

both before and after one of them voids. Before voiding there will be a back stress or reaction between the two particles. This back stress may be considered to be represented in the nucleation criteria of Ashby (38) by the value of 'b', the particle spacing (see section 2.5 or 2.12). If one of these particles voids then this back stress will be vastly reduced (more than half perhaps) and the likelyhood of the second particle nucleating a void diminished. If this is in fact the case and has reached such an extent in the situation mentioned above that the forces acting on all the remaining cohesive particles have been reduced in this way then this would be a possible explanation for this value of maximum damage (minimum A.N.N.D.). Under these circumstances the minimum value of A.N.N.D. would not be the carbide planar spacing but very roughly twice this value. In our case between 1.0 and 4.0μm, which is in good agreement with the values found.

8.4.5 Summary of the multi notch specimens

As a model for the events taking place in these specimens we have the following:-

a) Continuous nucleation of voids at carbides at a rate linearly connected to the strain in that area until such a time as the maximum damage is

achieved, this maximum damage being about equal to twice the carbide planar spacing.

b) Exponential growth of voids with respect to the hydrostatic stress system, but at an appreciably lower rate than that expected from the void growth theory of M^{c}Clintock (64).

c) A complicated system of stress related and strain related damage just under the notch tip. This damage being nucleated by a strain concentration which is moving out from the notch tip, and growing under a stress triaxiality which is also moving away from the notch tip with increasing strain, or notch opening. As these two systems start to interact the total damage for any one area will be rapidly accelerated until the size-spacing-stress state relationships satisfy an instability criteria (such as Thomasons (71)) and void coalescence takes place to form a crack which will both link back to the notch tip and grow further into the material by repeating the above process.

The final room temperature fracture surface, in all cases, is one of an outer ring of ductile fracture with an inner ring of cleavage, the reason for this could be a) the crack velocity could have reached sufficient speed for the material to be effectively below its ductile/brittle transition temperature, although it has been reported by Smith (94) that a ductile crack tends to slow down as its length increases rather than accelerate, but in this case the stored elastic energy in the relatively large specimen may have been sufficient to cause acceleration. b) The material in the core may have undergone enough strain to work harden it to such an extent that insufficient ductility remains for void growth and thus failure by cleavage is the preferred system, but the strains at the notch tips have been far greater than in the core, thus the exhaustion of ductility can be ignored and therefore the first alternative is the more likely.

8.5 Charpy impact tests

Comparing the impact results obtained for steels H1, H2 and H3 (table 5) to the damage rate equations obtained from the A.N.N.D. V's ε_p graphs (Fig.38 and table 2) it can be seen that there is a rough, not altogether unexpected, relationship between the rate of damage accumulation and the impact properties of the material, i.e. the material with the highest rate of damage accumulation (H2, A.N.N.D. V's ε_p slope of 37) has the lowest impact resistance of 139 Joules

whilst the material with the lowest damage rate (H3, A.N.N.D. V's ε_p of 10) has the highest impact resistance of 240 Joules. These results demonstrate the effect that the damage rate has upon the deformation required to cause failure i.e. there will be no void coalescence until a sufficient void concentration has been reached. In the context of material stability the position of the dilational surface in Fig.23 will be controlled, partly at least, by the number of voids in the material and for this surface to move nearer to the active stress point there will have to be more deformation to cause both further void nucleation and void growth until this surface is brought into contact with the active stress point and thus causing the material to fail.

The impact values of the 50D steel are also shown in table 5 and these are of interest in so far as the effect of orientation on these values is concerned. When these values are compared to the macros of their fracture surfaces (plate 8) and the highly orientated microstructure shown in plate 10, the reason for the vast difference in impact resistance becomes clear. Large macro voids can be seen on the fracture surface which are the result of nucleation and growth of voids from large macro inclusions, these inclusions (and therefore the voids) have different cross-sectional measurements, depending upon their orientation. As these voids grow they will eventually reach a point at which instability is imminent by void sheeting

between them, this point being controlled by the size and spacing of the smaller sheet voids which will be growing under stress systems in between the macro-voids, these stress systems being dependent upon the size and spacing of the macrovoids which are controlled by orientation, thus, dependent upon the initial orientation of the macro-inclusions the final fracture by void sheeting will be controlled.

8.6 Three point bend specimens

Plate 11 and Fig. 43 show the surface of these fractures after having been broken open under liquid nitrogen, a thumbnail of imminent ductile fracture can be seen about 1mm below the notch root, in the area leading up to this thumbnail no comparable voiding could be found. This is merely a demonstration of the stress distribution i.e. the triaxial stresses build up to a maximum at some distance away from the notch tip, that distance being roughly equal to the notch root radius.

The practical implication of this test is probably far more important than the theoretical one in that an appreciable amount of subsurface cracking can take place before it can be detected from the surface i.e. in service such a bend

may be discounted as merely that, a bend, when in fact a crack of considerable size has been formed which could prove catastrophic at some time in the future.

8.7 Sheet aluminium specimens

Fig.44 shows the form of the imminent shear failure, the direction of the shear having been considerably influenced by the presence of the artificial voids (i.e. the fracture would have been expected to form at 45° to the applied stress axis). As both the stress system and the scale are considerably different to the previous cases the applicability of the test may be questionable but it nevertheless gives a qualitative indication of the effect of voids on the local stress system i.e. when voids become large with respect to their spacing thay cannot be considered in that stress system without their reaction to that system being considered.

8.8 Practical implications

As mentioned in section 8.6 a large amount of sub-surface damage may take place before it can be detected from the surface. Bends of the nature described may be discounted as just that, a bend, but should there be a change in

environment then such damage could prove fatal to the integrity of the structure.

Damage of this type may not necessarily be caused by accidental overstressing of a component but could easily be introduced during the fabrication process, or during the assembly or repair of a structure.

This type of damage may be introduced at relatively low levels of applied strain, considerably lower than has generally been realised; resulting in permanent irreversible damage which over a period of repeated small strainings could accumulate to such an extent to cause failure.

The rate, or the ease, with which a ductile crack propagates must depend upon the amount of pre-existing damage in the material. If a component has been heavily deformed under the actions of a fairly high level of hydrostatic tension then any ductile crack or tear will pass through it fairly easily. If the material is relatively undamaged then it will offer much more resistance to the growth of any ductile crack, as the crack will have to generate all its own damage required for the final material separation.

The various processes which cause a ductile fracture are reasonably well understood, and in most cases can be predicted by the existing theories to an accuracy well within one order of magnitude. Providing that the designer appreciates the effect of local stress complexities and local strain concentrations, as well as the effect of macro-stresses acting on a component, then he should be able to safely design against the possibility of failure by ductile fracture without introducing unacceptably high safety factors.

9. CONCLUSIONS

a) In the material considered here void nucleation appears to be a function of strain (if measured as the A.N.N.D. value than as a linear function). This function can be extrapolated, with reasonable accuracy, to levels of strain far above those of the original observations; until a cut off is reached at an A.N.N.D. value about equal to twice the planar spacing of the void nucleants.

b) The growth of voids under the action of hydrostatic tension is of an exponential type, in general agreement with the available theories, but at a lower rate than these theories predict - especially at high levels of hydrostatic tension.

c) There does not appear to be any size dependency of nucleation with strain, at least not on the minimum size of voids nucleated.

d) There is no effect of varying the hydrostatic stresses, over the range considered here, on the rate of void nucleation.

e) The mechanics of ductile fracture can be quantitatively explained by the mechanisms thought to operate.

f) There may be considerable subsurface damage under notches in material which has been plastically deformed. This damage, or crack, will not be detectable from the surface of the material and could easily be of such size as to compromise the integrity of the material.

g) A ductile fracture is more strain controlled than was previously thought. The effect of stresses has, in the past, been overestimated i.e. its effect on void growth is less than predicted, whilst strain controls the void nucleation events.

h) Designs cannot be based on macro-stresses alone. There must be considerations of both the internal triaxial stresses and the micro-strain concentrations.

APPENDIX A

Adaptation of Neuber's (82) analysis

1. Co-ordinate System

Neuber defines a curvilinear co-ordinate system such that:-

$$x = \sinh u \cos v$$

$$y = \cosh u \sin v$$

$$\left(\frac{x}{\sinh u}\right)^2 + \left(\frac{y}{\cosh u}\right)^2 = 1$$

$$\left(\frac{y}{\sin v}\right)^2 - \left(\frac{x}{\cos v}\right)^2 = 1$$

Where x and y are the equivalent linear co-ordinates (Fig.A1).

For a system considering the notch plane only:-

$$x = o \quad \therefore \sinh u = o \quad \therefore u = o$$

thus $y = \sin v$

2. Stress Systems for a Circumferentially Notched Bar

Neuber gives the radial stress as

$$\sigma_v = \frac{1}{h^2}\left\{-A\,\frac{\cos v}{1+\cos v} + (\alpha - 1)\,C\cos v\right\} + \frac{\cos v}{h^4}\left\{A - B - C\cos^2 v\right\}$$

where $h = \sqrt{\sinh^2 u + \cos^2 v}$

but when $x = o$ $\sinh u = o$

$\therefore h = \cos v$

$\alpha = (1 - \nu)2$ ν = Poissons Ratio

Let vo be the curvilinear co-ordinate describing the notch surface.

$$A = (\alpha - 1)(1 + \cos vo)C$$

$$B = A - A\cos^2 Vo$$

$$C = -\frac{p}{2}\,\frac{1 + \cos vo}{1 + (2 - \alpha)\cos vo + \cos^2 vo}$$

$p = \frac{P}{\pi a^2}$ remote stress acting over the notched area

(a = sin vo)

Let Z = cos v

$$\sigma v = \frac{1}{Z^2}\left\{-\frac{AZ}{1+Z} + (\alpha - 1)CZ\right\} + \frac{Z}{Z^4}\left\{A - B - CZ^2\right\}$$

i.e.

$$\sigma v = \frac{-A}{Z + Z^2} + \frac{(\alpha - 1)C}{Z} + \frac{A}{Z^3} - \frac{B}{Z^3} - \frac{C}{Z}$$

in the same way the stress acting in the direction of tension becomes:-

$$\sigma u = \frac{B}{Z} - \frac{C}{Z}(1 + \alpha) + \frac{B}{Z^3} - \frac{A}{Z^3} + \frac{C}{Z}$$

and the hoop stress becomes:-

$$\sigma w = \frac{A}{Z^3 + Z^4} - \frac{B}{Z^3} + \frac{C(\alpha - 2)}{Z^3}$$

In this analysis the actual dimensions are set by the notch root radius (ρ)

$$\frac{a}{\rho} = \tan^2 vo$$

but $a = \sin vo$

$$\therefore \quad \rho = \frac{\cos vo}{\tan vo} = \frac{\cos^2 vo}{\sin vo}$$

Thus a physical scale can be set and the elastic stresses calculated for all three dimensions for any point along the notch plane. For these to be converted into plastic stresses using Neuber's (59) relationship:-

$$\left(K\sigma_\rho \cdot K\varepsilon_\rho\right)^{1/2} = K_T$$

A value for $K\varepsilon_\rho$ for each point along that plane must be derived.

Using Weiss's (60) analysis for strain concentration

$$K\varepsilon_\rho = \frac{\varepsilon}{\varepsilon_n} = \left(K_T\sqrt{\rho/4}\right)^{2(n+1)^{-1}} \quad \propto^{-(n+1)^{-1}}$$

where

K_T = stress concentration factor (i.e. σ_u/σ^∞ at a = sin vo)

ρ = notch root radius i.e. = $a/\tan^2 vo$

x = position = sin vo - sin v

n = work hardening index

This value of $K\varepsilon_p$ is parallel to the direction of applied stress, the strain in the other directions (v and u) will be:-

$$K\varepsilon_{pv} = K\varepsilon_{pw} = K\varepsilon_{pu}/2$$

Thus we have all the necessary values to determine the three principal plastic stresses acting at any one point on the notch plane.

If for a value of the triaxiality at any point we use the non-dimensional quantity

$$\sigma_m/\bar{\sigma} \qquad \sigma_m = \frac{\Sigma \sigma_{ij}\ \delta_{ij}}{3}$$

$$\bar{\sigma} = \left(\tfrac{1}{2} \Sigma (\sigma_i - \sigma_j)^2\right)^{\frac{1}{2}}$$

which can easily be calculated from the above formula. Using a simple iterative computer programme to determine the position and magnitude of the maximum triaxiality, the graph shown in Fig.47 may then be constructed.

Fig. A1

Curvy linear co-ordinate system

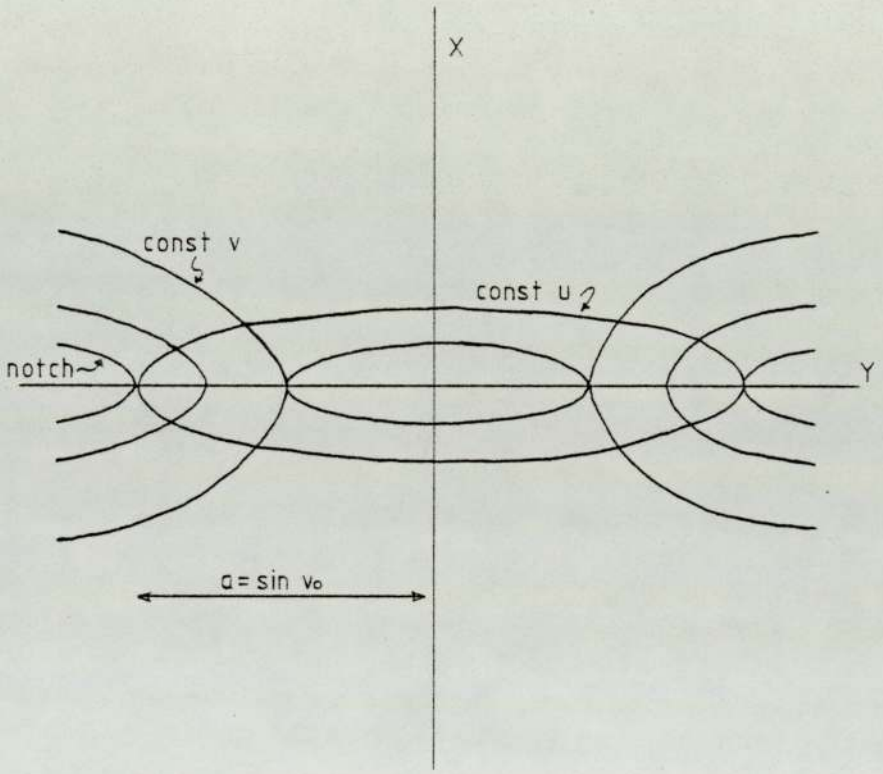

REFERENCES

1. A. R. Rosenfield
   Met. Reviews (No.121) 13 29 (1968)

2. H. C. Rodgers
   Ductility, A.S.M., Metals Park, 31 (1968)

3. M. A. Greenfield and H. Margolin
   Met. Trans. 3 2649 (1972)

4. A. S. Argon, J. Im and R. Safoglu
   Met. Trans. 6A 825 (1975)

5. J Gurland and J. Plateau
   Trans. A.S.M. 56 442 (1963)

6. E. Rosorsky, W. C. Hahn and B. Avitzur
   Met. Trans. 4 927 (1973)

7. J. Ganglie and J. Gurland
   Trans. of Metal Soc. of A.S.M.E. 239
   269 (1967)

8. T. C. Lindley, G. Oates and C. E. Richards
Acta Met. 18 1127 (1970)

9. J. Gurland
Acta Met. 20 735 (1972)

10. K. E. Easterling, H. F. Fishmeister and E. Navara
Powder Met. 16 128 (1973)

11. K. E. Puttick
Phil. Mag. 4 964 (1959)

12. C. F. Tipper
Metallurgica 39 133 (1948)

13. D. Broek
Eng. Fract. Mech. 5 55 (1973)

14. B. I. Edelson and W. M. Baldwin
Trans. A.S.M. 55 230 (1962)

15. C. Crussard, R. Boraine, J. Plateau and F. Maratory
J.I.S.I. 183 146 (1956)

16. H. C. Rodgers
Trans. A.I.M.E. 218 498 (1960)

17. T. B. Cox and J. R. Low
Mat Trans. 5 1457 (1974)

18. J. I. Bluhm and P. J. Morrissey
Proc. First Int. Conf. Fract. (Vol.3)
Japan Soc. Strength and Stracture.
Sendai 1739 (1966)

19. I. G. Palmer, G. C. Smith and R. D. Warda
Physical Basis of Yield and Fracture.
Inst. of Physics London 53 (1967)

20. C. A. Berg
Inelastic Behaviour of Solids. Ed
Kannine et al. McGraw Hill N.Y.
171 (1970)

21. I. L. Dillamore and R. A. Maynard
British Steel Dev. Lab. Rpt.
CDL/MT/9/74 (1975)

22. I. G. Palmer and G. C. Smith
Oxide Dispersion Strengthening,
Gordon and Breach New York 253 (1968)

23. C. D. Calhoun and N. S. Stoloff
Met. Trans. 1 997 (1970)

24. T. Gladman, B. Holmes and I. D. McIvor
Effects of Second Phase Particles on
Mechanical Properties of Steel. Iron
and Steel Institute. London 68 (1971)

25. T. Inous and S. Kinoshita
Proc. Third Int. Conf. on Strength of
Metals and Alloys. Inst. Metals,
Cambridge 159 (1973)

26. F. D. Rosi and M. S. Abrahams
Acta Met. 8 807 (1960)

27. R. W. Bauer and H. G. F. Wilsdorf
Scripta Met. 7 1213 (1973)

28. J. A. Alic and R. M. Asimov
Eng. Fract. Mech. 4 915 (1972)

29. A. Van Den Beukel

Vacancies and Interstitials in Metals

North Holland Amsterdam 427 (1969)

30. D. R. Miller and F. M. C. Besog

Proc. First Int. Conf on Fract. (Vol 2)

Sendai Japan 711 (1966)

31. W. A. Backhofen

Fracture of Engineering Materials,

A.S.M. Metals Park 107 (1964)

32. G. Y. Chin, W. E. Hosford and W. A. Backhofen

Trans. A.I.M.E. 230 437 (1964)

33. B. I. Brindley and T. P. Lindley

J.I.S.I. 210 124 (1972)

34. D. Broek

Int. Met. Rev. 135 (1974)

35. B. R. Butcher

A.E.R.E. Report No. R 7314

36. E. Smith and J. T. Barnby
Met. Soc. J. 1 1 (1967)

37. A. N. Stroh
Proc. Royal Soc. A 223 404 (1954)

38. M. E. Ashby
Phil. Mag. 14 1157 (1966)

39. K. Tanaka, T. Mori and T. Nakamura
Phil. Mag. 23 1201 (1971)

40. J. D. Eshelby
Proc. Roy. Soc. A 241 1201 (1957)

41. L. M. Brown and W. M. Stobbs
Phil. Mag. 23 1201 (1971)

42. B. I. Kleverbring and R. Mahrs
Scand. I. Met. 2 310 (1973)

43. Masayuki Toya
Int. J. Fract. 9 463 (1973)

44. N.I. Muskhelishvili

'Some Basic Problems of the Mathematical Theory of Elasticity'. English Translation by J. R. M. Radok and P. Nordhoff (1953)

45. B. Sundstorm

Eng. Fract. Mech. 6 483 (1974)

46. G. R. Irwin

J. Appl. Mech. 24 361 (1957)

47. T. C. Lindley, G. Oates and C. E. Richards

Proc. Conf. by The Corporate Laboratories of the British Steel Corporation and the Iron and Steel Institute. Scarborough 54 (1971)

48. I. L. Dillamore

Proc. Conf. by the Corporate Laboratories of the British Steel Corporation and the Iron and Steel Institute. Scarborough 64 (1971)

49. J. W. Hancook, I. L. Dillamore and R. E. Smallman
High Temperature Materials, 6th Plansee Seminar Reutte/Tyrol 467 (1968)

50. J. Knott
Inclusion and their effects on steel properties. B.S.C. Conf. Boddington Hall Leeds University September (1974)

51. H. C. Burghard Jr.
Met. Trans. 5 2085 (1974)

52. V. K. Sarin and N. J. Grant
Met. Trans. 3 875 (1972)

53. P. W. Bridgman
Studies in large plastic flow and fracture. Harvard University Press. Cambridge Mass. (1952)

54. C. D. Beacham
Trans. A.S.M. 56 318 (1963)

55. J. T. Barnby
Acta. Met. 15 903 (1967)

56. C. T. Liu and J. Gurland
Trans. A.S.M. 61 156 (1968)

57. D. P. Clausing
Journal of Materials J.M.A.S.A. 4
473 (1969)

58. D. P. Clausing
Int. J. Fract. Mech. 6 71 (1970)

59. J. R. Low, R. H. Van Stone and R. H. Merchant
N.A.S.A. Tech. Rpt. # 2 NGR
39 - 087 - 003 (1972)

60. T. B. Cox and J. R. Low
N.A.S.A. Tech. Rpt. #3 NGR
39 - 087 - 003 (1972)

61. T. B. Cox and J. R Low
N.A.S.A. Tech. Rpt. #4 NGR
39 - 087 - 003 (1972)

62. D. Broek
National Aerospace Lab. (N.L.R.)
The Netherlands N.L.R. T.R. 72029 u (1972)

63. F. A. McClintock

A.S.M. Seminar, 'Ductility',

255 (1967)

64. F. A. McClintock

Trans. A.S.M.E. Series E (J. Appl. Mech)

35 363 (1968)

65. J. R. Rice and D. M. Tracy

J. Med. Phys. Sol. 17 201 (1969)

66. D. M. Tracy

Eng. Fract. Mech. 3 301 (1971)

67. J. W. Hancock and A. C. Mackenzie

J. Mech. Phys. Solids 24 147 (1976)

68. J. Orr and D. K. Brown

Eng. Fract. Mech. 6 261 (1974)

69. P. F. Thomason

J. Int. Met. 96 360 (1968)

70. J. W. Hancock

4th Int. Conf. on Strength of Metals

and Alloys. Nancy France. 30 Aug. 1976

71. P. F. Thomason
Trans. A.S.M.E. (J. Appl. Mech.)
To be published (1979)

72. R. Hill
The mathematical theory of plasticity.
Oxford University Press (1950)

73. P. F. Thomason
Trans. A.S.M.E. (J. Appl. Mech) 45
678 (1978)

74. W. Roberts, B. Lehtiness and K. Easterling
Acta. Met. 24 745 (1976)

75. M. Naguno
Acta. Met. 21 1661 (1973)

76. A. C. Mackenzie, J. W. Hancock and D. K. Brown
Eng. Fract. Mech. 9 167 (1977)

77. M. J. Cowling, J. W. Hancock and A. C. Mackenzie
4th Int. Conf. on Strength of Metals and
Alloys. Nancy France. 30 Aug. 1976

78. J. W. Hancock, M. J. Cowling and A. C. Mackenzie
Weld. Res. Int. 6 37 (1976)

79. A. P. Green
J. Mech. Math. 6 223 (1953)

80. J. R. Rice and M. A. Johnson
Inelastic behaviour of solids. Kannine et al. McGraw Hill, New York 641 (1970)

81. J. F. Knott
Fracture 1977, Vol. 1, ICF4, Waterloo, Canada (1977)

82. H. Neuber
Theory of Notch Stresses. 2nd Edition (Translation by U.S. Joint Publications Research Services). Washington U.S. A.E.C. Office of Technical Information (1961)

83. H. Neuber
Trans. A.S.M.E. (J. Appl Mech.) 28 554 (1961)

84. K. S. Grewal and V. Weiss

Trans. Am. Soc. Metals 56 790 (1963)

85. J. Earl and D. K. Brown

Eng. Frac. Mech. 8 599 (1976)

86. D. K. Brown and R. M. McMeeking

Fracture 1977 Vo.3 ICF4 Waterloo

Canada (1977)

87. V. Weiss

Fatigue, an interdisciplinary approach

Proc. 10th Sagmore Army Materials Research

Centre. Ed- J. J. Burk, N. L. Reid

and V. Weiss. Syracuse University

Press 179 (1964)

88. H. W. Liu, W. J. Garigan and I. S. Ke

Int. J. Frac. Mech 6 41 (1970)

89. J. R. Rice and J. Rosengreen

J. Mech. Phys. Sol. 16 1 (1968)

90. H. Rodgers

Trans. Met. Soc. A.I.M.E. 218

498 (1960)

91. D. T. Livey and P. Murray

Warmfest und Korrosionsbestandige

Sinterwerkstoffe Springer Berlin

375 (1956)

92. D. J. Widgery and J. F. Knott

Met. Sci. 12 8 (1978)

93. M. D. M. Bain, P. E. Holden and N. Trigwell

Private communication. The

University of Aston in Birmingham

(1978)

94. D. Smith and J. F. Knott

Conf. Proc. Practical applications of

Fracture Mechanics to Pressure Vessel

Technology. I.M.E. (1971)

Fig. 1

Fracture from macroinclusions

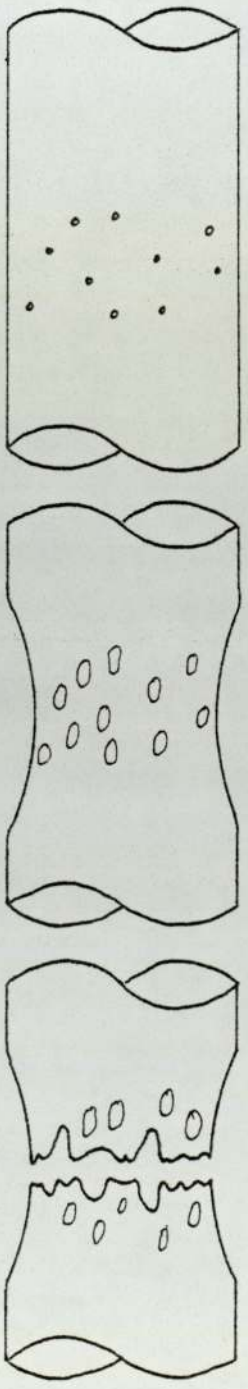

1 Voids nucleate

2 Voids grow

3 Voids coalesce

Fig. 2

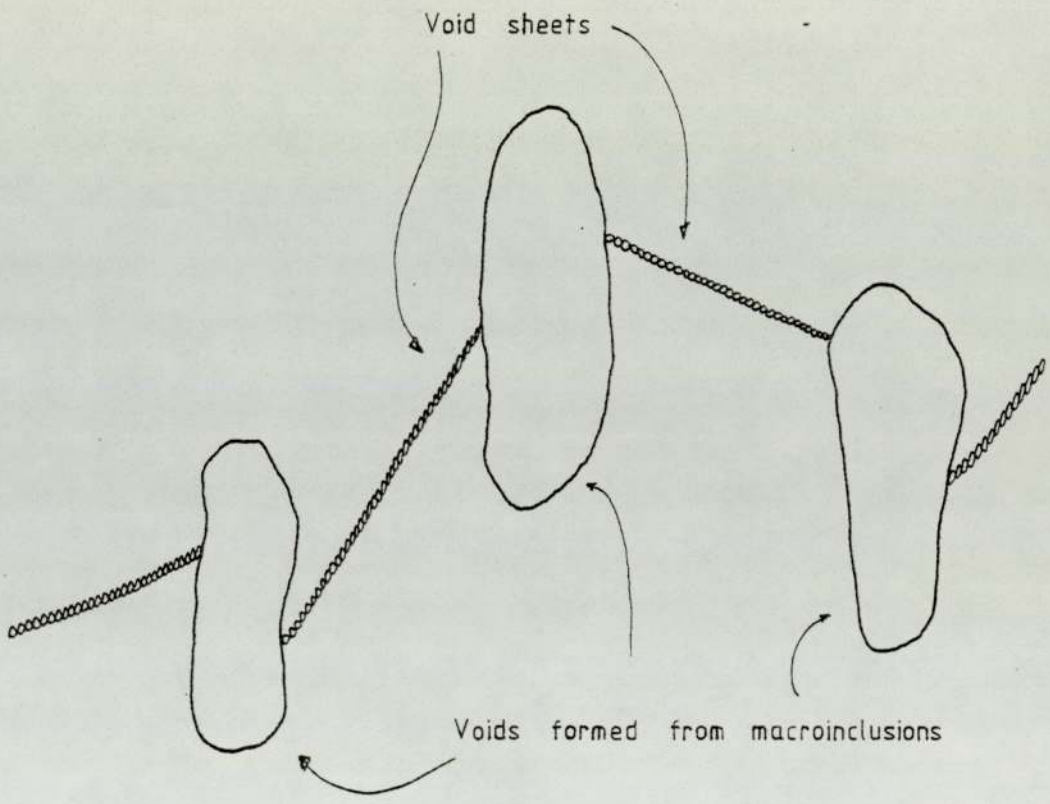

Fig. 3

The Results of Gurland and Plateau

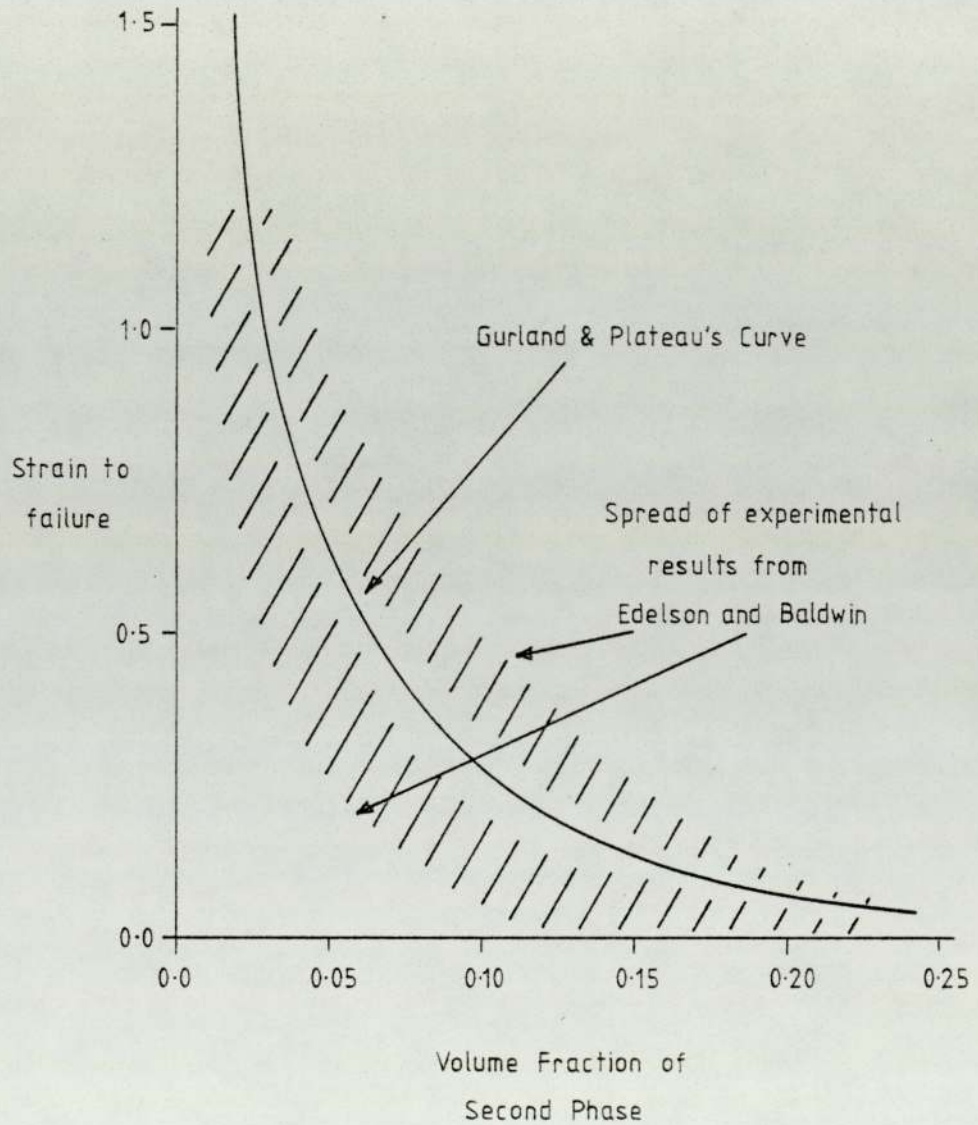

fig 6

Fig. 4

The Fibre Loading Model Of Lindley et al

a)

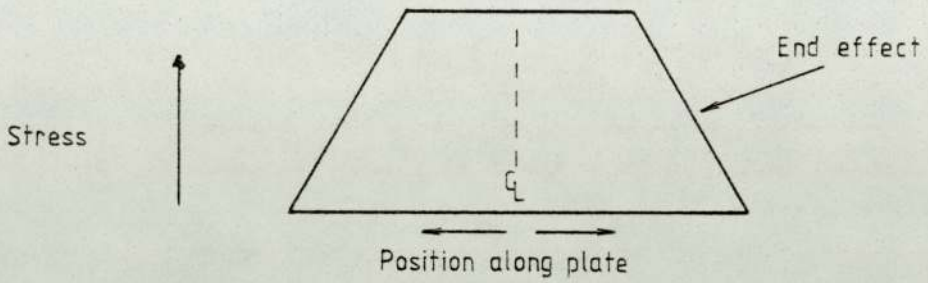

b)

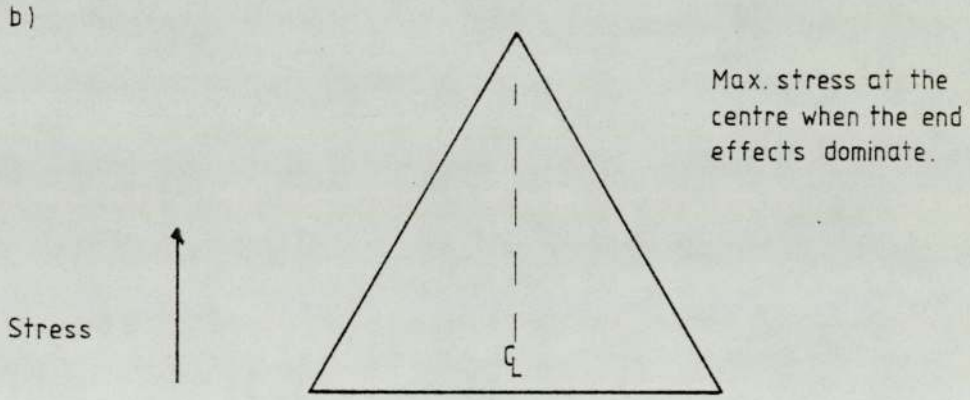

c)

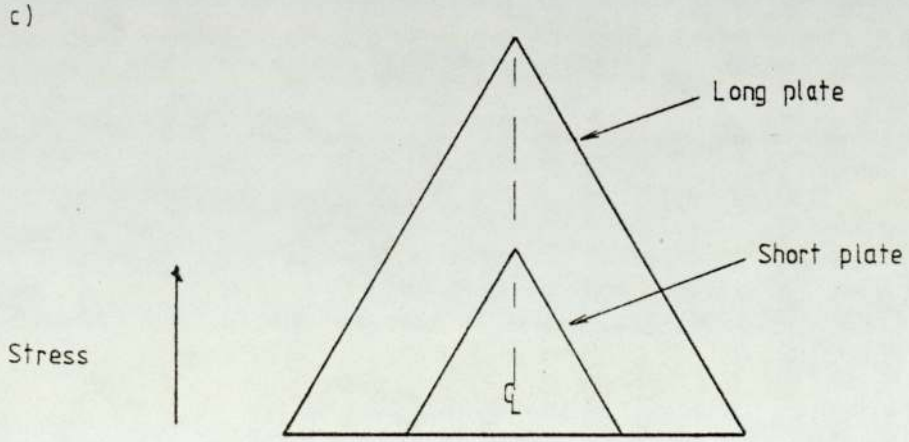

Fig. 5

Relative Magnitudes Of Stresses Around
A Particle — As A Function Of Size
(Afer Butcher)

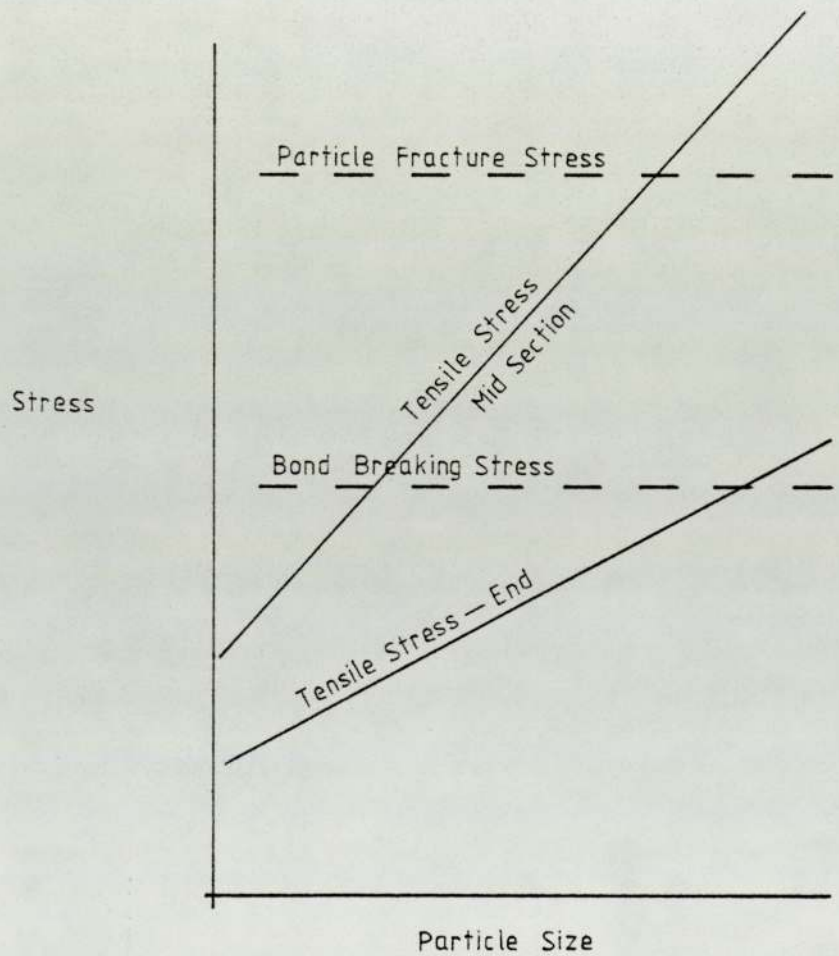

Fig. 6

Void Nucleation (Smith & Barnby)

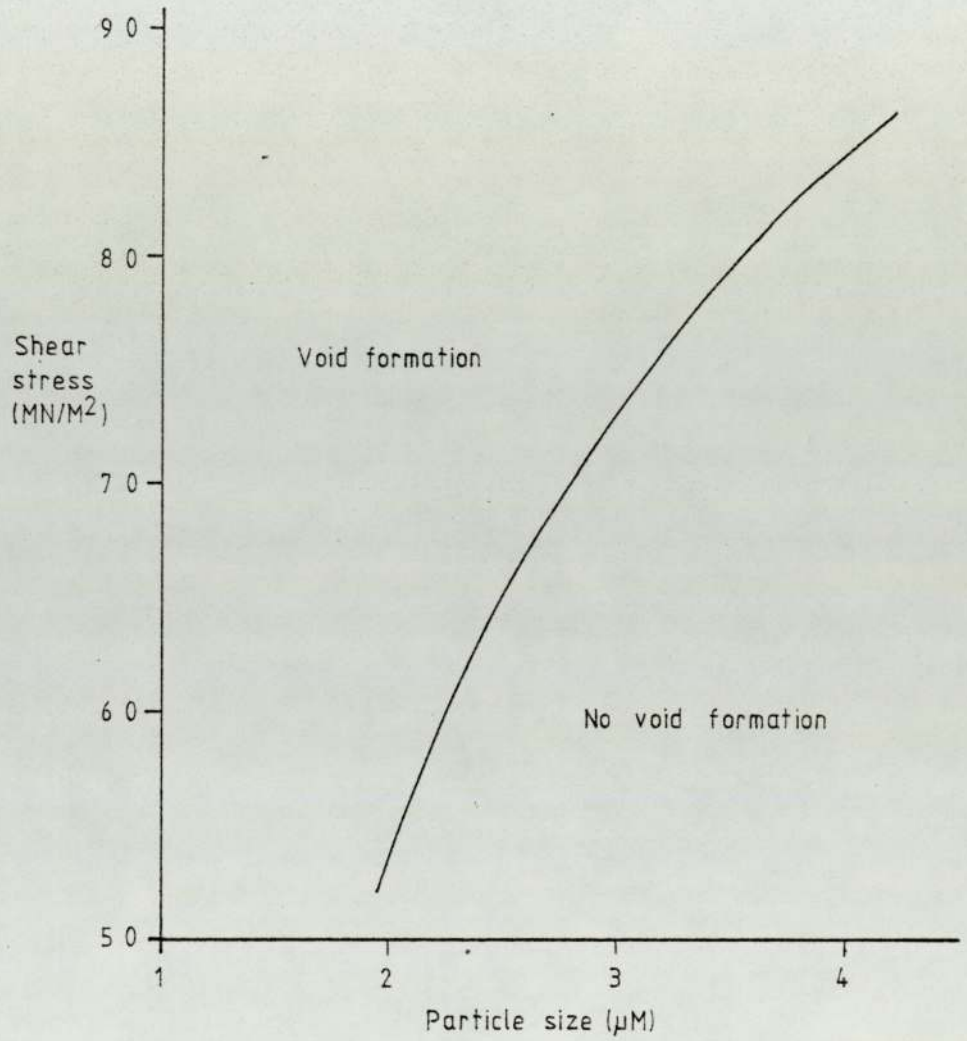

Punching out of dislocation loops (after Ashby)

Ridgid inclusion elastically deformed

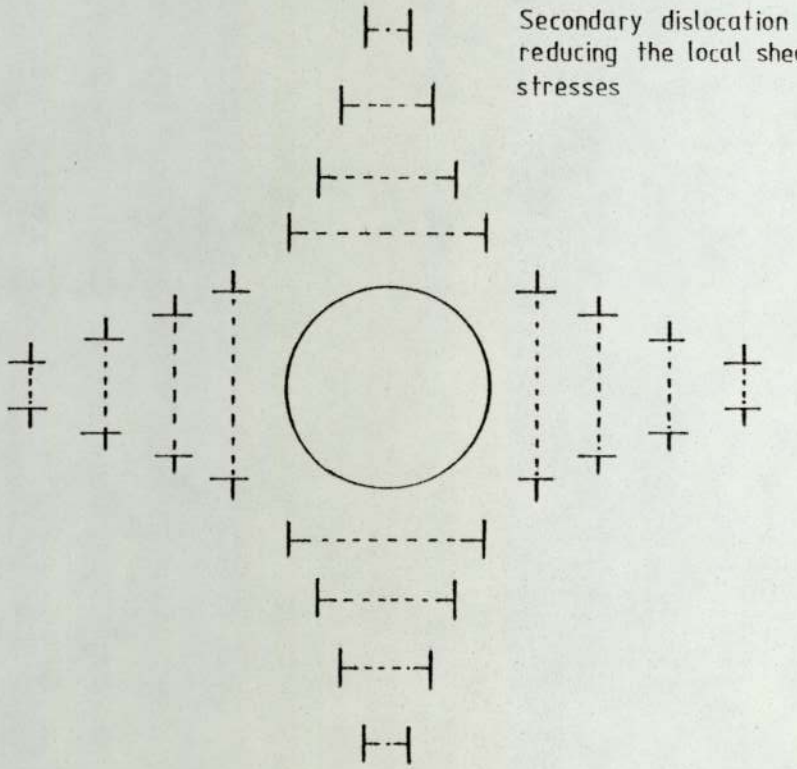

Secondary dislocation loops reducing the local shear stresses

Fig. 7

Fig. 8

Void Nucleation (Ashby)

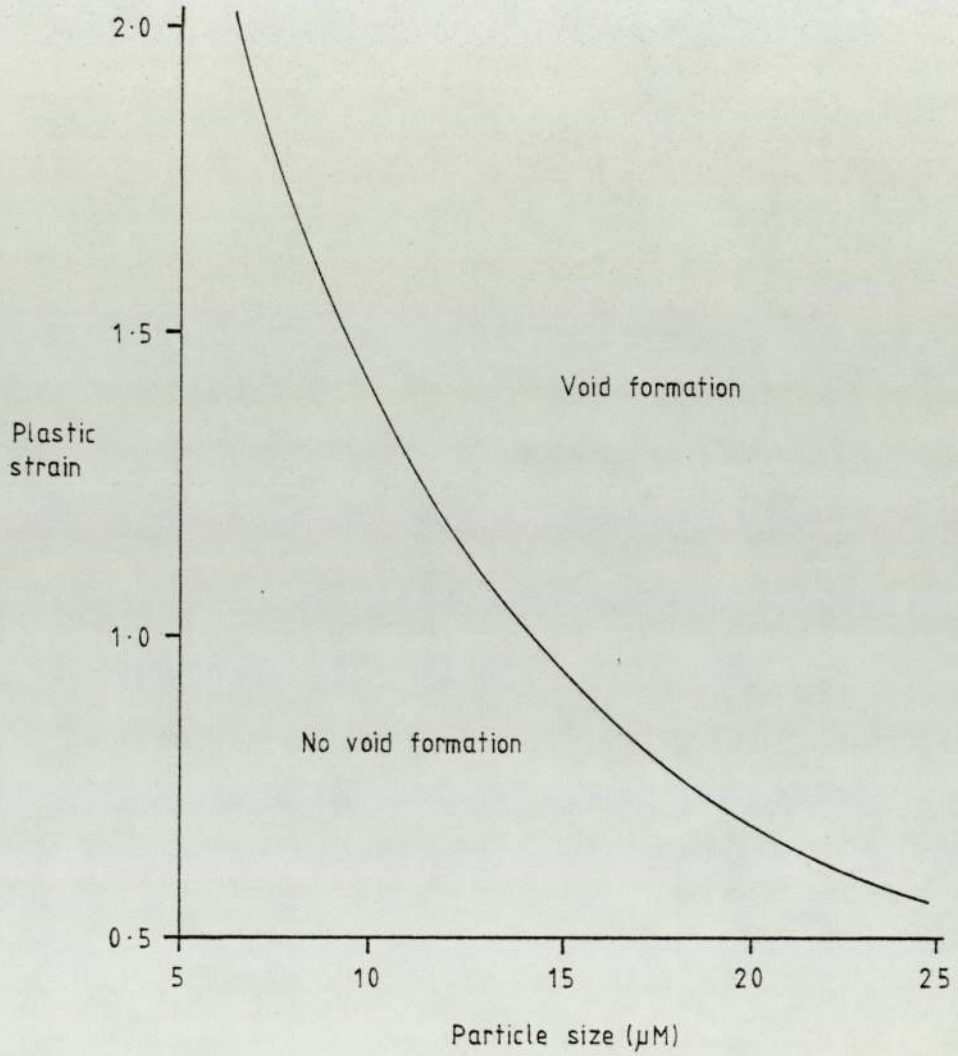

Fig. 9

Void Nucleation (Tanaka)

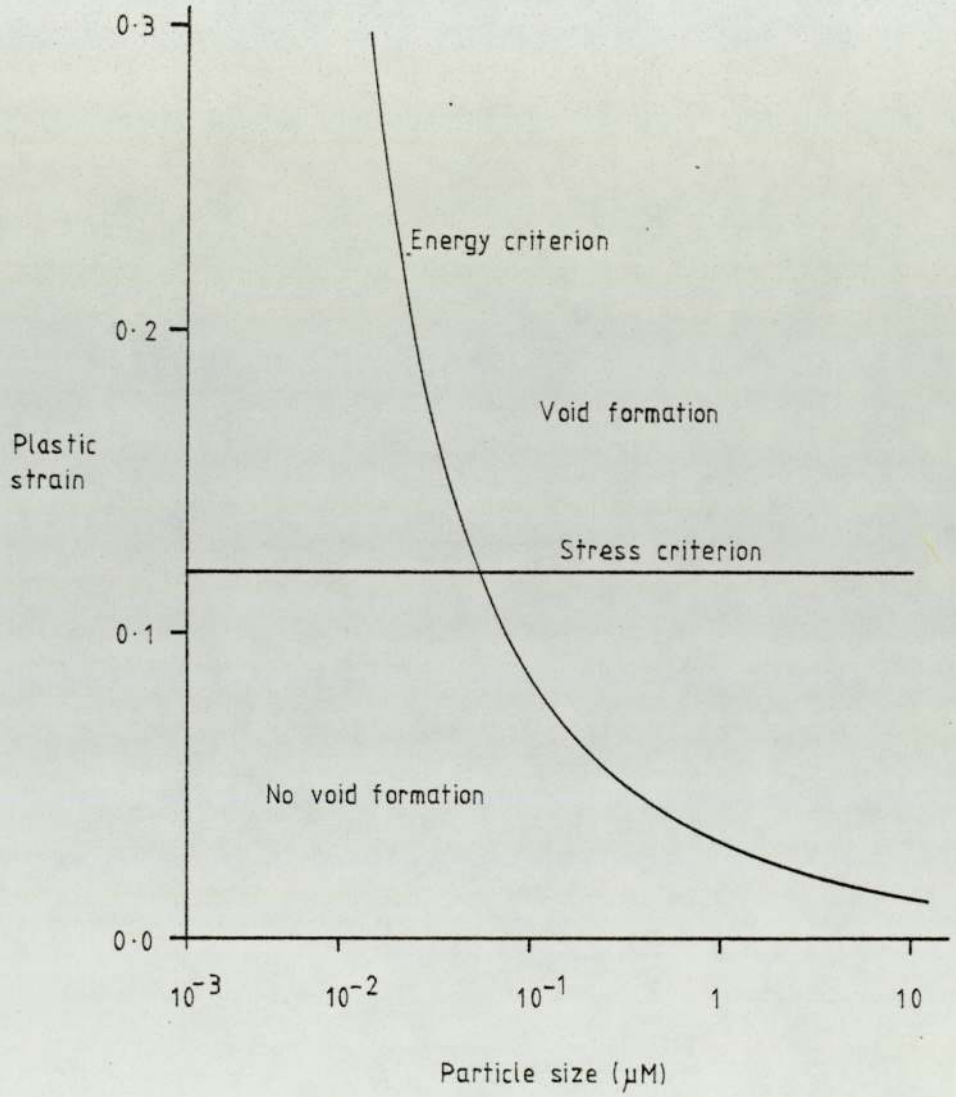

Fig. 10

Void Growth Rates

(after Rice and Tracy)

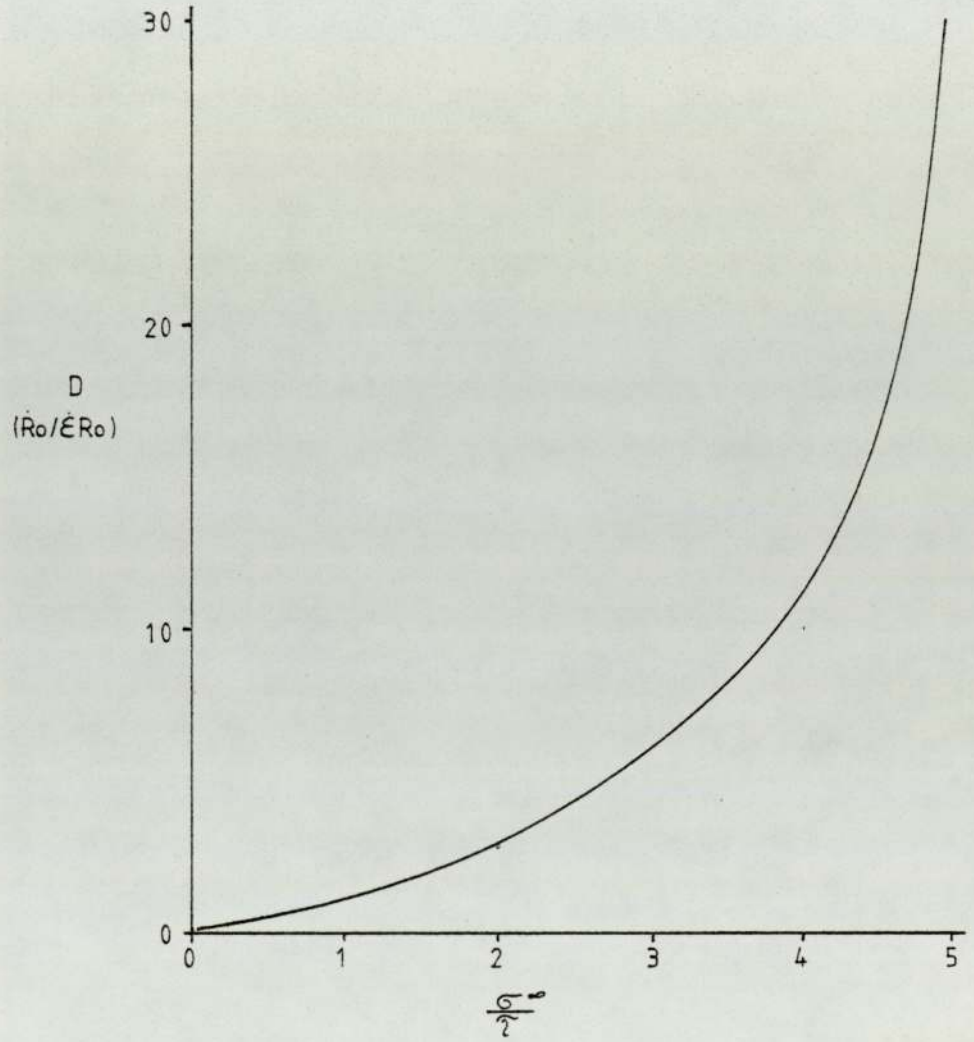

fig 9

Fig. 11

Ductility predictions from void growth theories

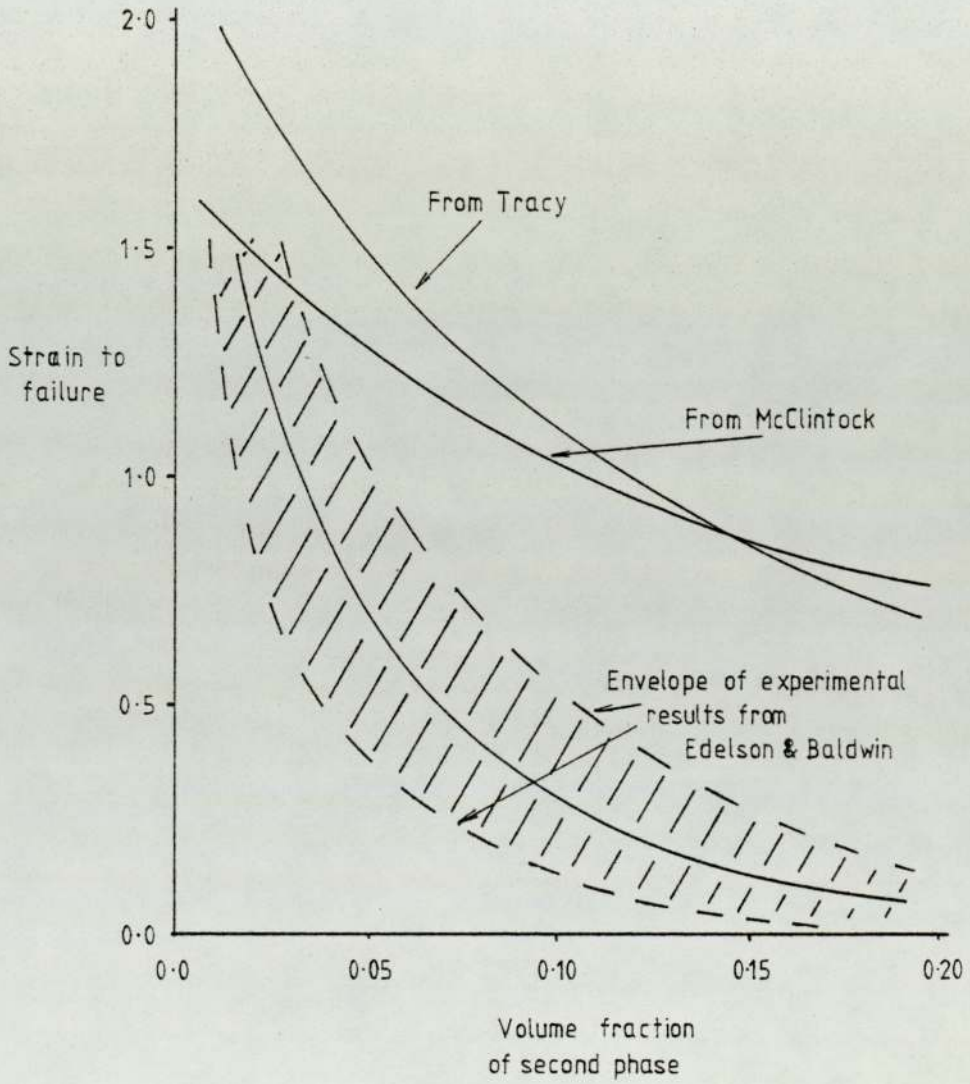

fig (10)

Fig. 12

Hole–growth amplification near a void

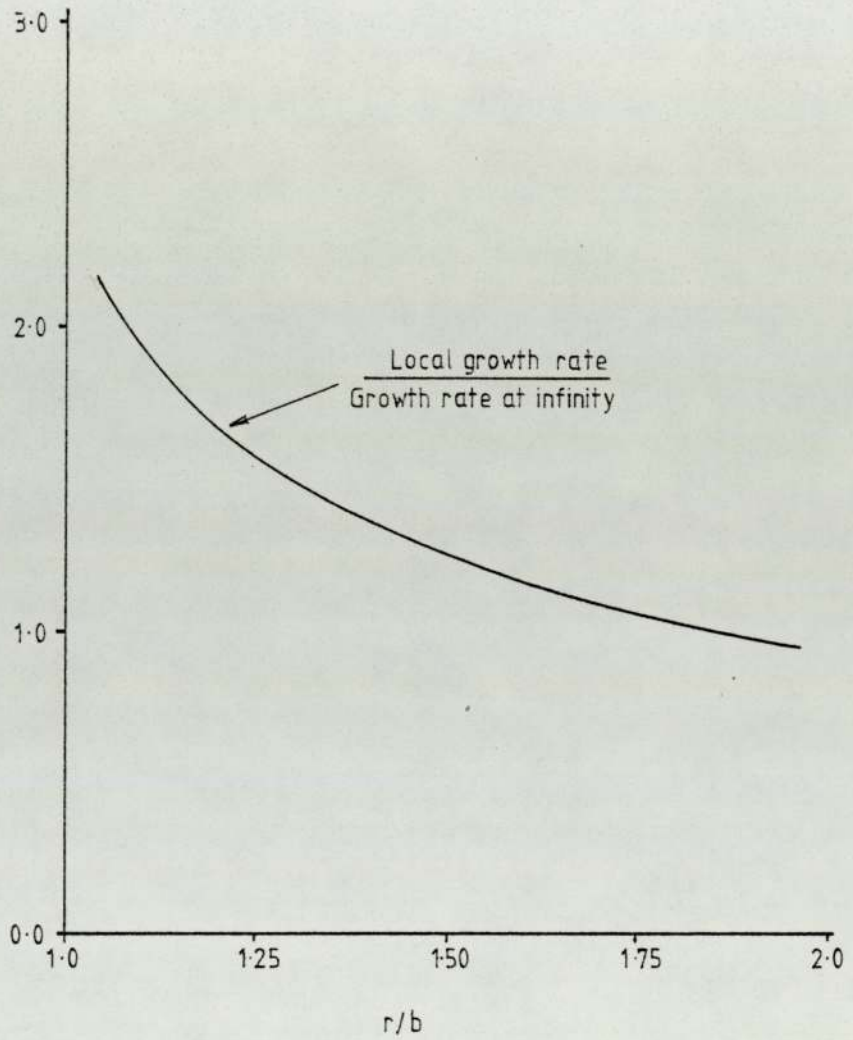

fig (1)

Fig. 13

Dilational Banding (Berg)

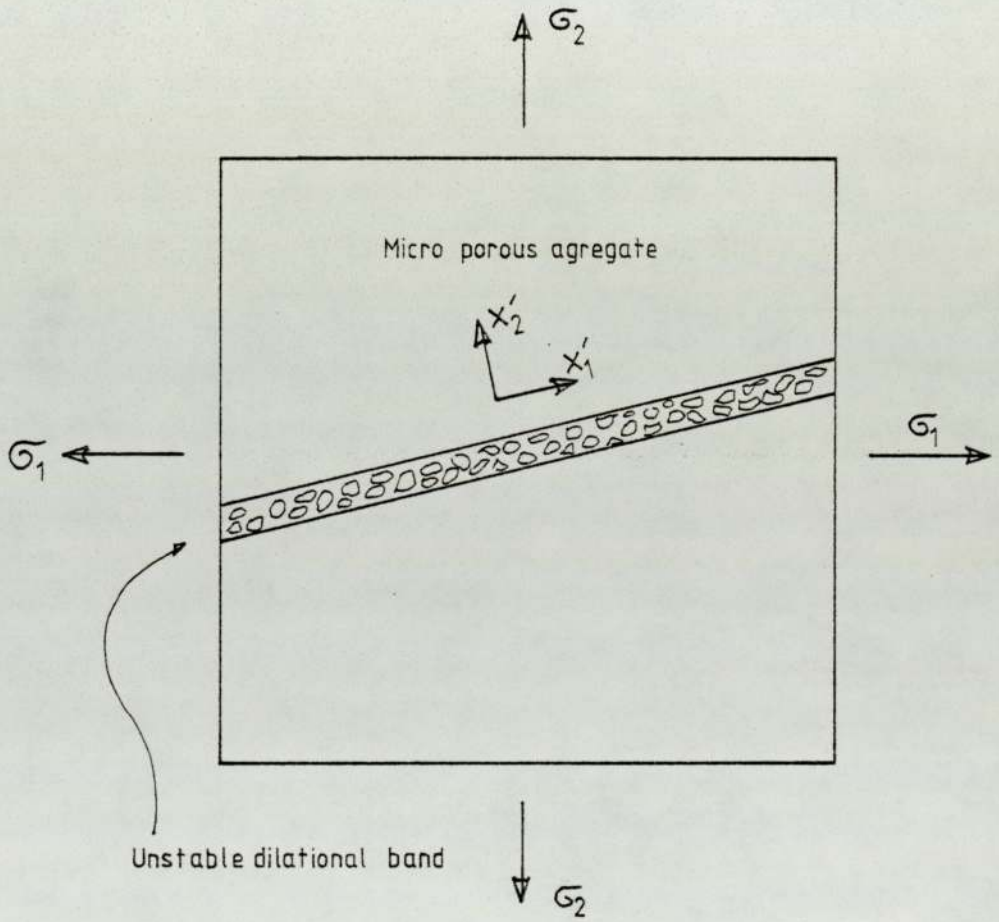

$\delta\varepsilon'_{11}$ in the X′ direction must vanish during localisation

fig 14

Fig. 14

Capping of the yield locus

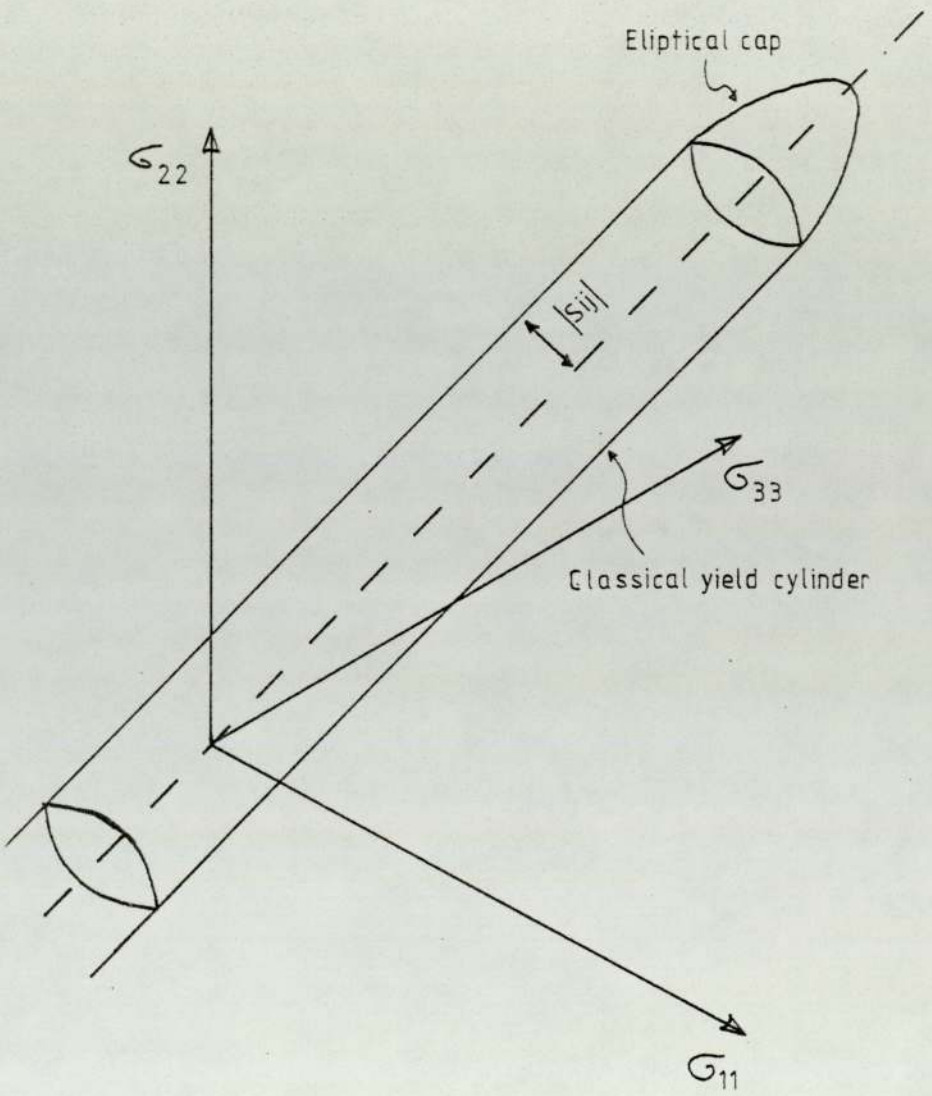

Fig (15)

Fig 15

Thomasons square array

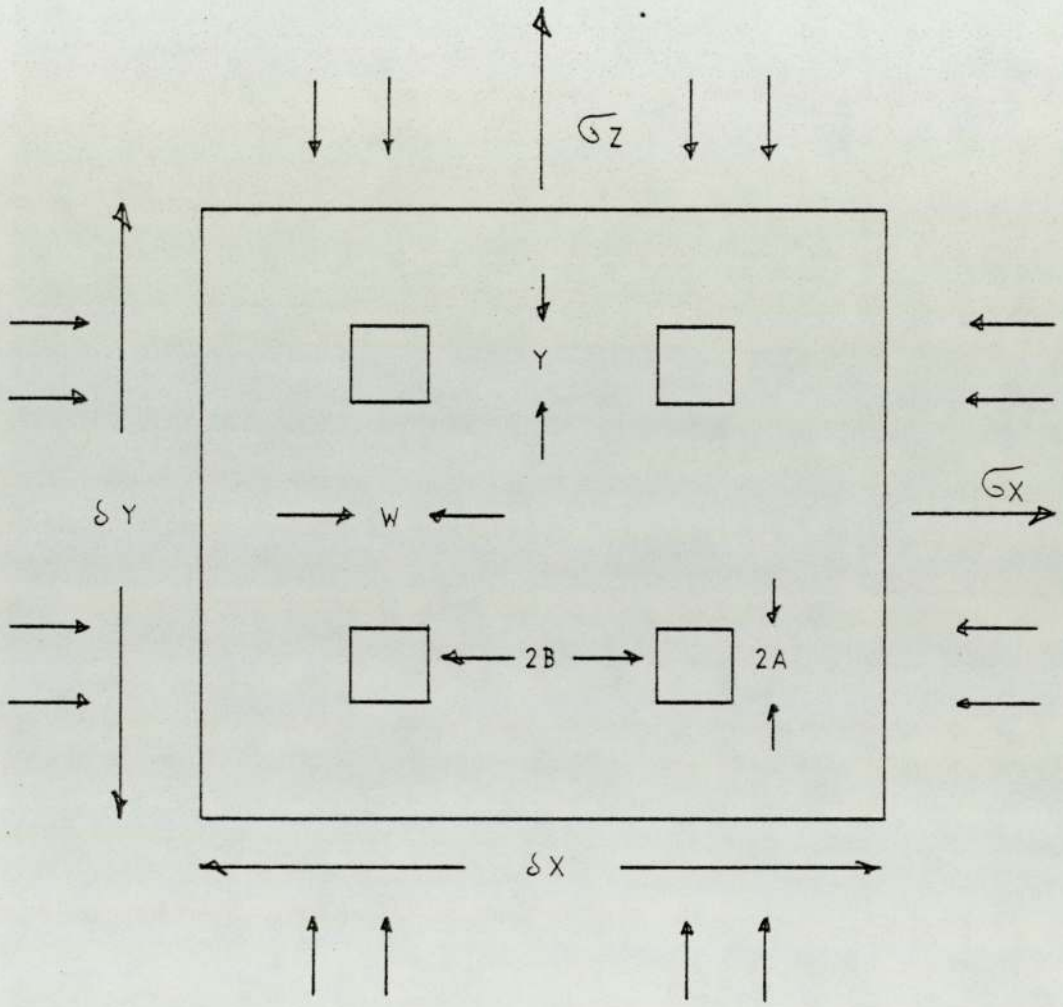

fig 16

Fig. 16

Stress to cause internal necking

(Thomasons square lattice)

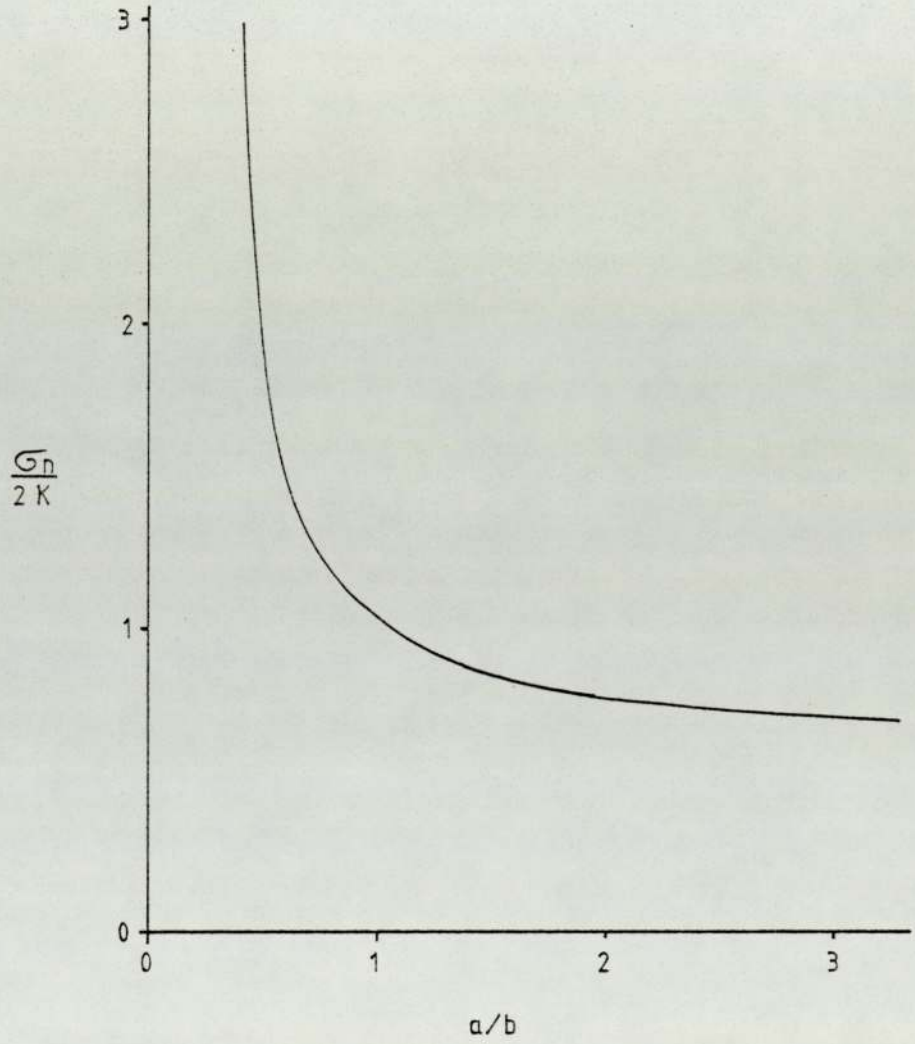

fig 17

Fig. 17

Strain to instability (Thomason)

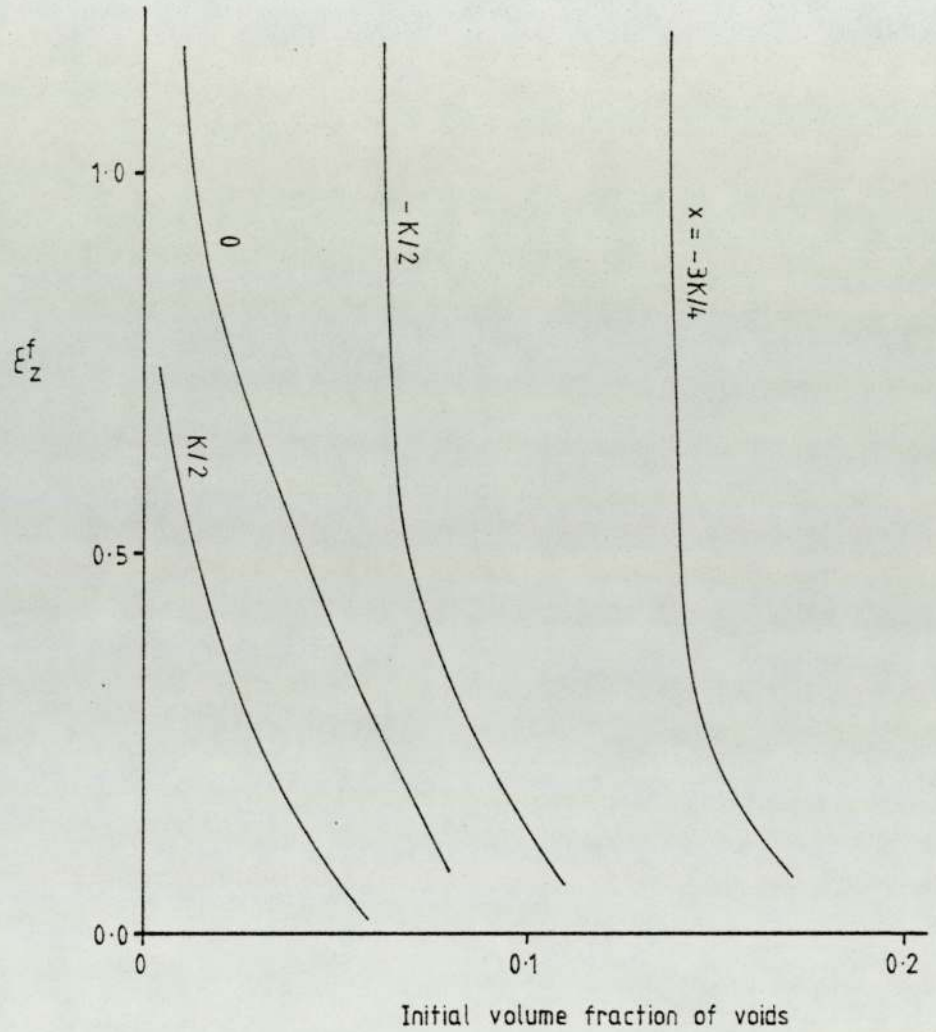

fig 18

Fig. 18

Hancocks void

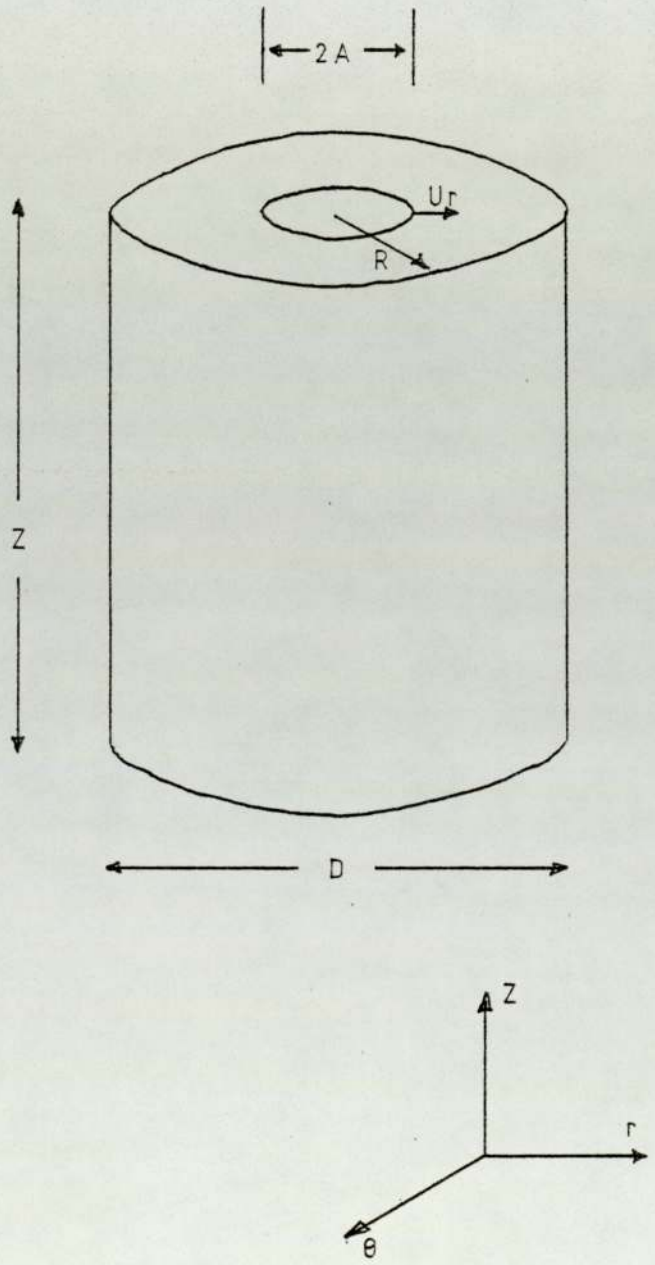

Fig 19

Fig. 19

Strain to radial load maxima

(Hancock)

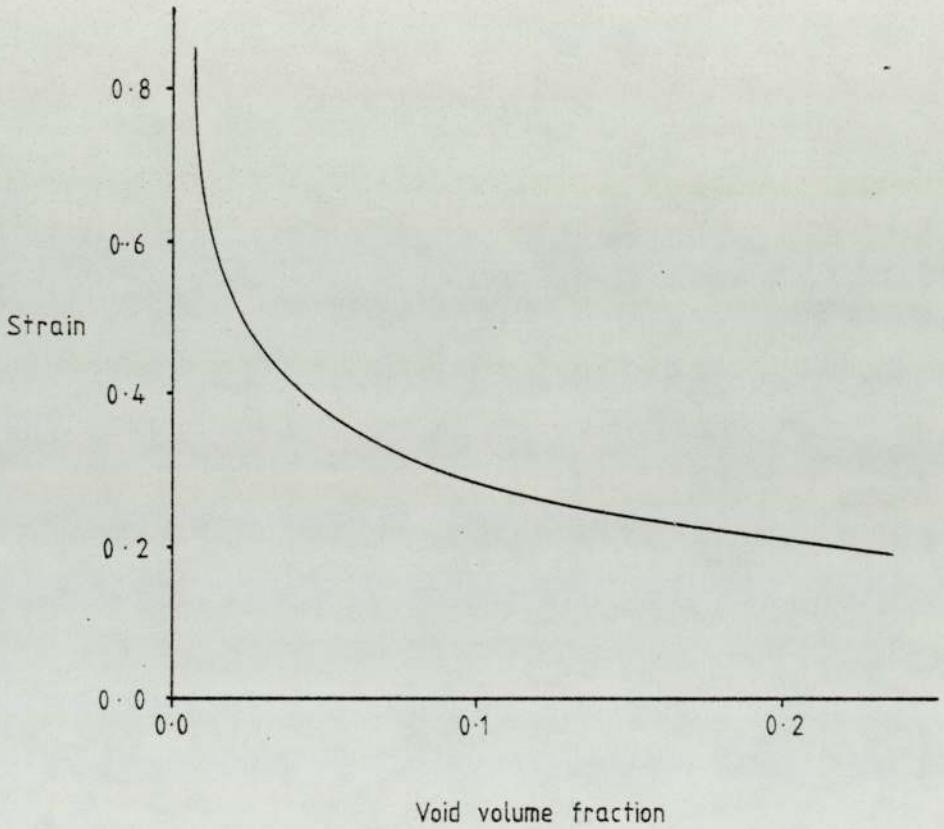

Fig 20

Fig. 20

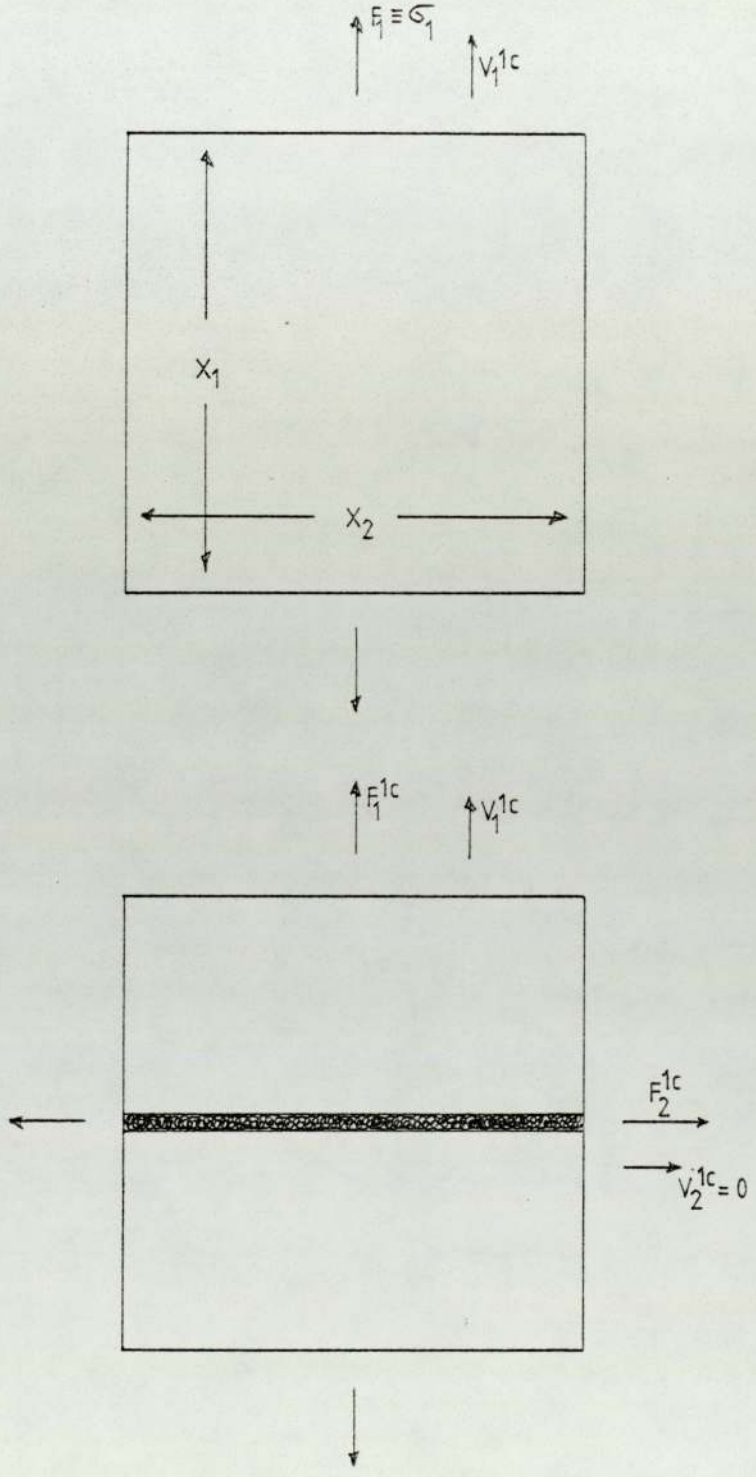

Fig. 21

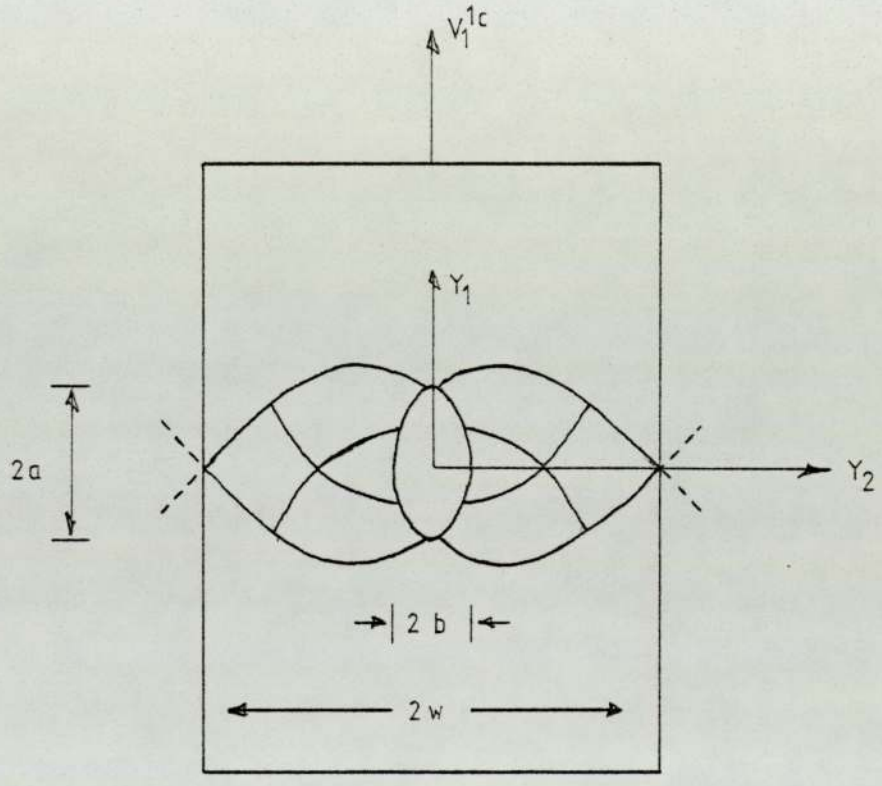

Fig. 2 2

Instability Tractions

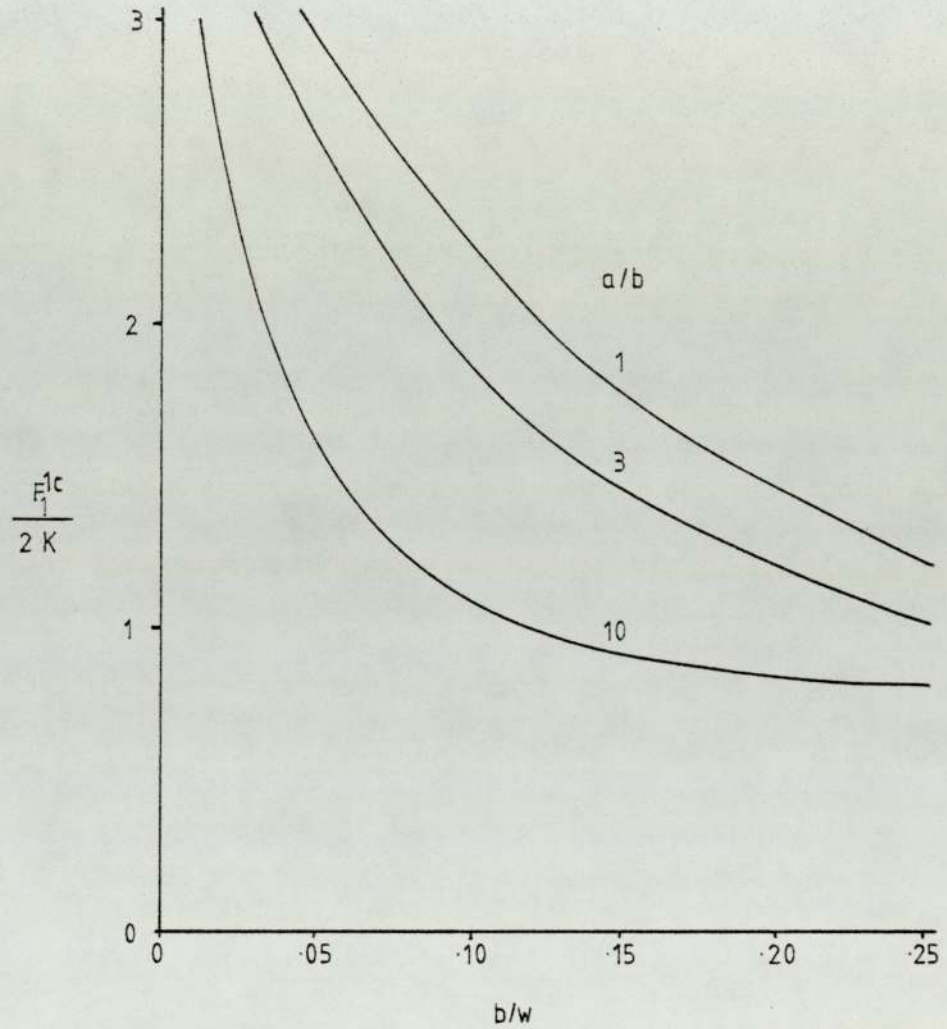

Fig. 23

Dilational yield surface cutting the yield cylinder

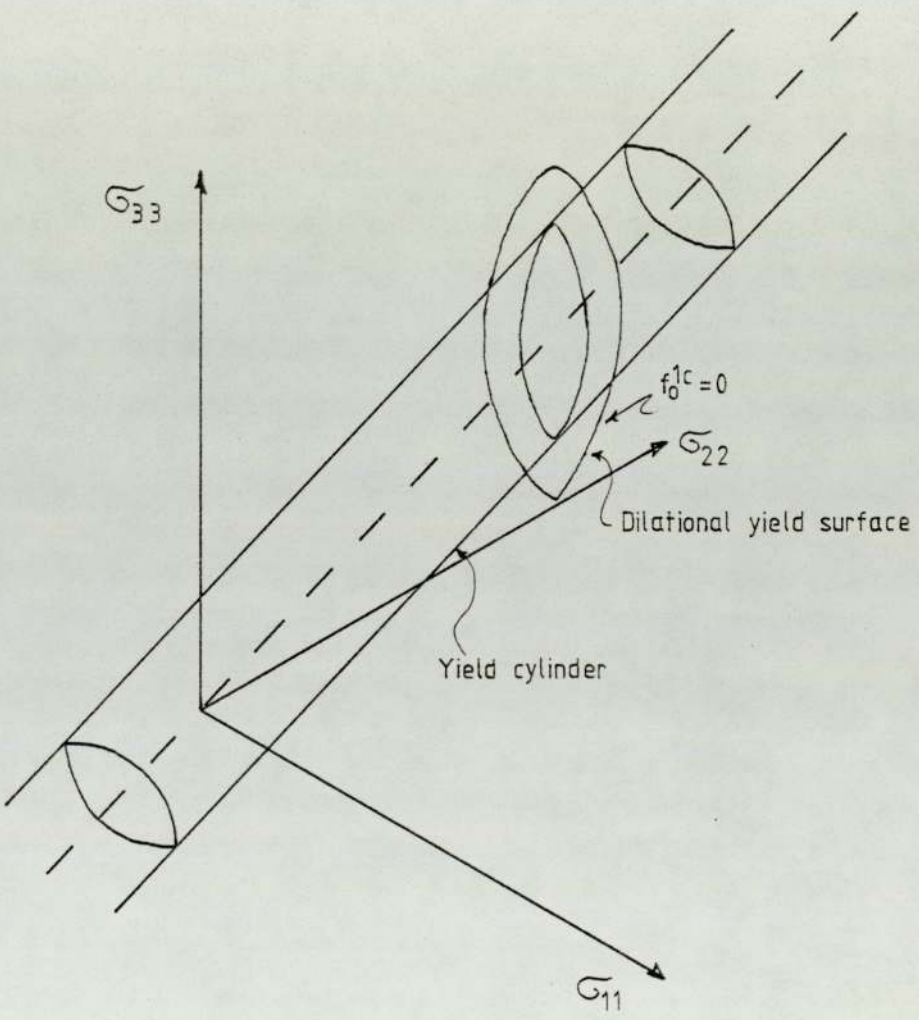

Fig. 24

Generalised coalesence

(after the observations of Roberts et al)

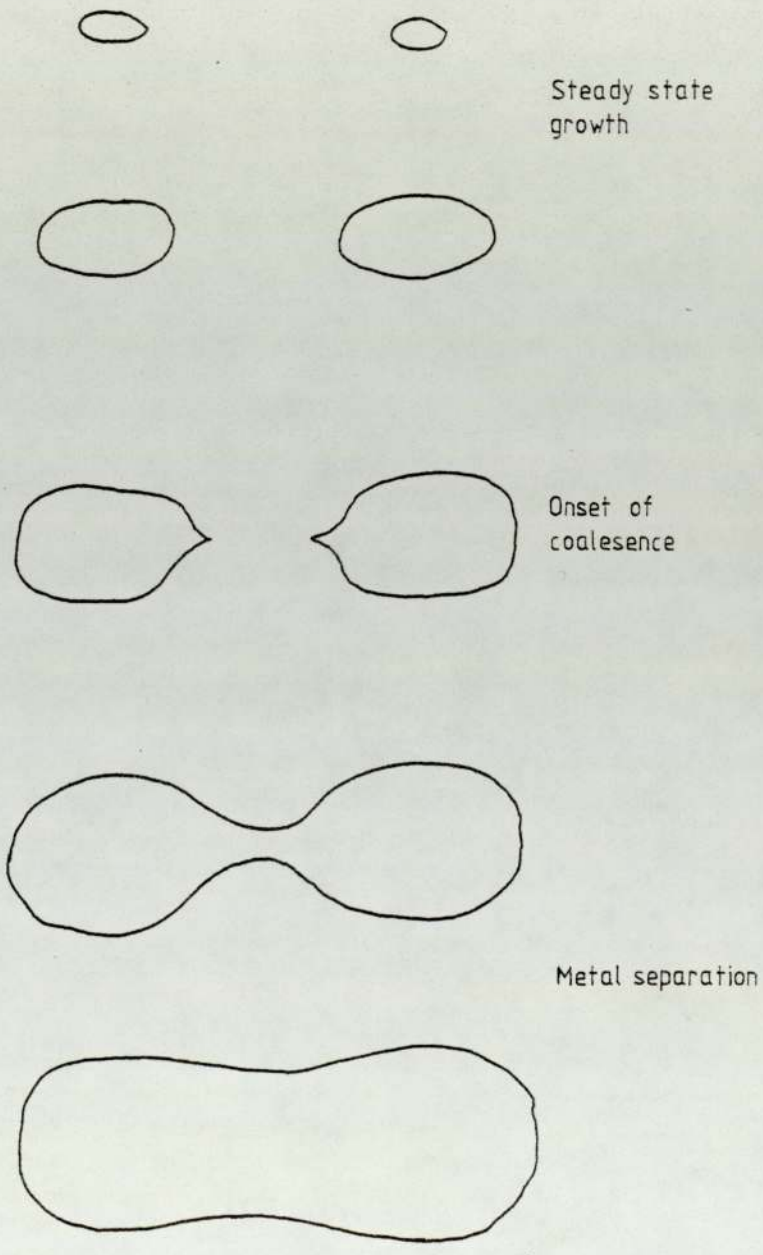

Fig 25

Effect of stress state on ductility

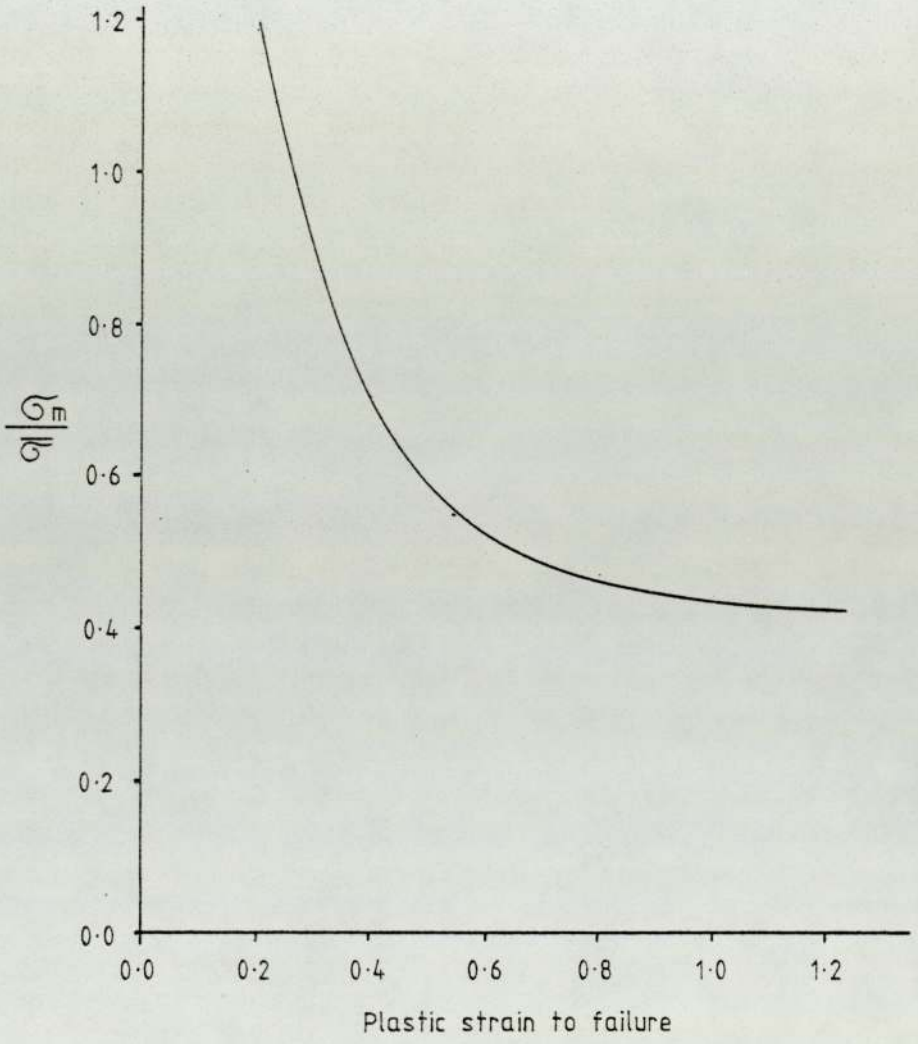

Fig. 26

Stress state beneath a key-hole notch

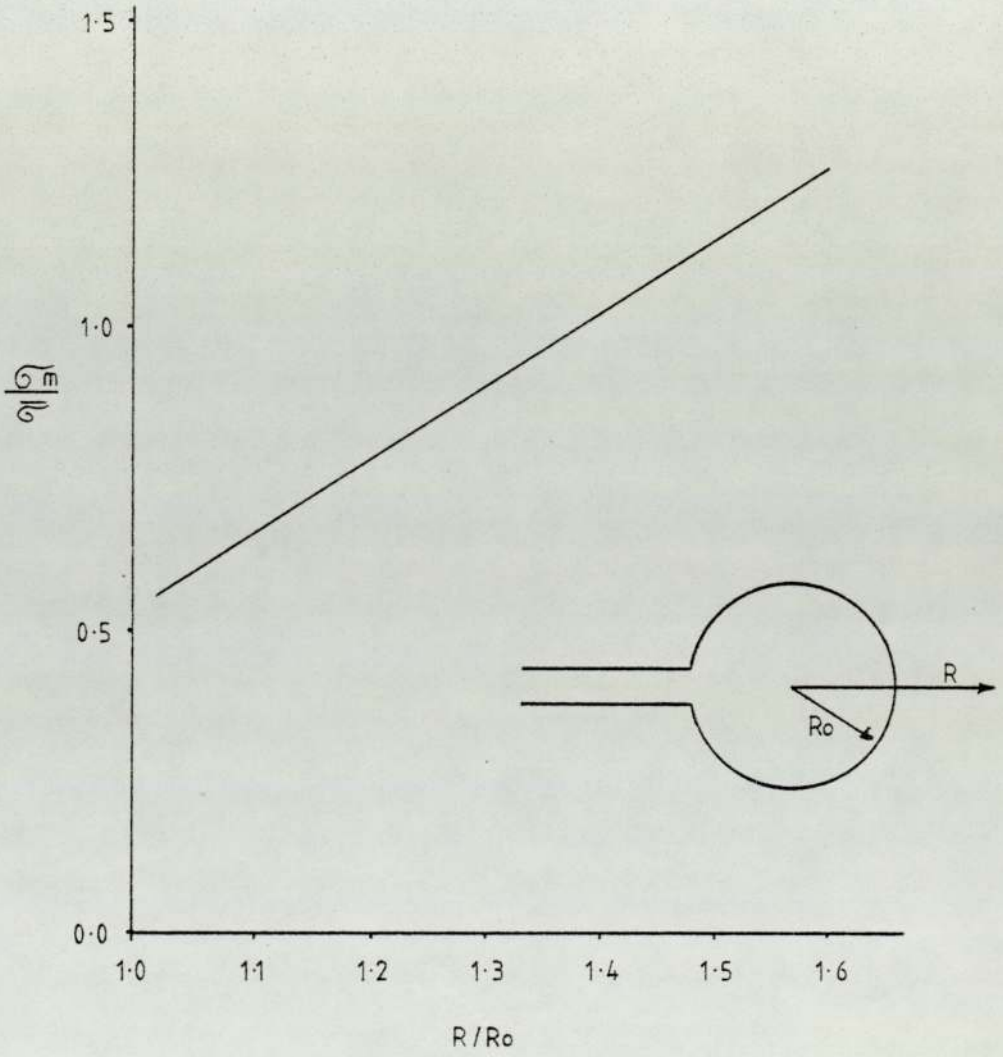

Fig. 27

Strain under a key-hole notch (slip line solution)

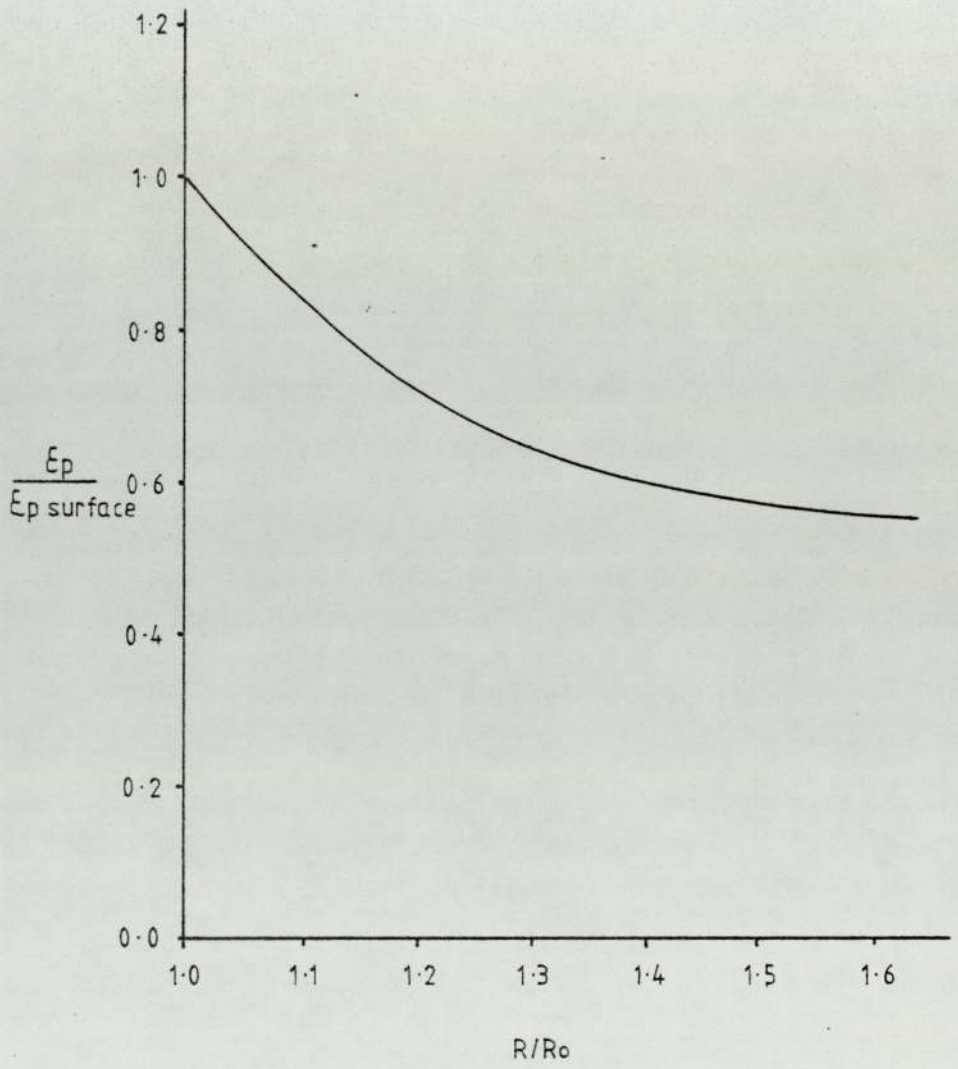

Fig. 28

C.O.D. Vs Surface strain

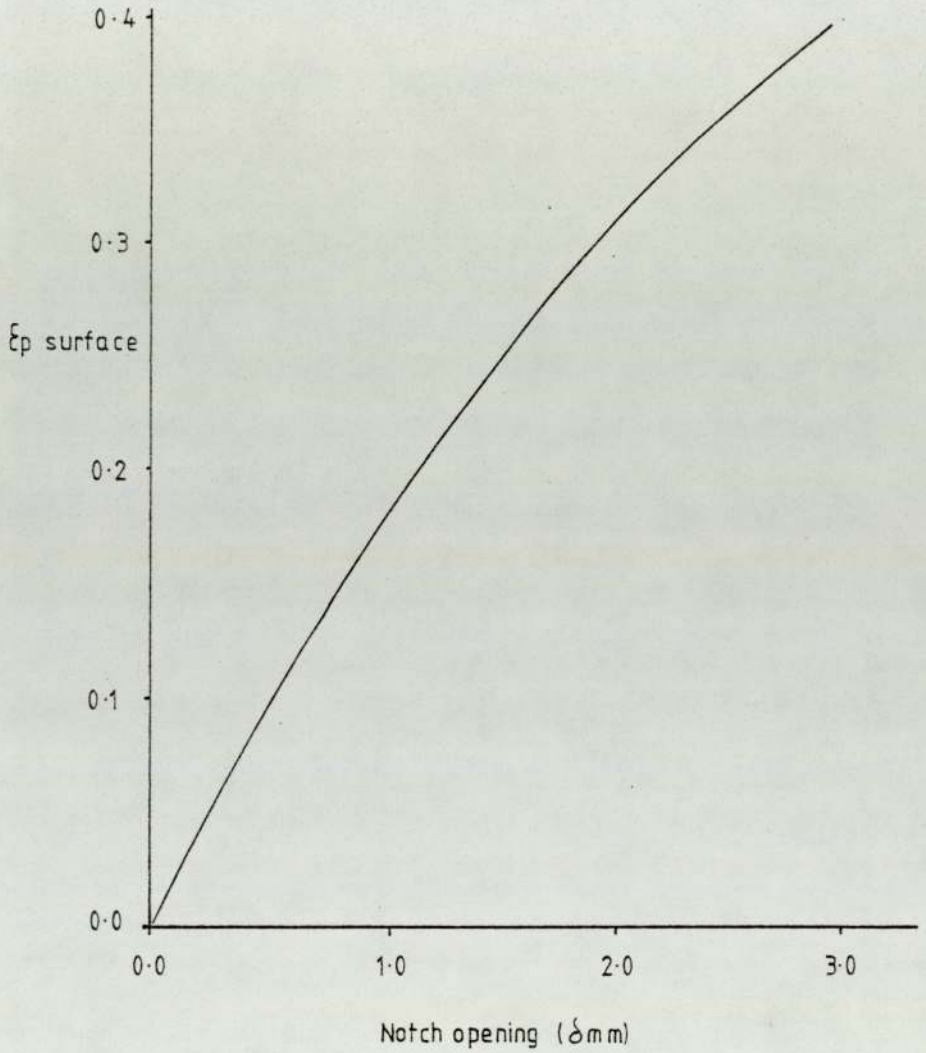

Fig. 29

Slip line field under a blunt crack

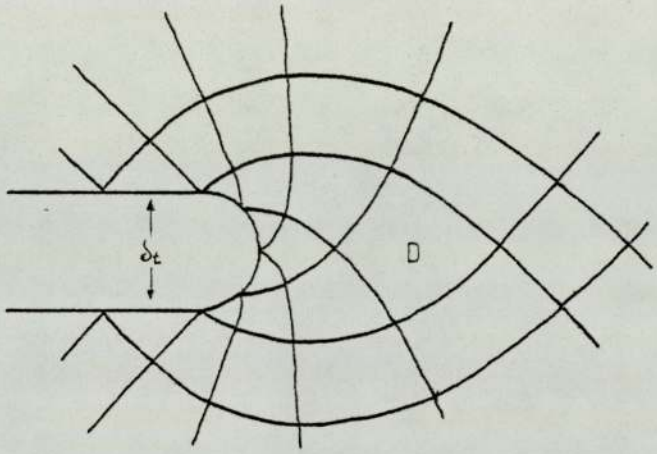

after Rice and Johnson

Fig. 30

C.O.D. Vs particle size and spacing

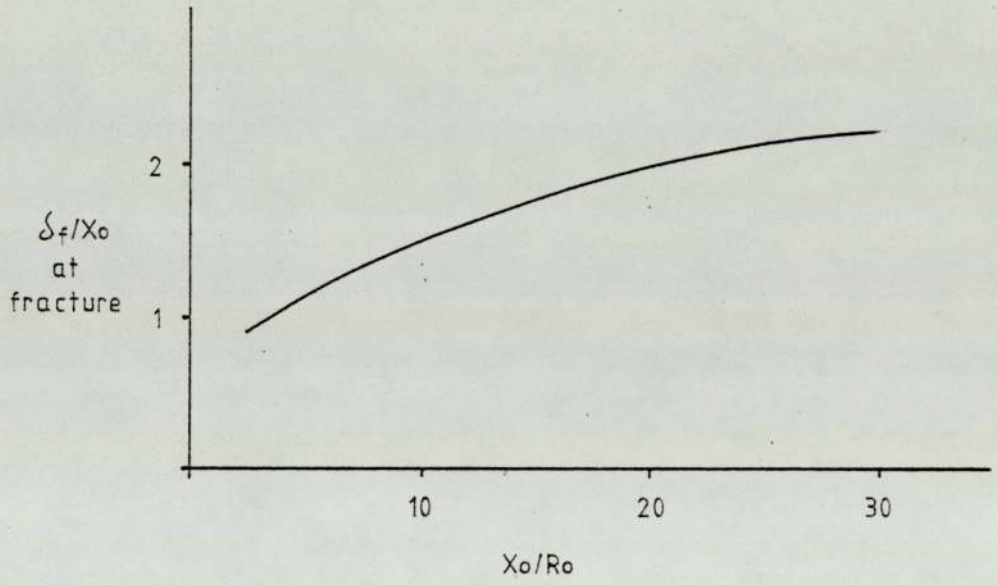

Fig. 31

Neuber's stress analysis

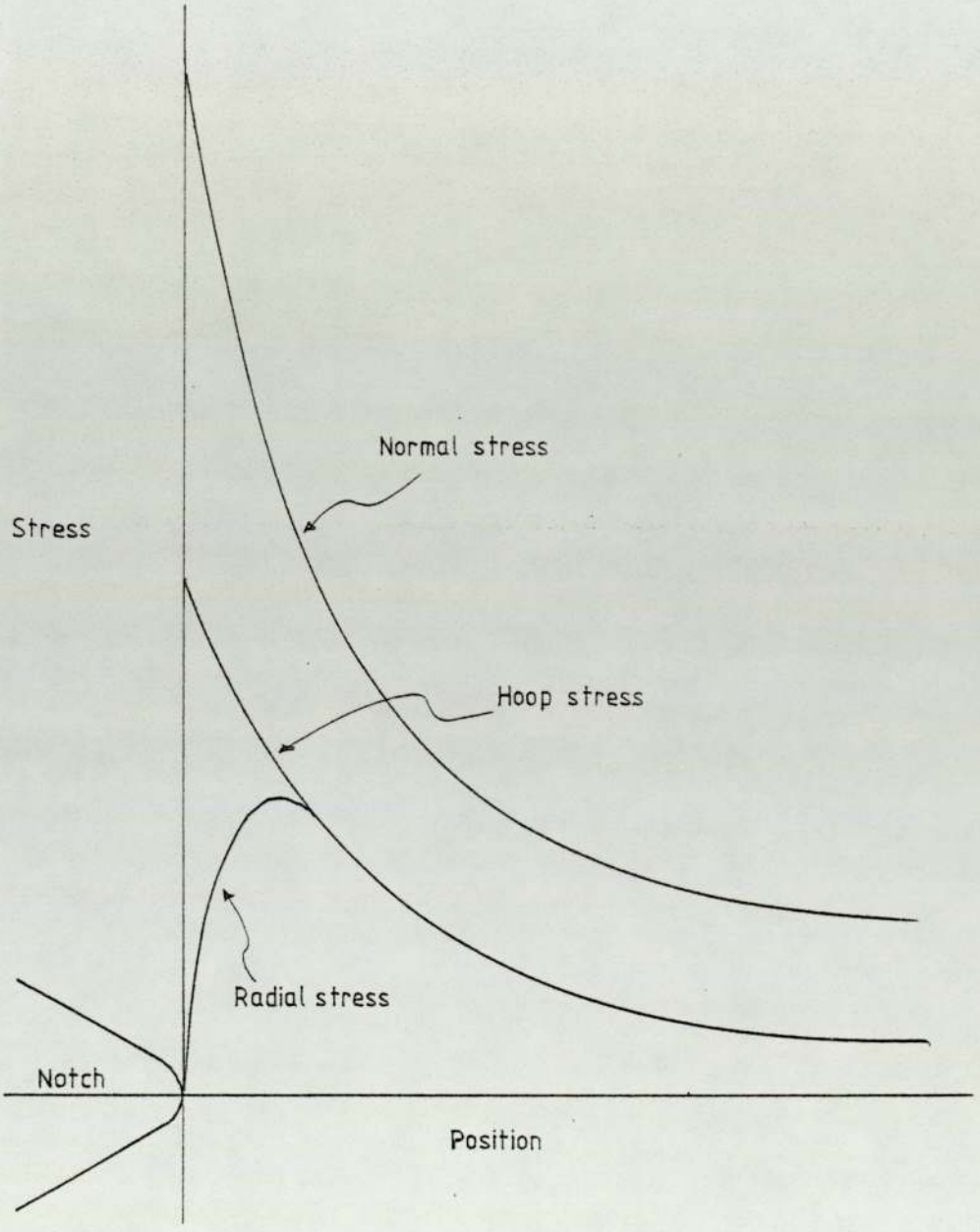

Fig. 32

Bridgman's stress analysis

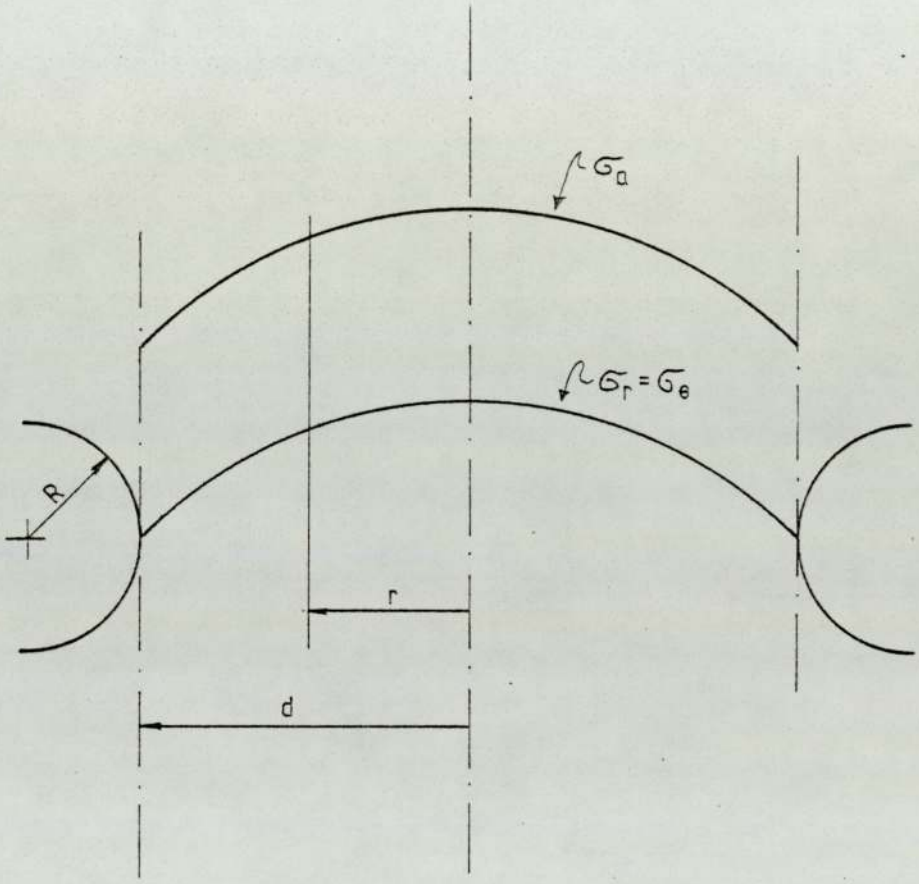

Fig. 33

Multi-notch Tensile Specimen

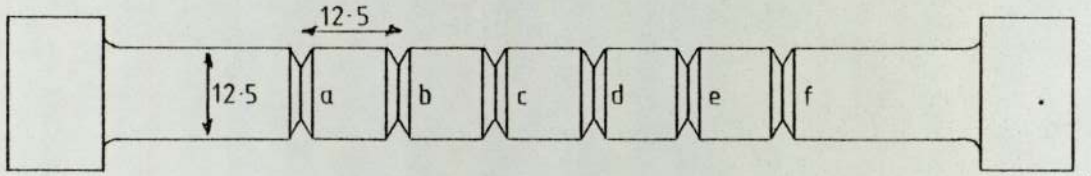

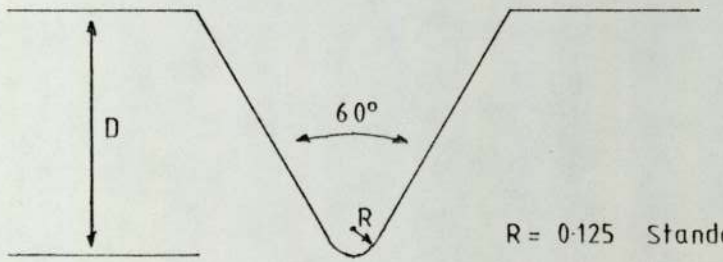

R = 0·125 Standard

R = 0·750 C '30'

Notch	Depth (D)
a	2·30
b	2·35
c	2·40
d	2·45
e	2·50
f	2·55

Fig. 34

Neck formation in parallel tensile specimens

1. $\varepsilon_p = 0{\cdot}18$

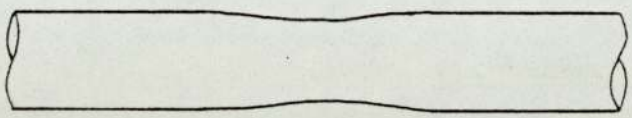

2. $\varepsilon_p = 0{\cdot}20$

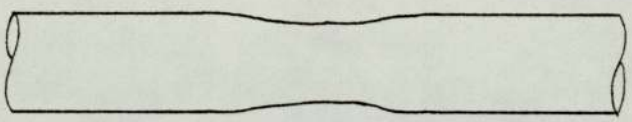

3. $\varepsilon_p = 0{\cdot}43$

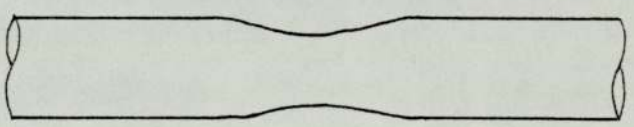

4. $\varepsilon_p = 0{\cdot}60$

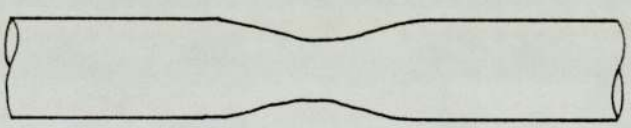

5. $\varepsilon_p = 0{\cdot}65$

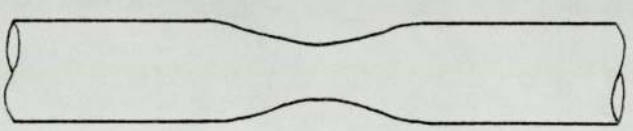

6. $\varepsilon_p = 0{\cdot}70$

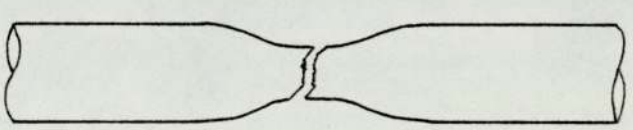

(fig 21)

Fig. 35

Stress Vs. Extension with Potential Drop

For single notch specimen HSO

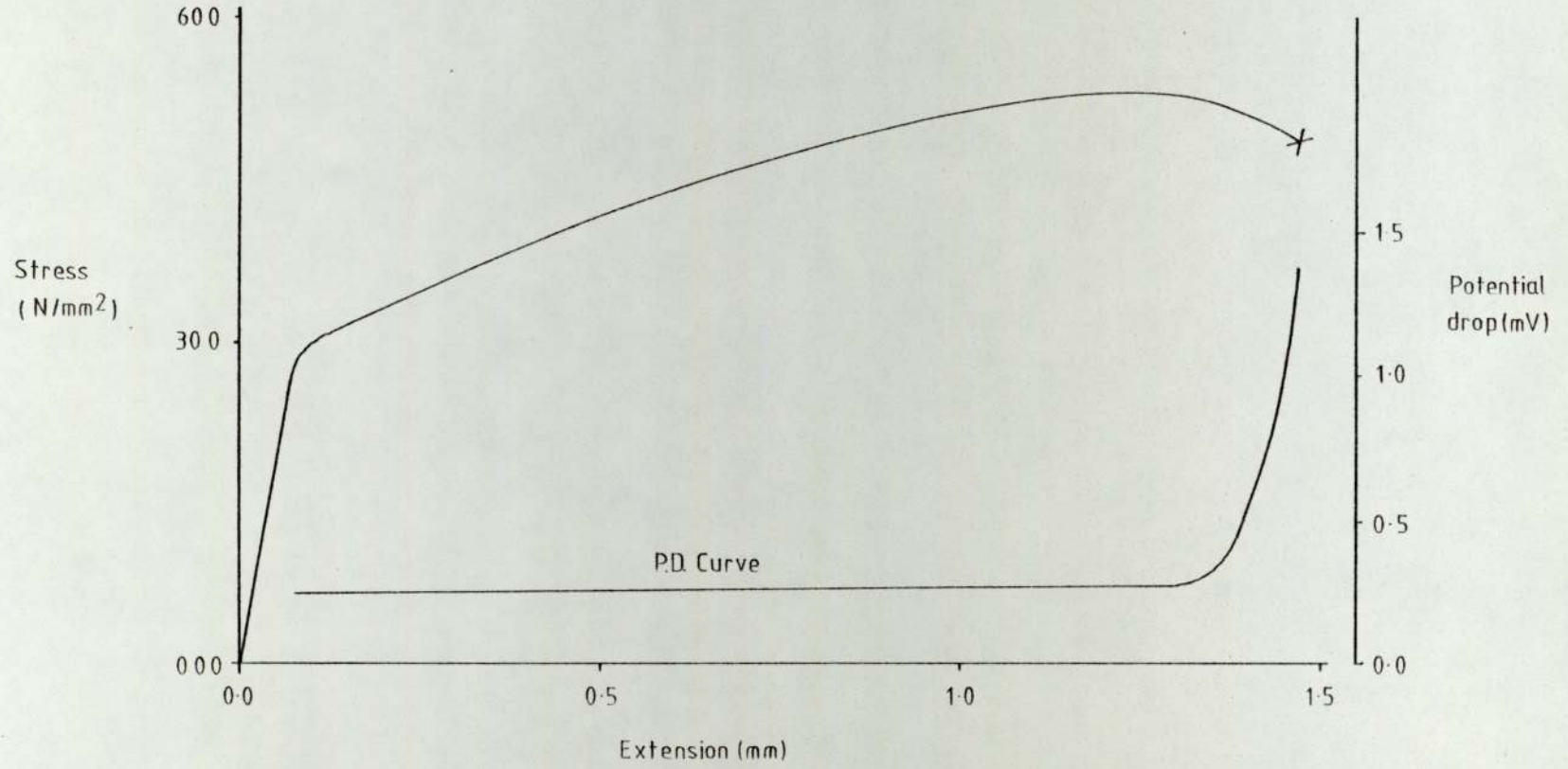

Fig. 36a

True Stress
Vs.
True Strain

Material – Mild Steel Bar Stock

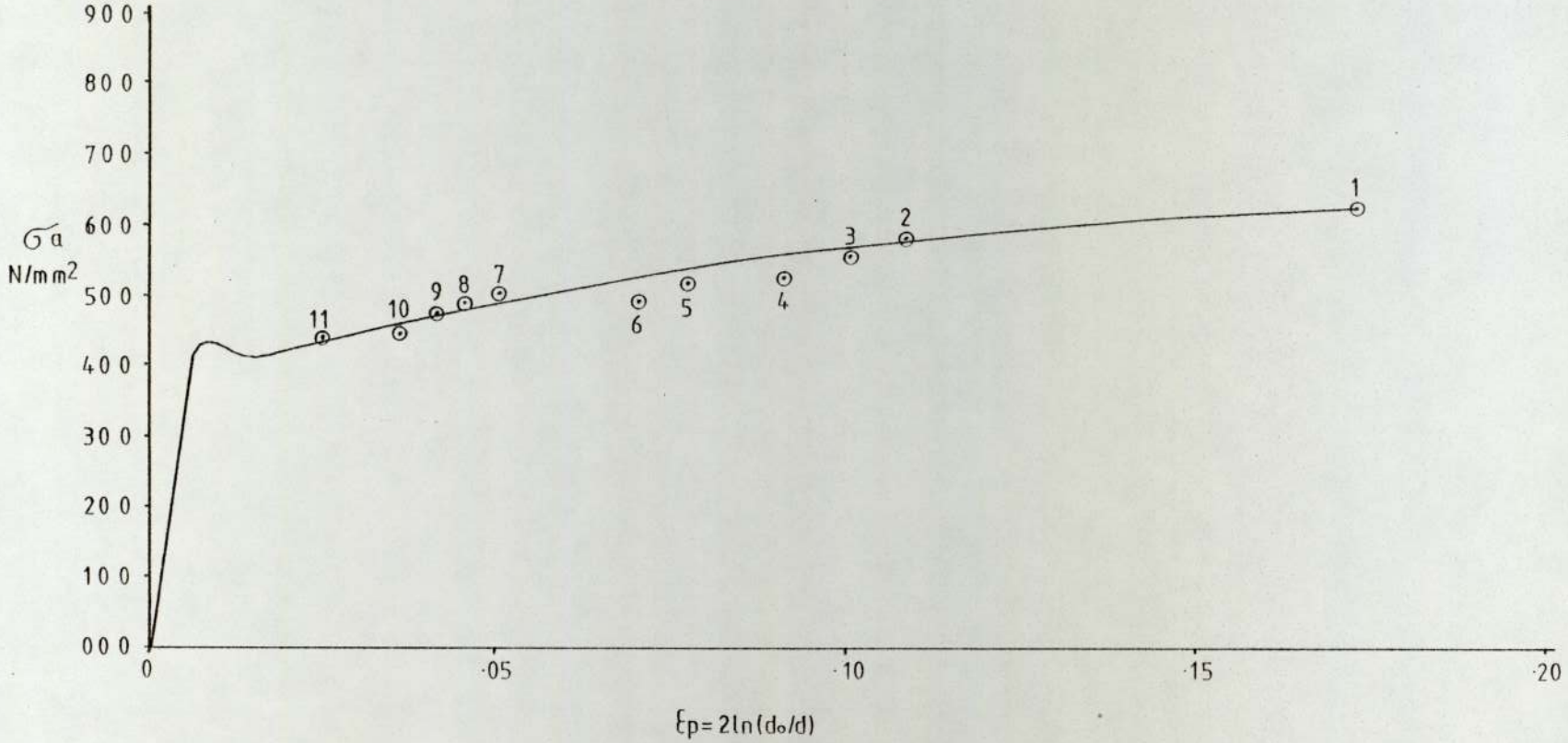

Fig. 36 b

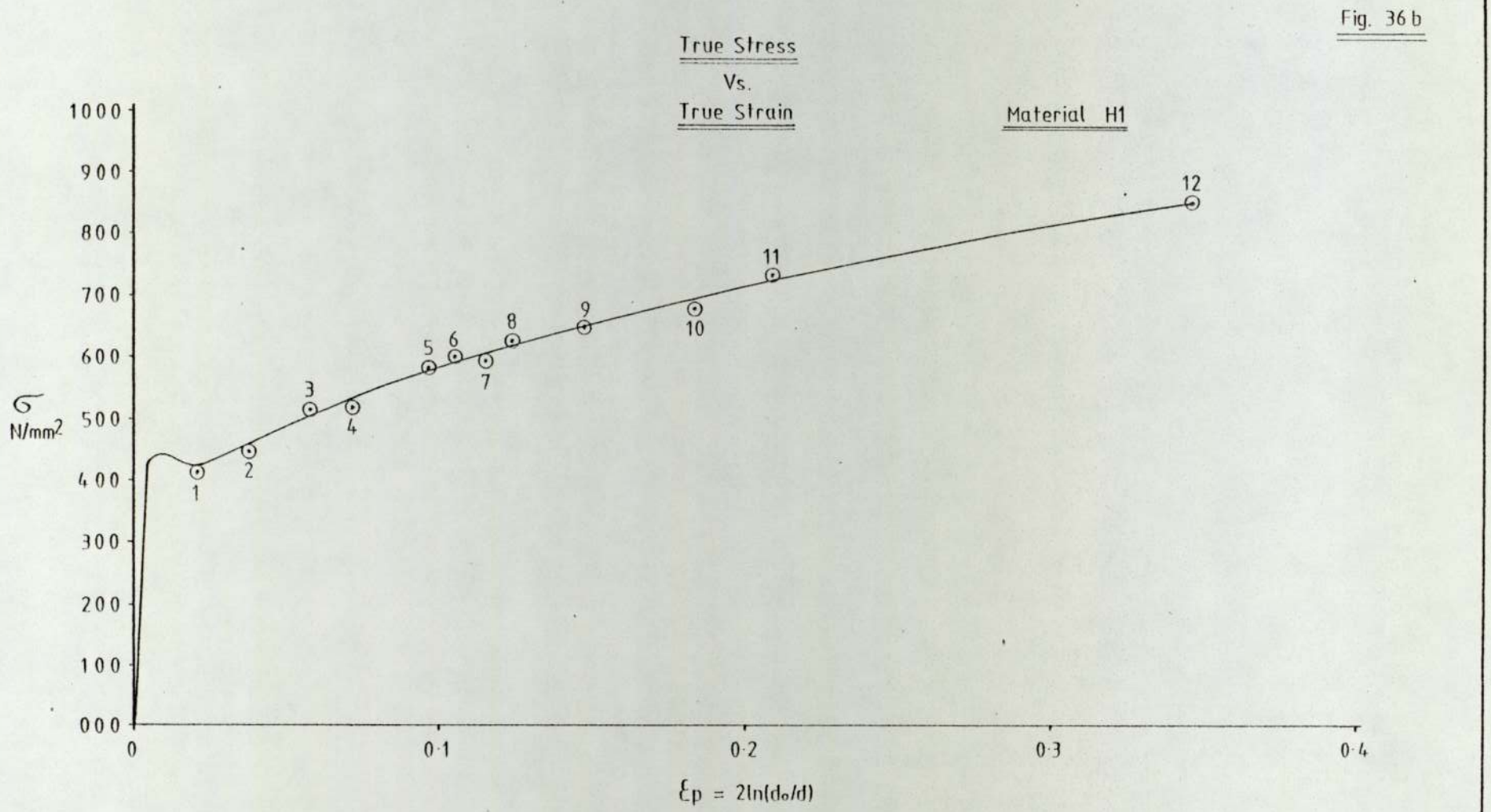
True Stress
Vs.
True Strain
Material H1
1000
900
800
700
600
500
400
300
200
100
000
σ
N/mm²
0
0·1
0·2
0·3
0·4
εp = 2ln(d₀/d)
1
2
3
4
5
6
7
8
9
10
11
12

Fig. 36 c

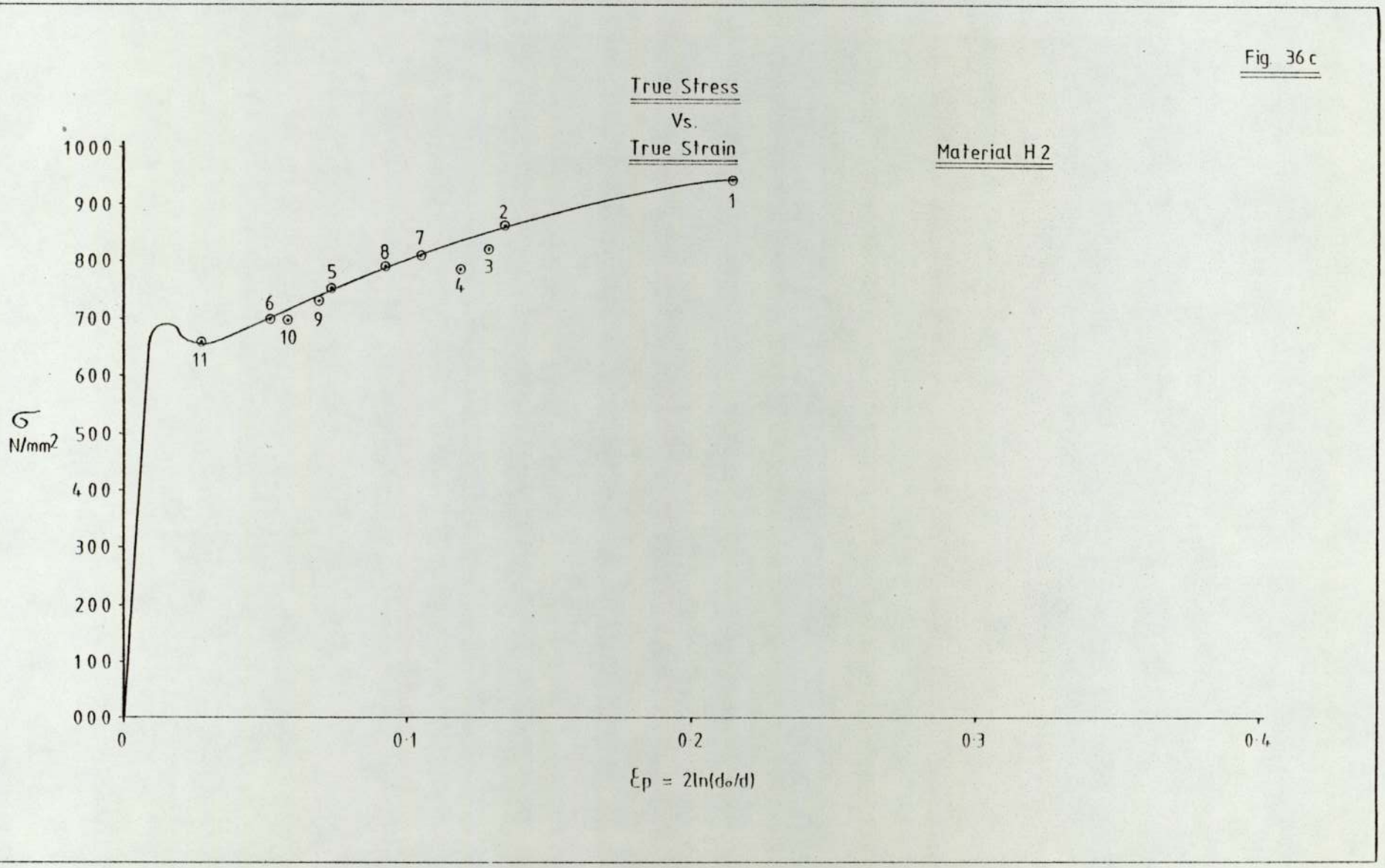
True Stress
Vs.
True Strain
Material H 2
1000
900
800
700
600
500
400
300
200
100
000
σ
N/mm²
0
0·1
0·2
0·3
0·4
εp = 2ln(d₀/d)
1
2
3
4
5
6
7
8
9
10
11

Fig. 36d

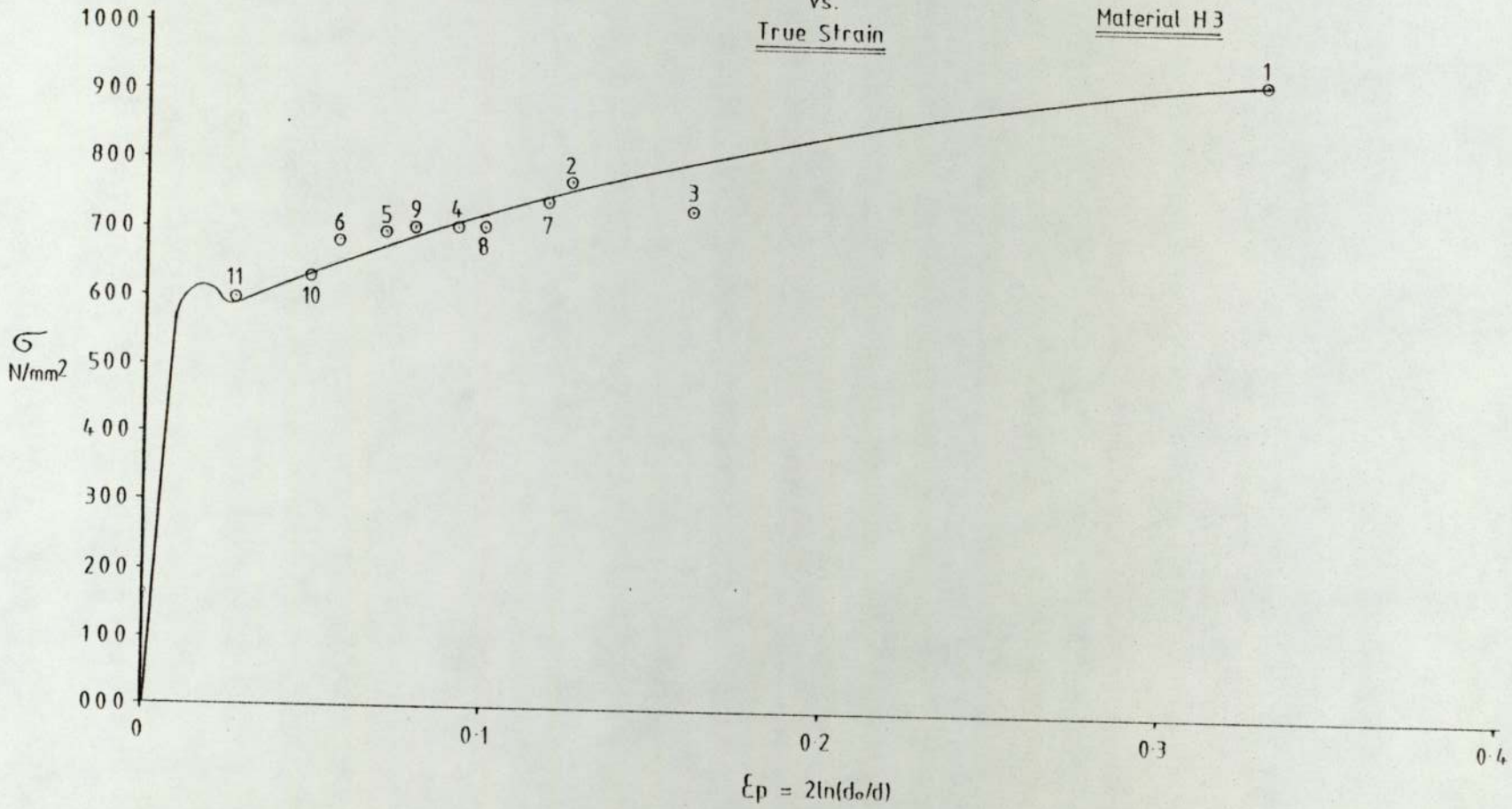
True Stress
Vs.
True Strain
Material H3
1000
900
800
700
600
500
400
300
200
100
000
σ
N/mm2
0
0·1
0·2
0·3
0·4
εp = 2ln(do/d)
1
2
3
4
5
6
7
8
9
10
11

Fig. 36 e

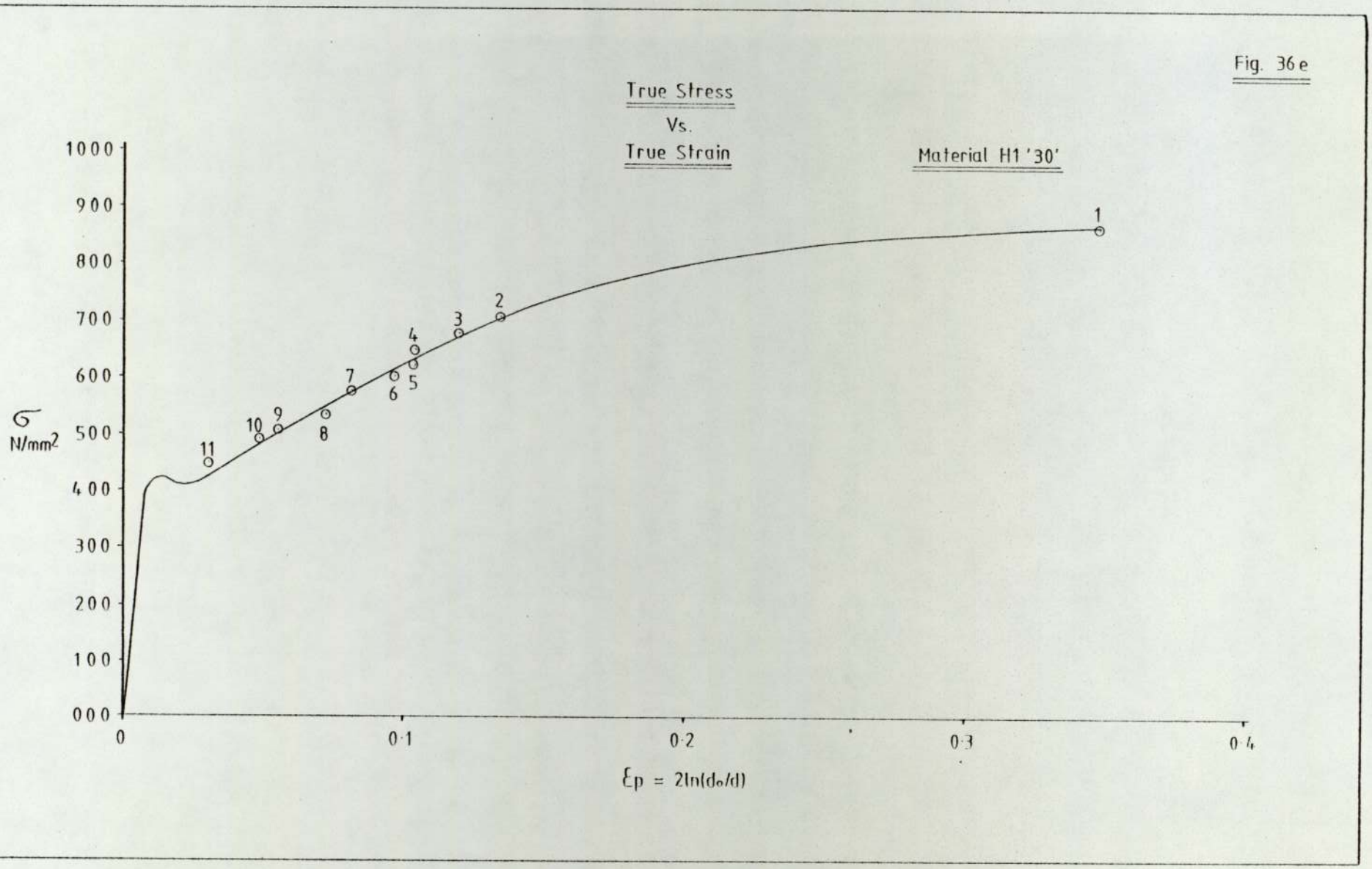
True Stress
Vs.
True Strain
Material H1 '30'
1000
900
800
700
600
500
400
300
200
100
000
σ
N/mm2
0
0·1
0·2
0·3
0·4
εp = 2ln(do/d)
1
2
3
4
5
6
7
8
9
10
11

Fig. 36 f

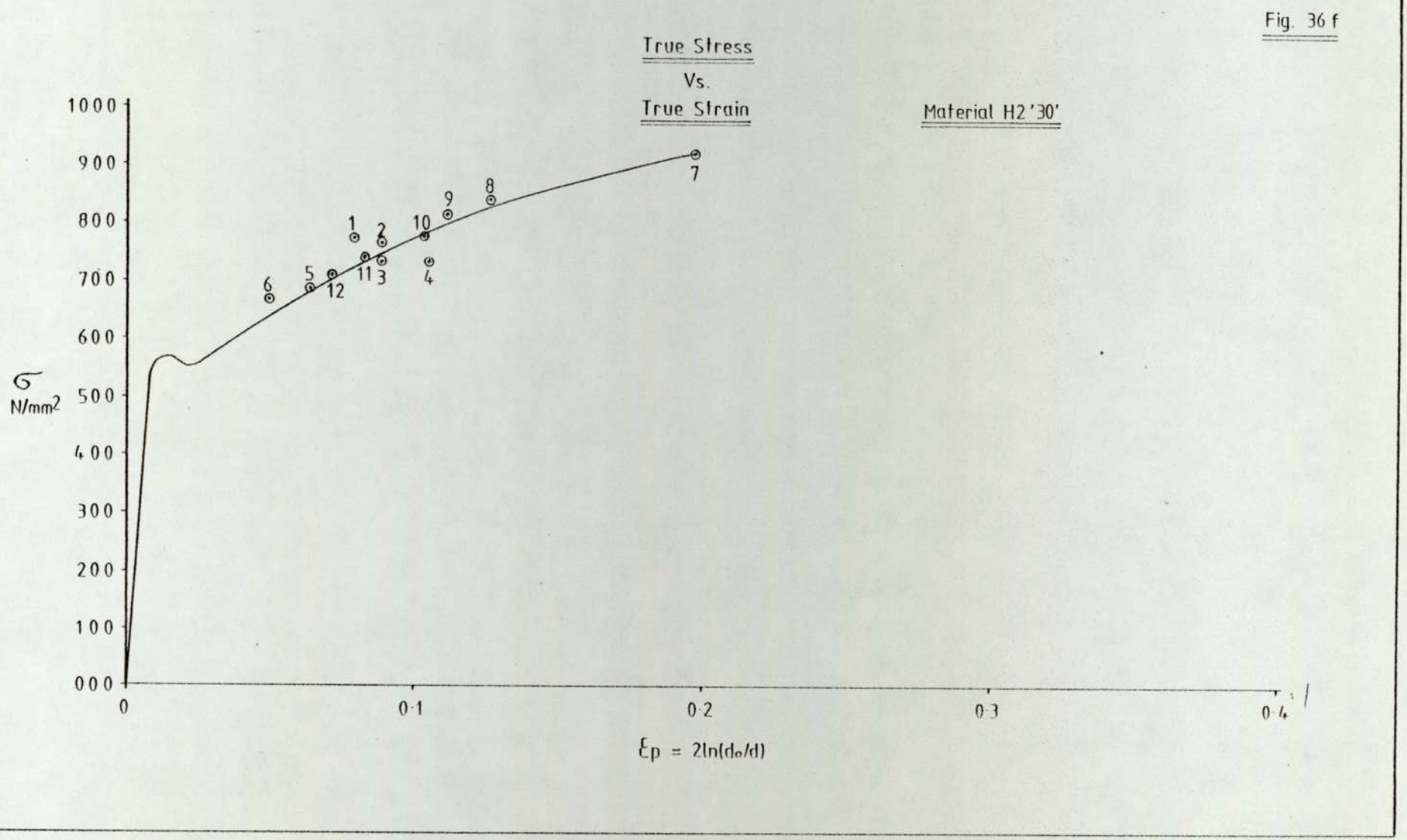
True Stress
Vs.
True Strain
Material H2 '30'
1000
900
800
700
600
500
400
300
200
100
000
σ
N/mm²
0
0·1
0·2
0·3
0·4
εp = 2ln(d₀/d)
1
2
3
4
5
6
7
8
9
10
11
12

Fig. 36g

True Stress
Vs.
True Strain

Material H3 '30'

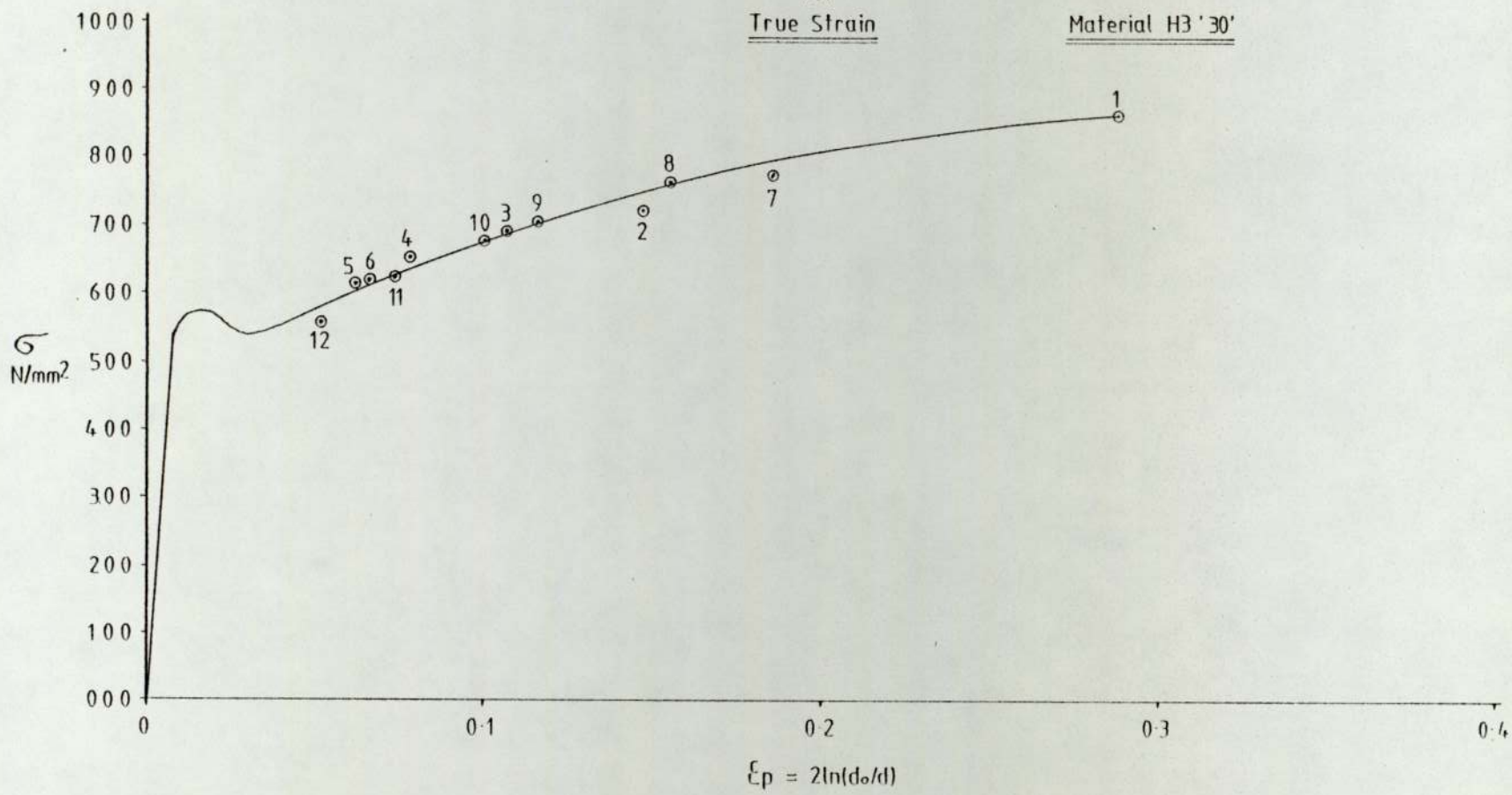

Fig. 37

Relationship between beam angle (θ)
and actual area under examination

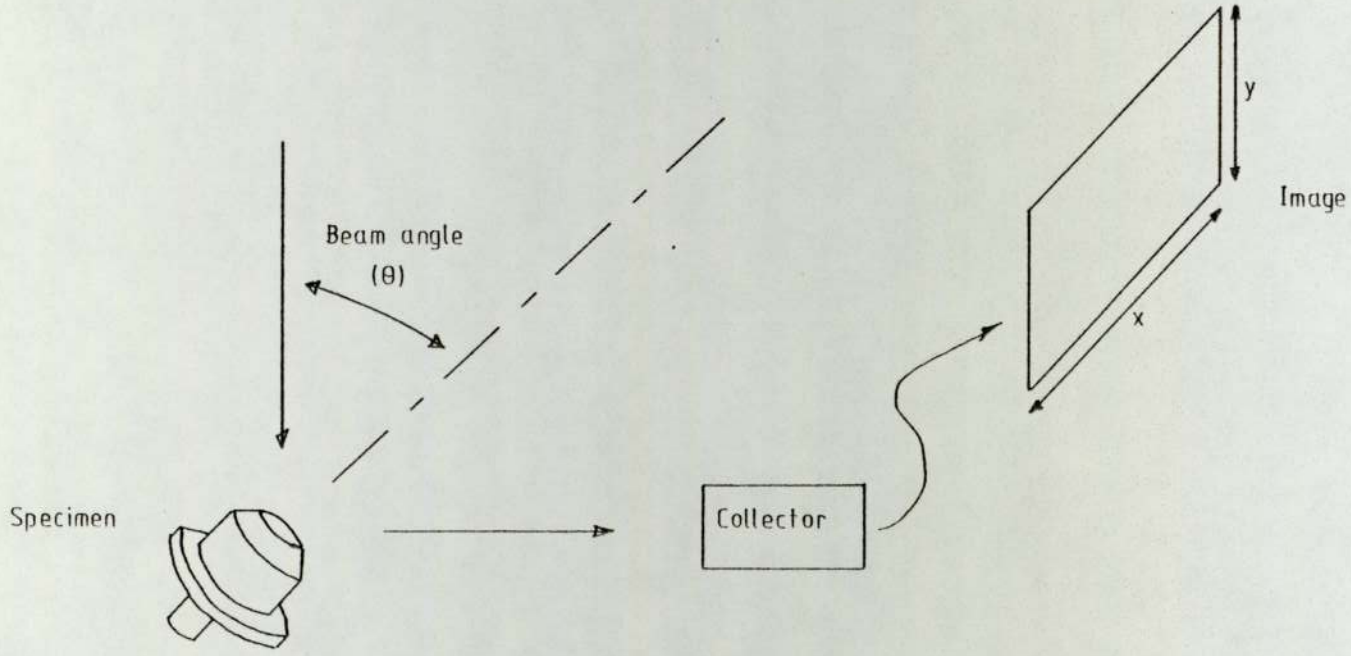

Fig. 38a

Average Nearest Neighbour Distance

Vs.

Applied Plastic Strain

Material – Mild Steel Bar Stock

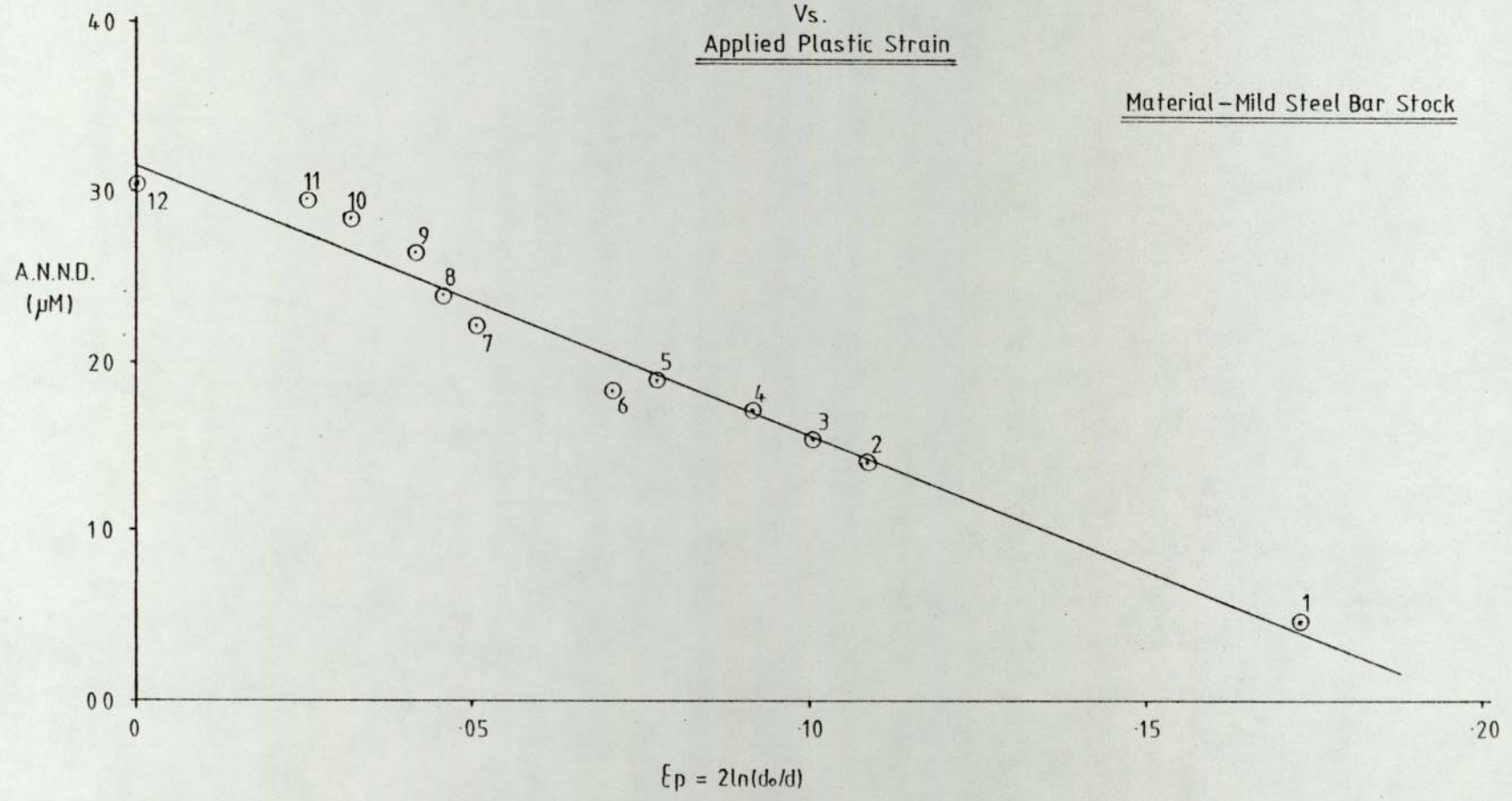

Fig. 38b

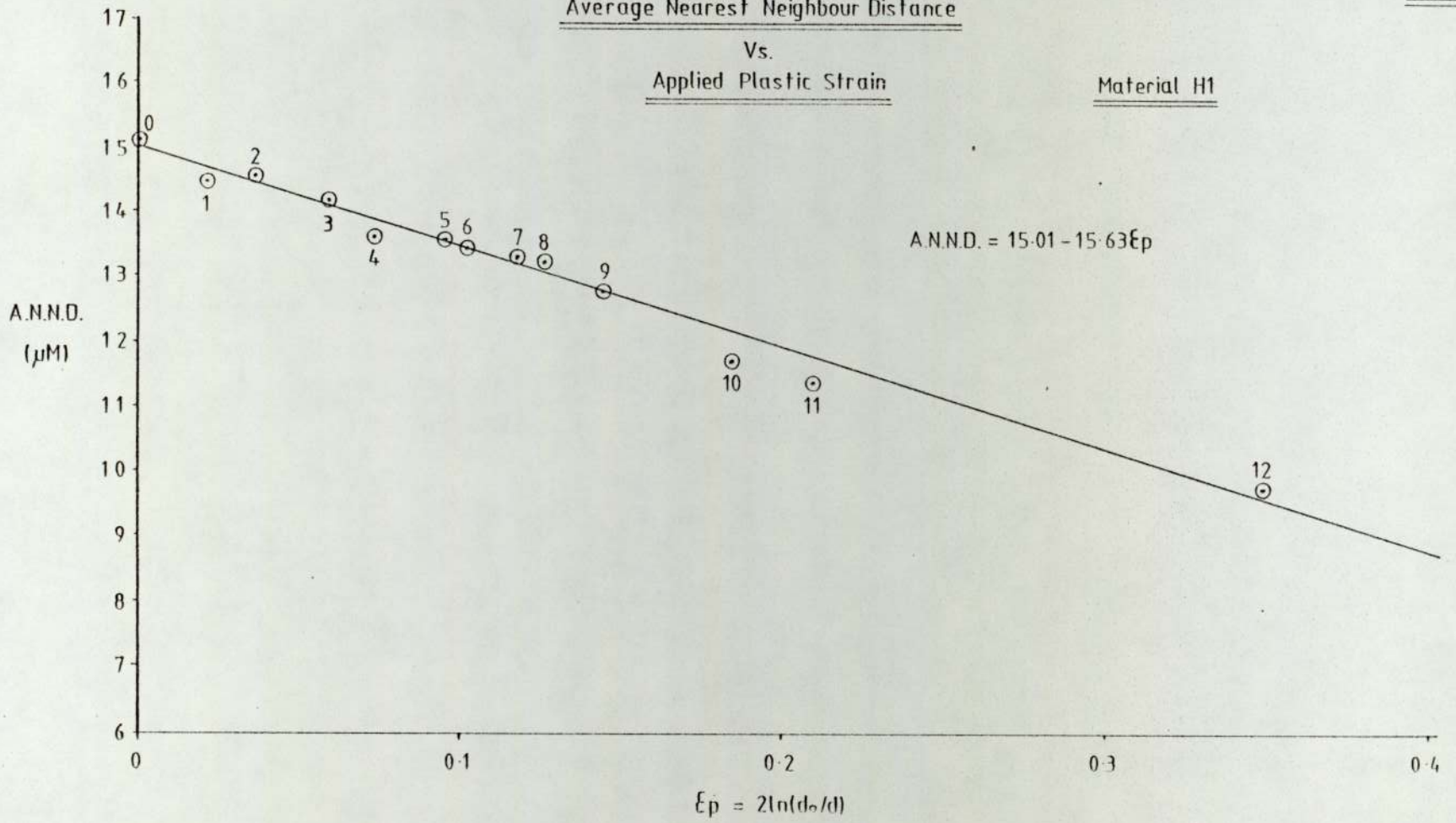
Average Nearest Neighbour Distance
Vs.
Applied Plastic Strain
Material H1
A.N.N.D. = 15·01 - 15·63εp
A.N.N.D. (μM)
17
16
15
14
13
12
11
10
9
8
7
6
0
1
2
3
4
5
6
7
8
9
10
11
12
0
0·1
0·2
0·3
0·4
εp = 2ln(d₀/d)

Fig. 38c

Average Nearest Neighbour Distance

Vs.

Applied Plastic Strain

Material H2

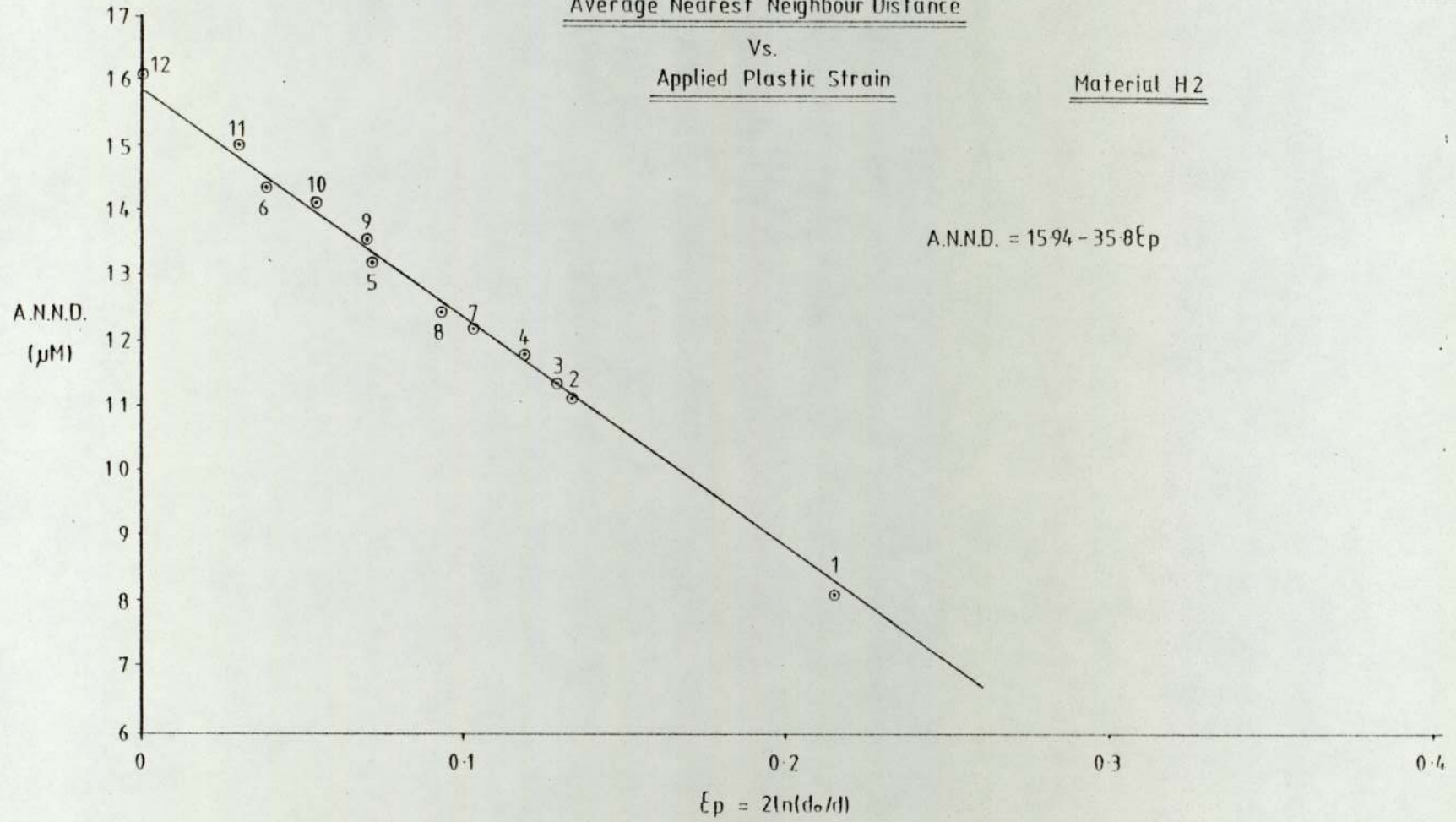

Fig. 38d

Average Nearest Neighbour Distance

Vs.

Applied Plastic Strain

Material H3

A.N.N.D. = 10·54 - 10·66ε_p

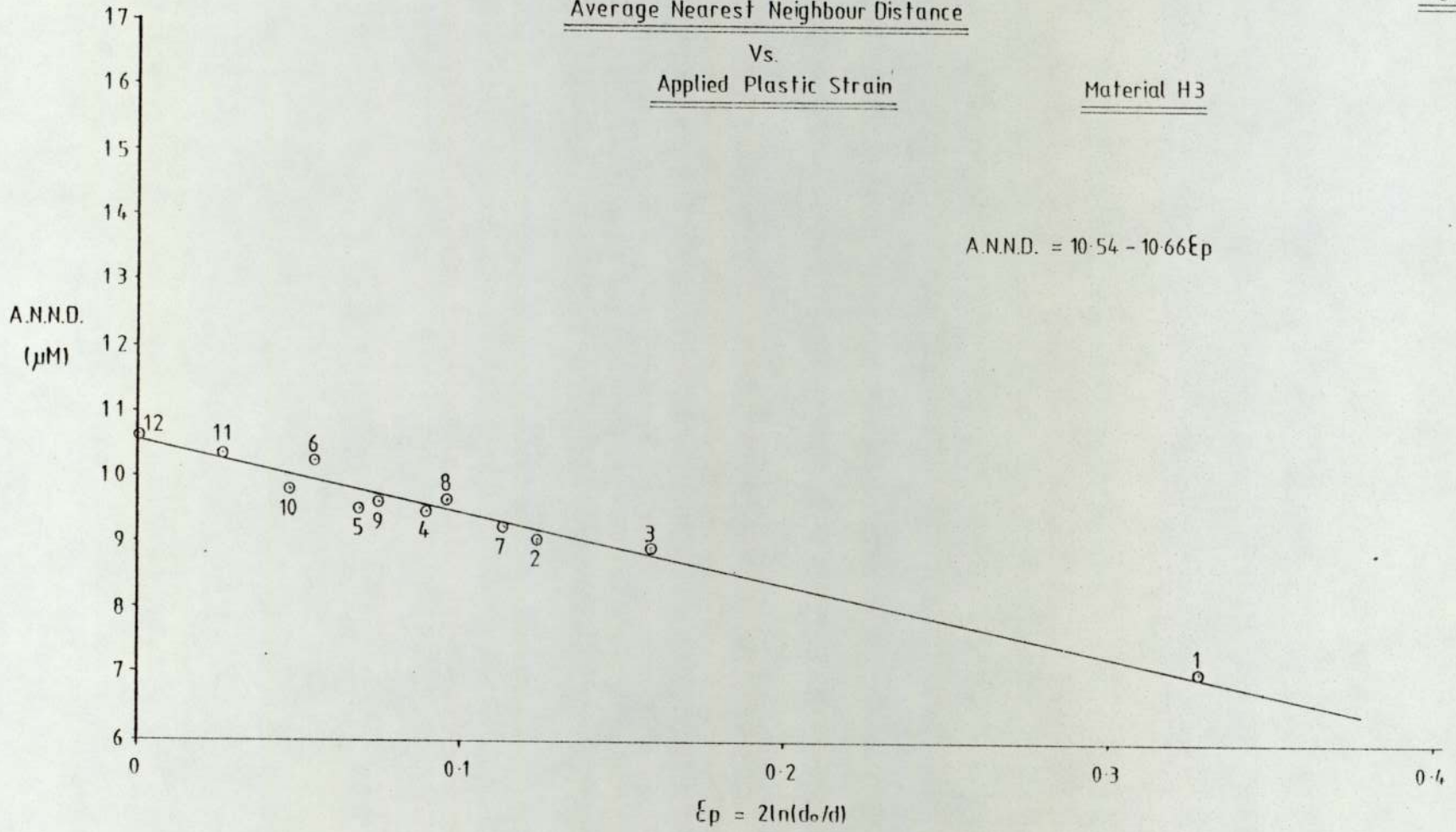

Fig. 38e

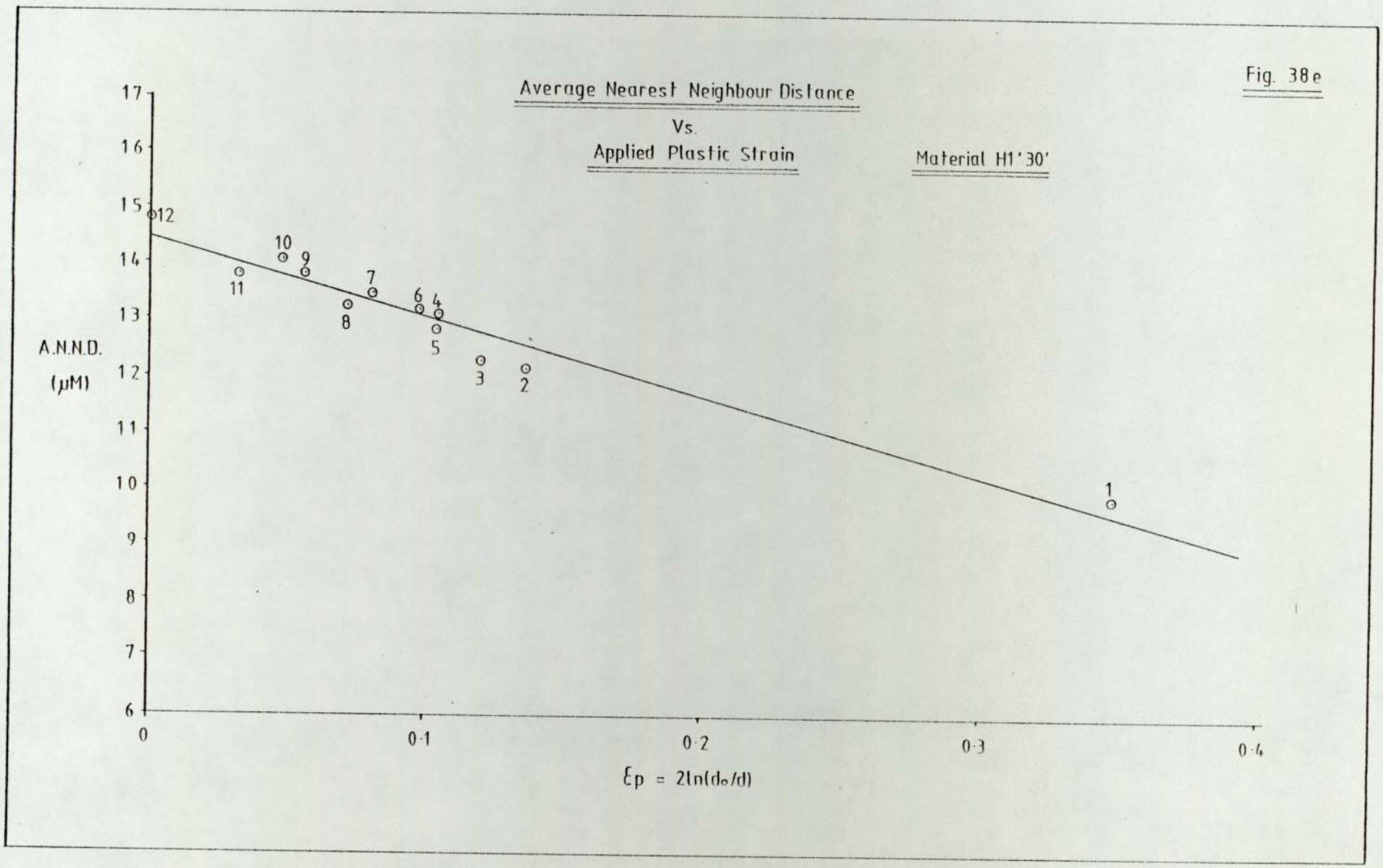
Average Nearest Neighbour Distance
Vs.
Applied Plastic Strain
Material H1'30'
A.N.N.D.
(μM)
17
16
15
14
13
12
11
10
9
8
7
6
12
10
9
11
7
8
6
4
5
3
2
1
0
0·1
0·2
0·3
0·4
εp = 2ln(d₀/d)

Fig. 38 f

Average Nearest Neighbour Distance

Vs.

Applied Plastic Strain

Material H2 '30'

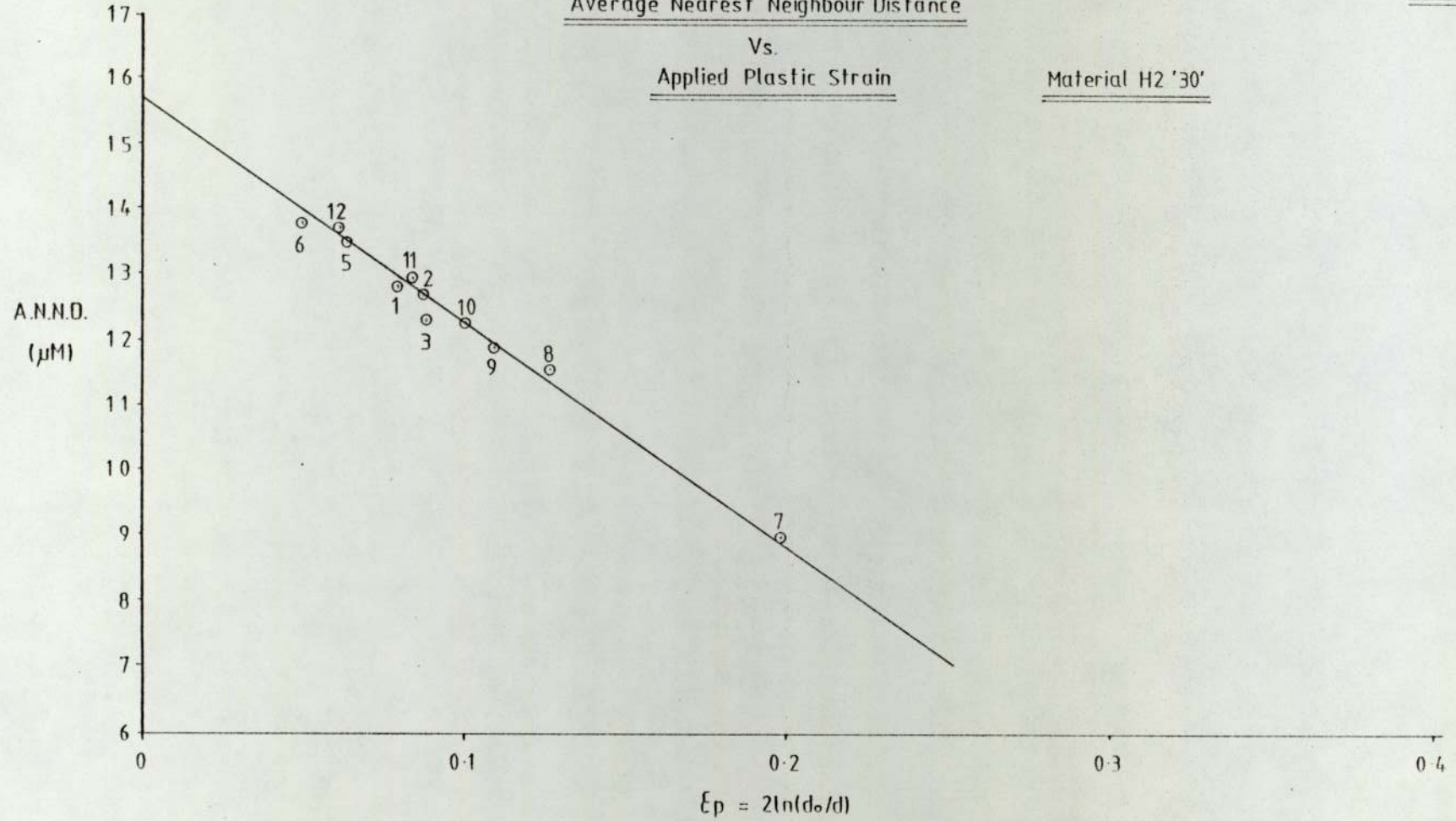

Fig 38g

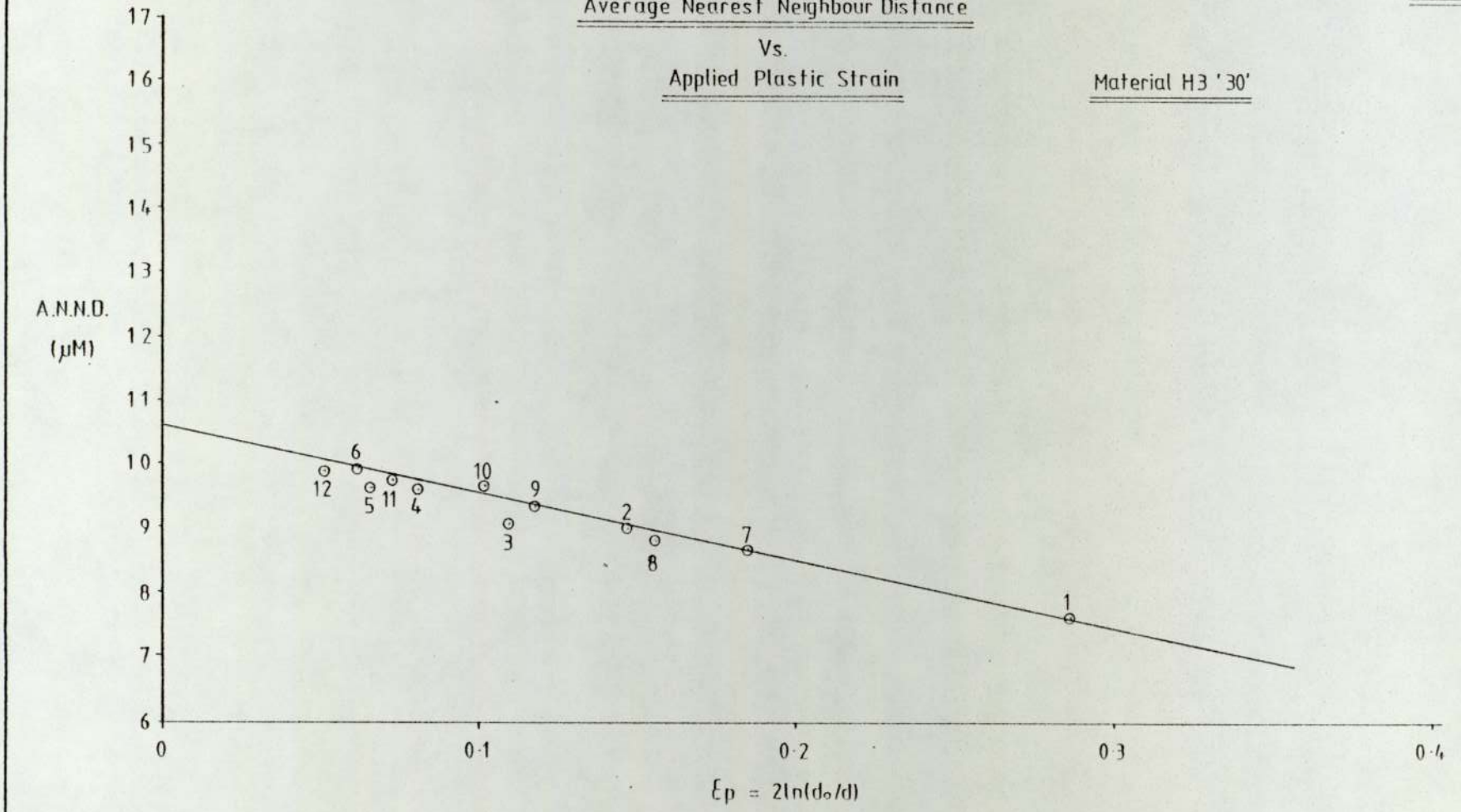
Average Nearest Neighbour Distance
Vs.
Applied Plastic Strain
Material H3 '30'
A.N.N.D.
(μM)
17
16
15
14
13
12
11
10
9
8
7
6
0
0·1
0·2
0·3
0·4
εp = 2ln(do/d)
12
6
5
11
4
10
3
9
2
8
7
1

Fig. 39a

Void Size Vs. Strain

Material H1

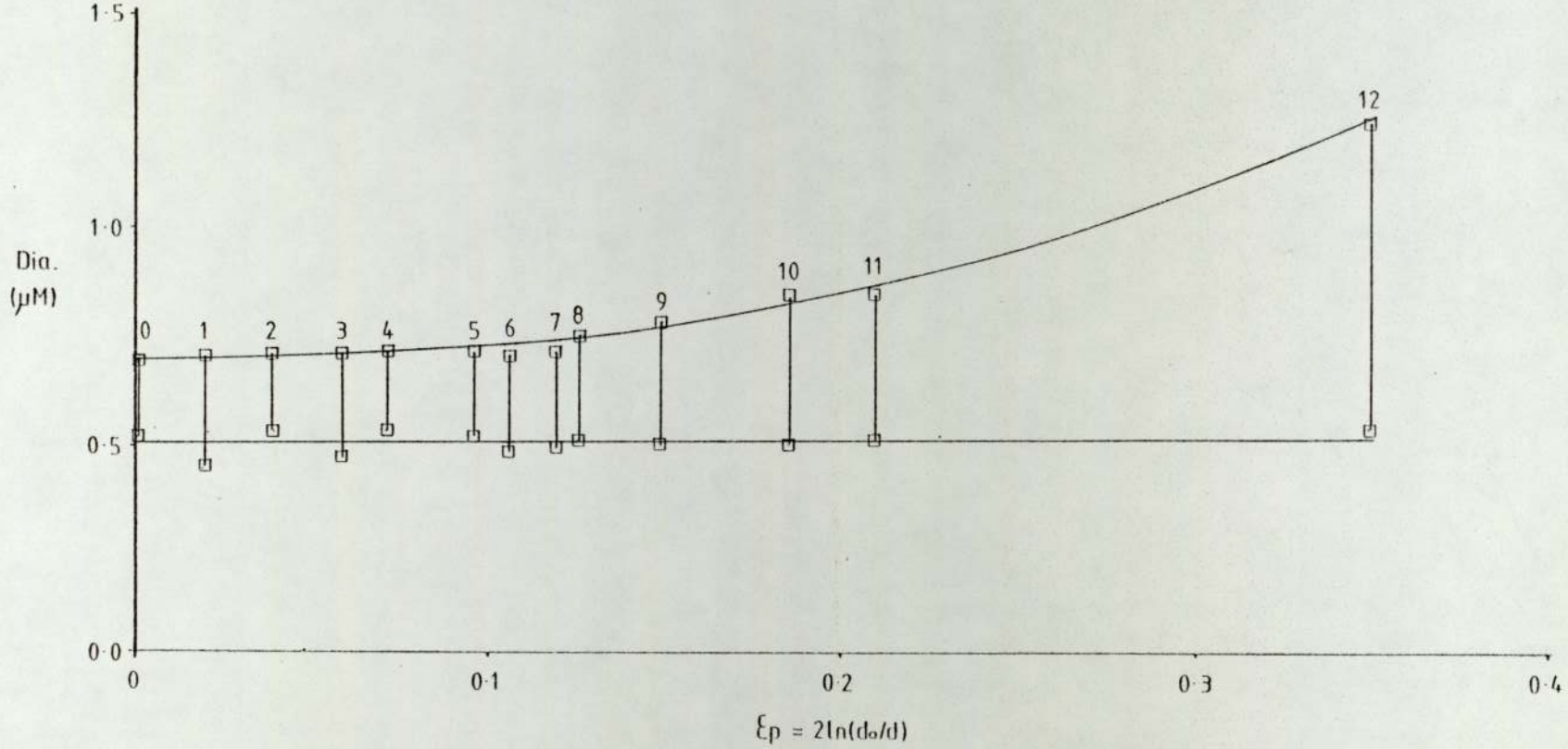

Fig. 39 b

Void Size Vs. Strain

Material H2

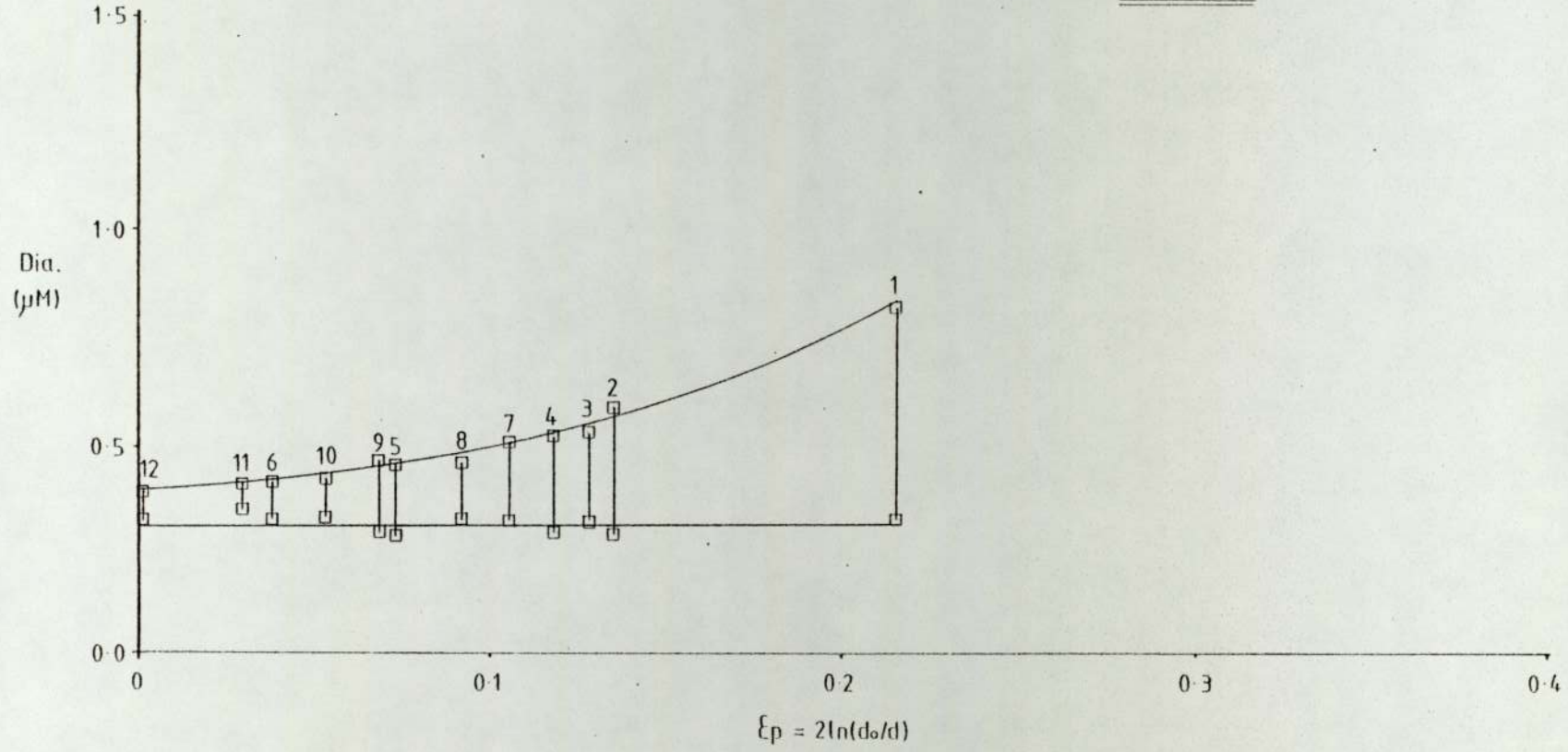

Fig. 39 c

Void Size Vs. Strain

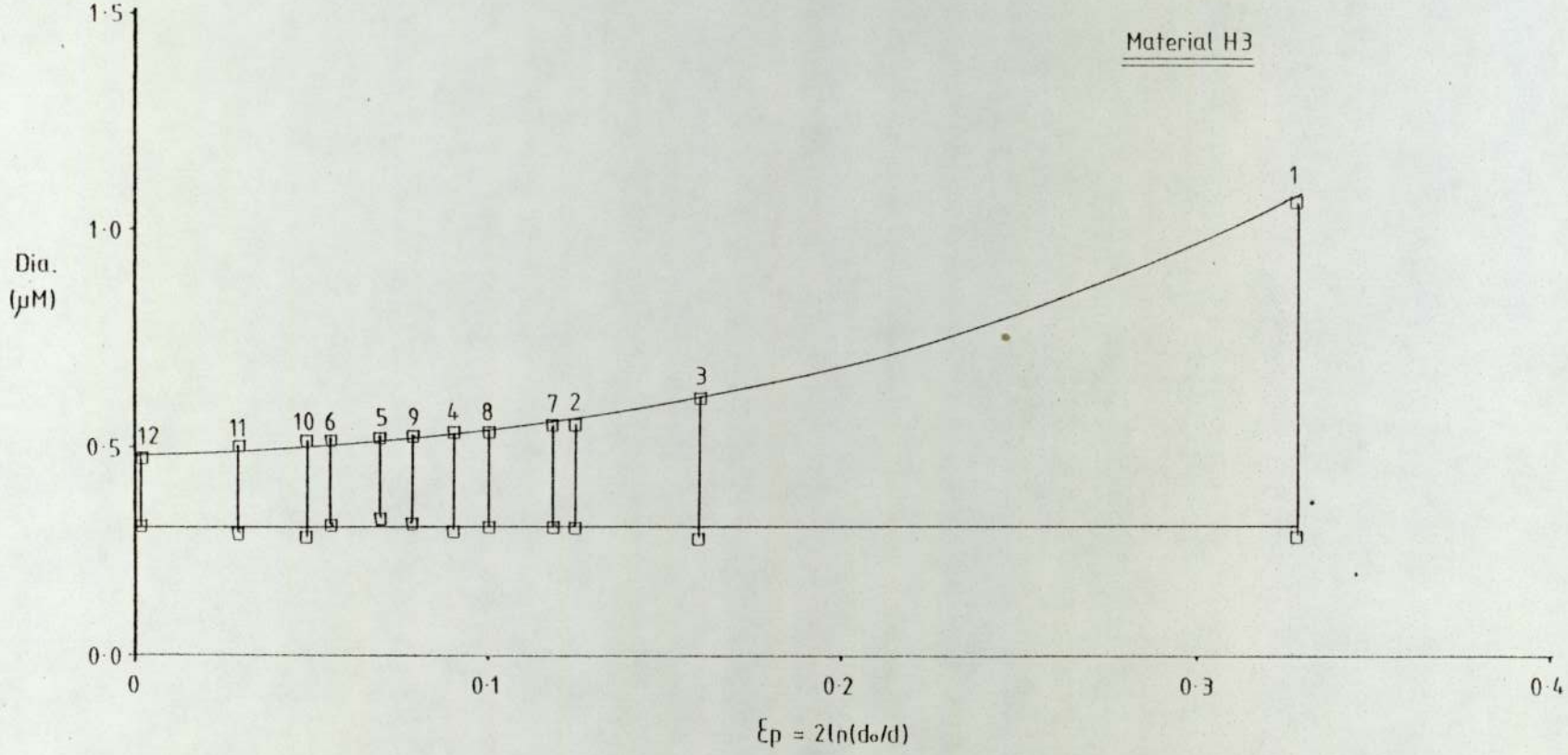

Fig. 39 d

Void Size Vs. Strain

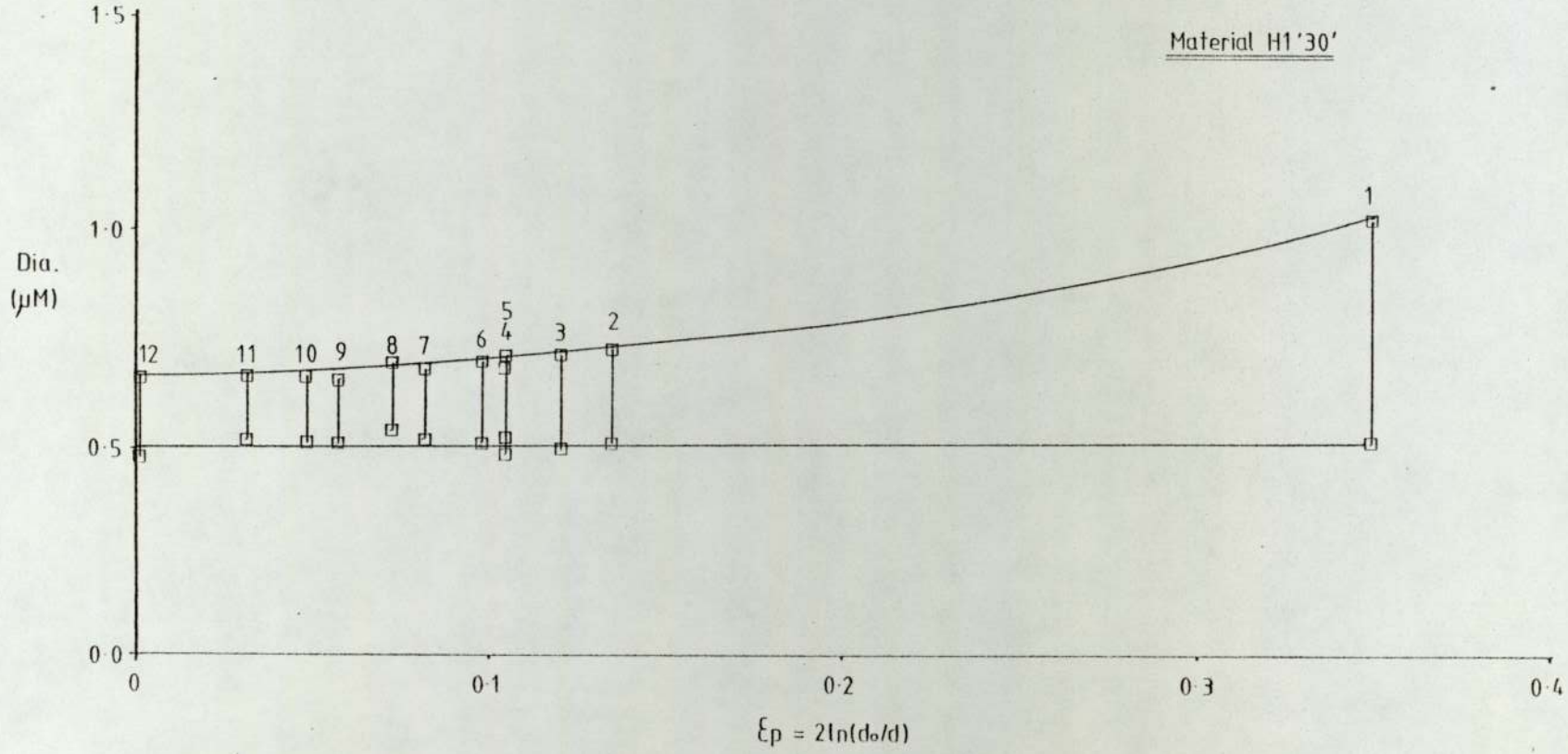

Fig. 39 e

Void Size Vs. Strain

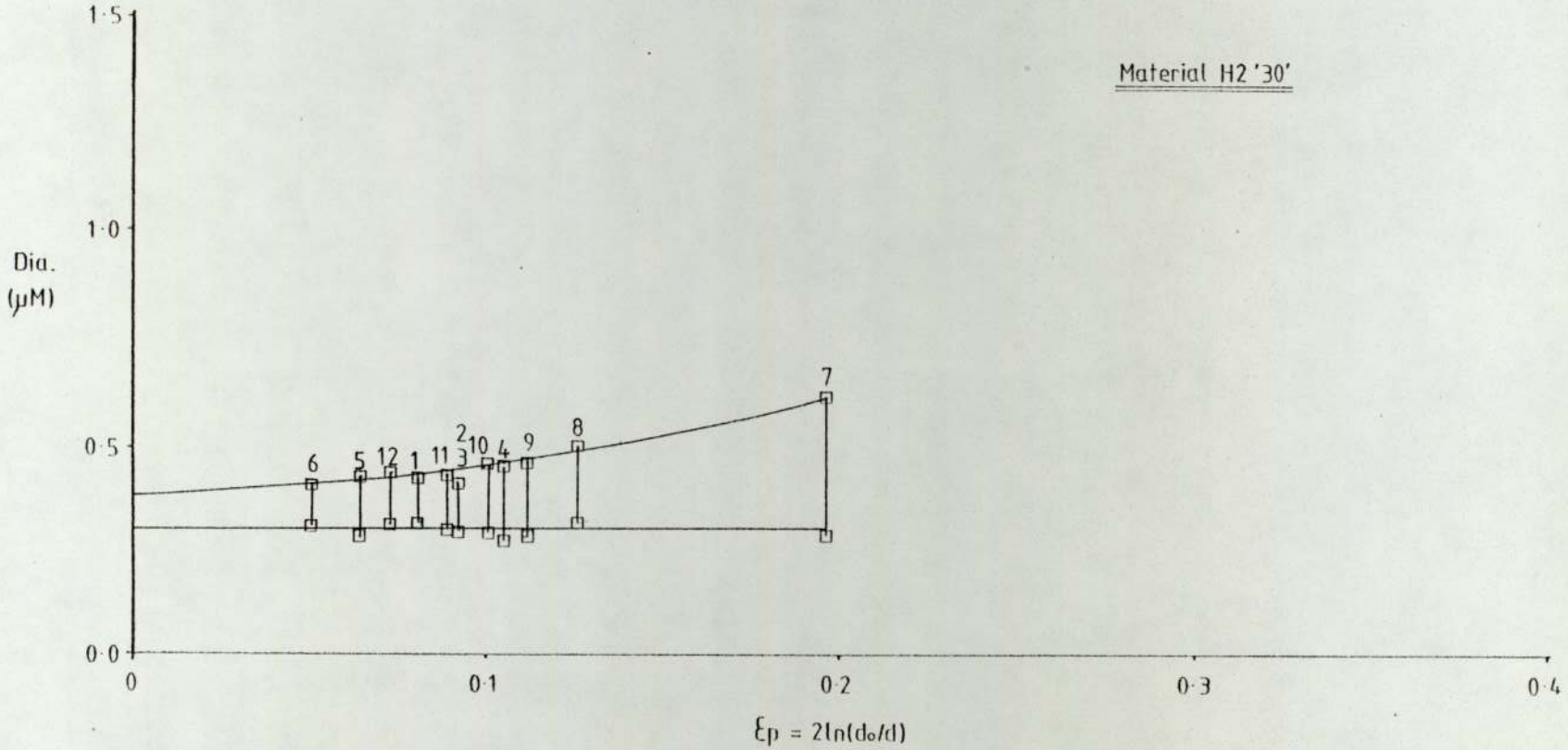

Fig. 39 f

Void Size Vs. Strain

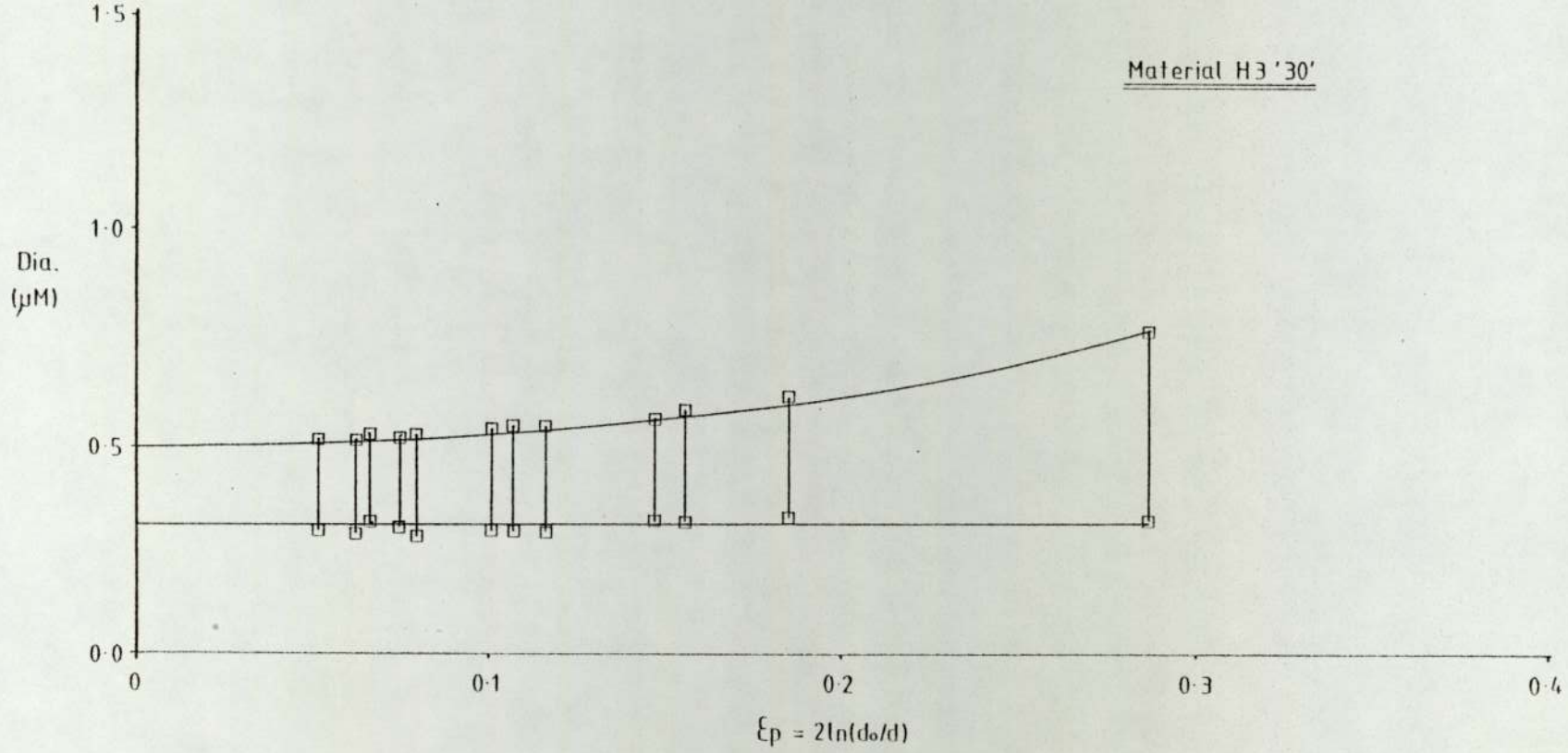

Sub-notch damage Notch H1-5

Fig. 40a

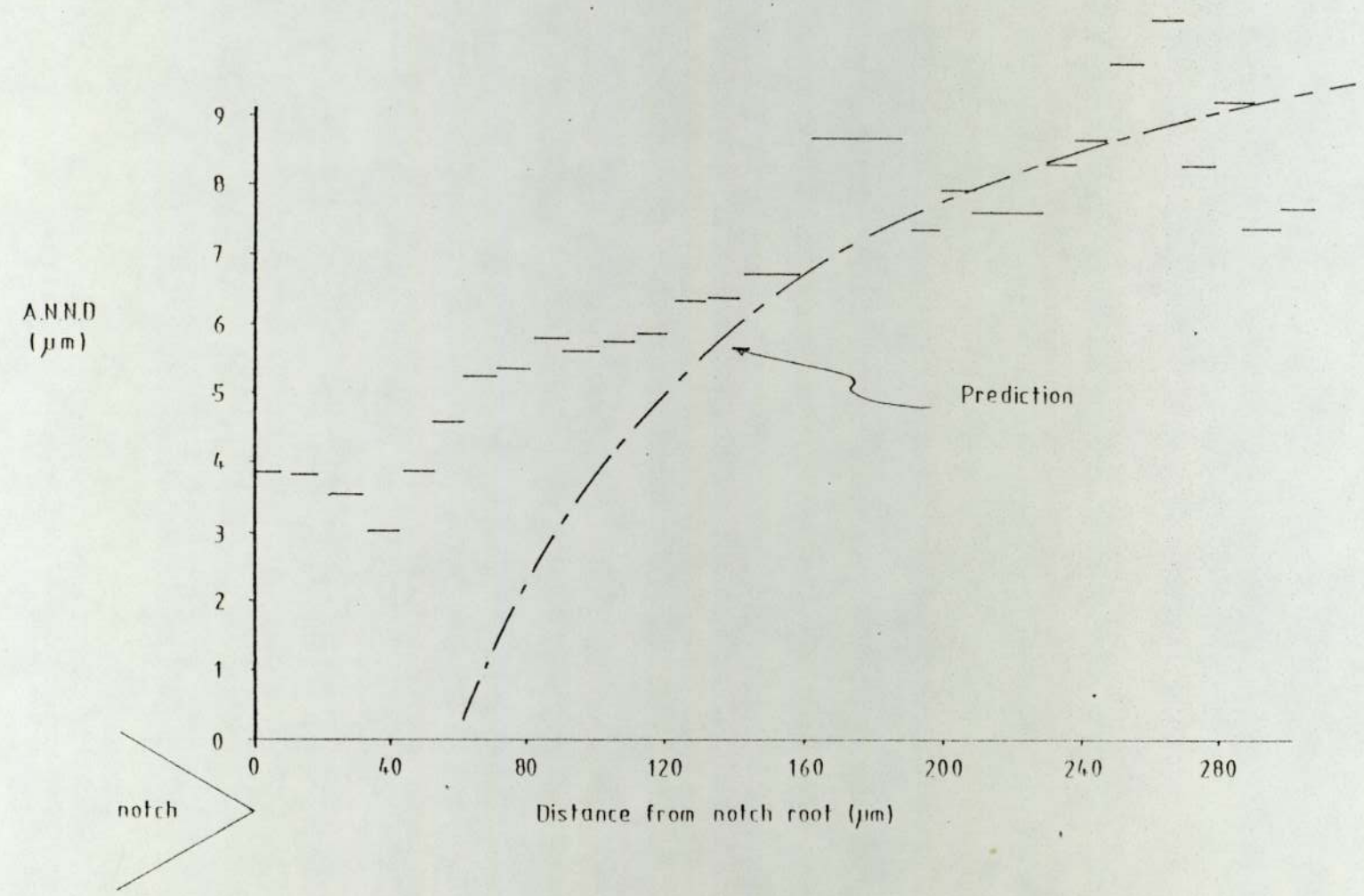

Sub-notch damage Notch H1-4

Fig. 40b

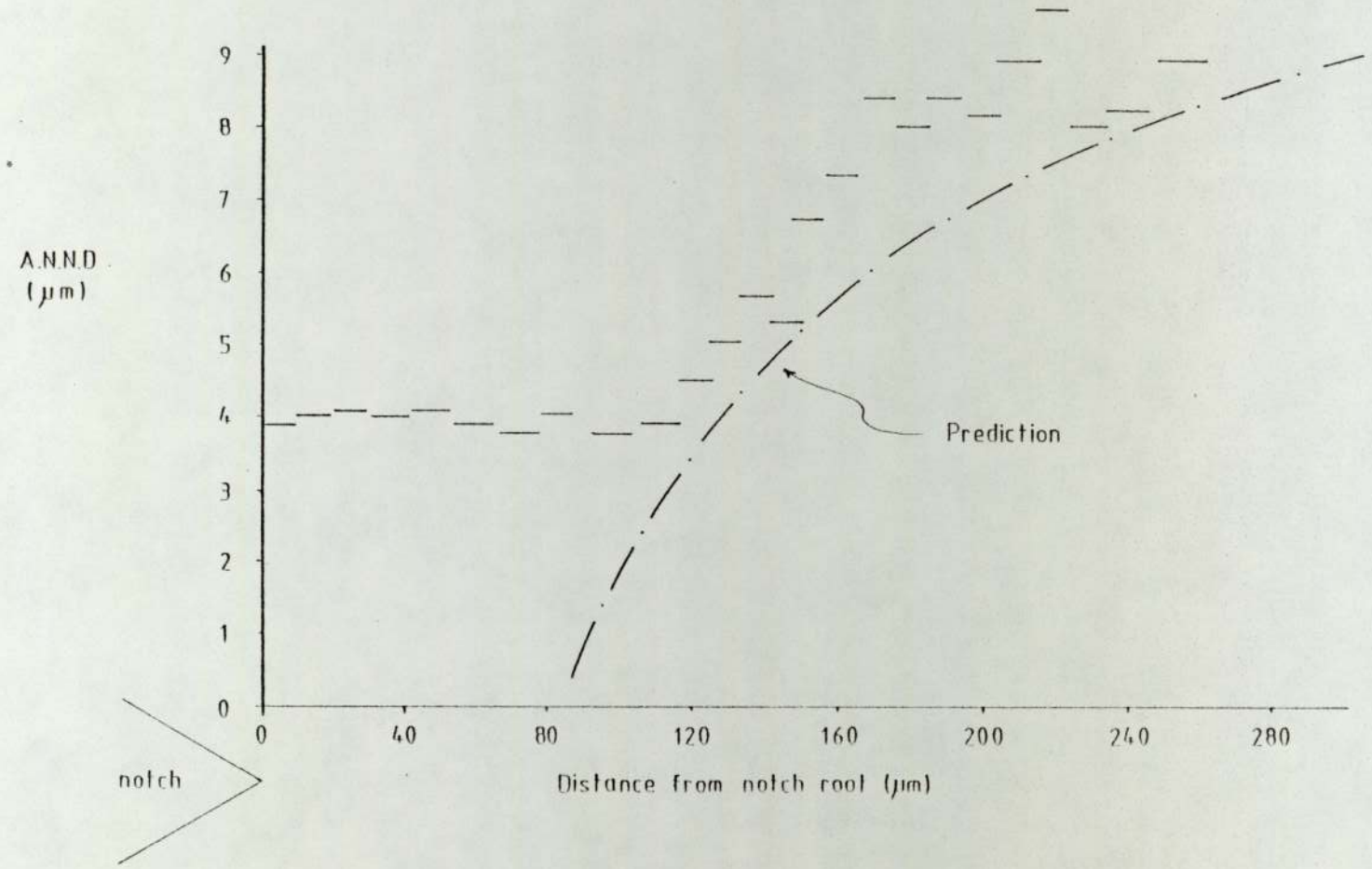

Sub-notch damage Notch H1-3

Fig. 40c

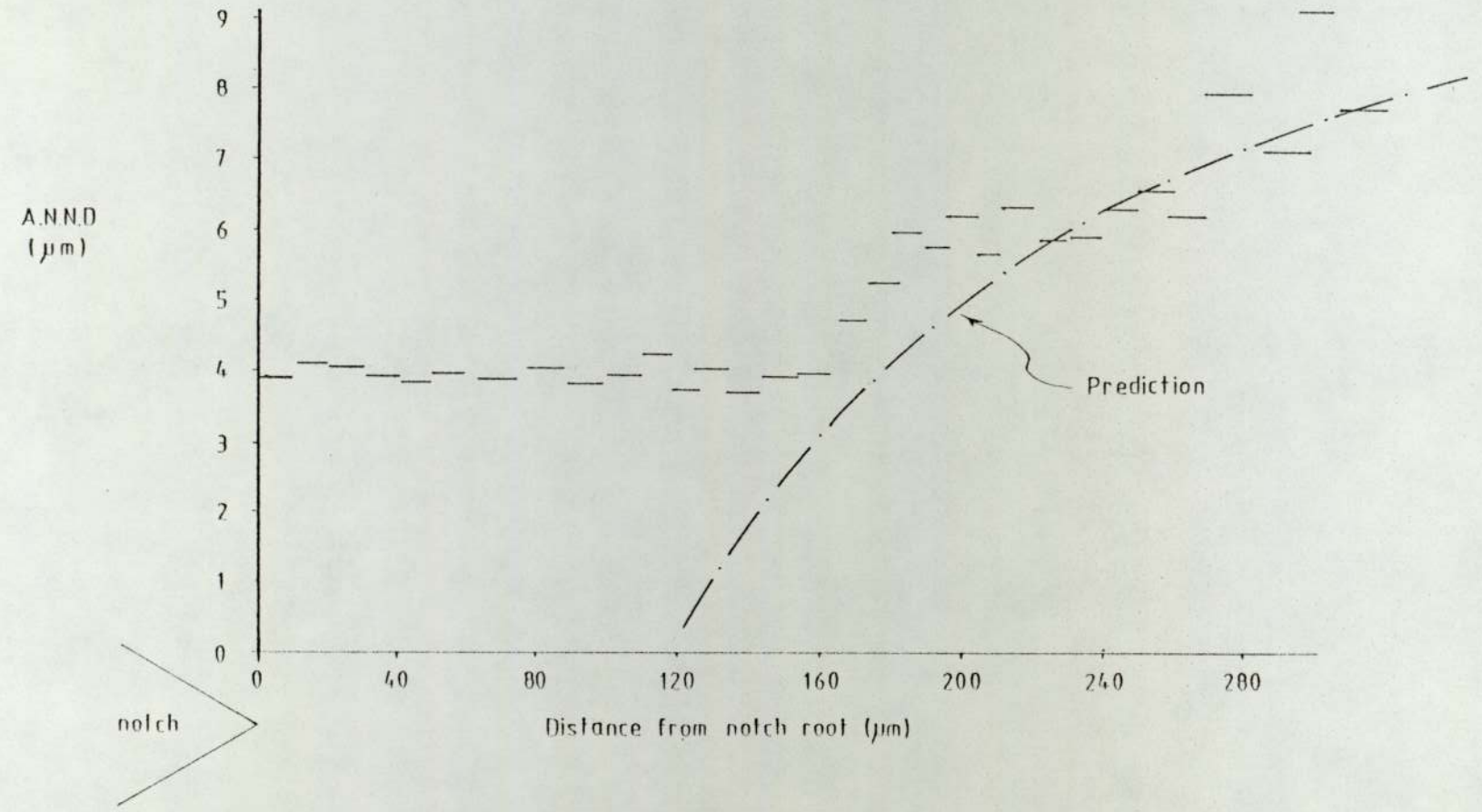

Sub-notch damage Notch H3-5

Fig 40d

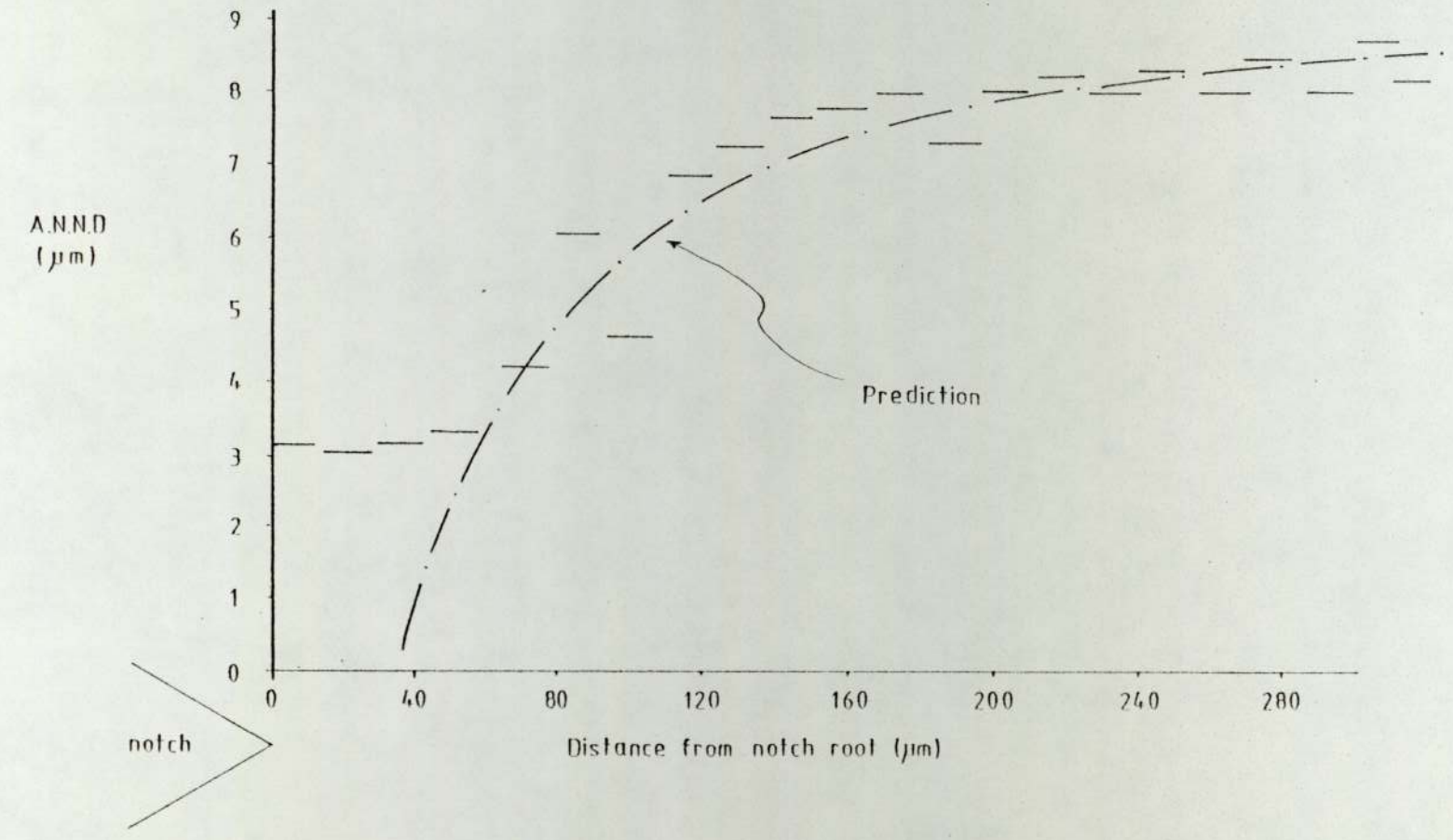

Sub-notch damage Notch H3-3

Fig. 40e

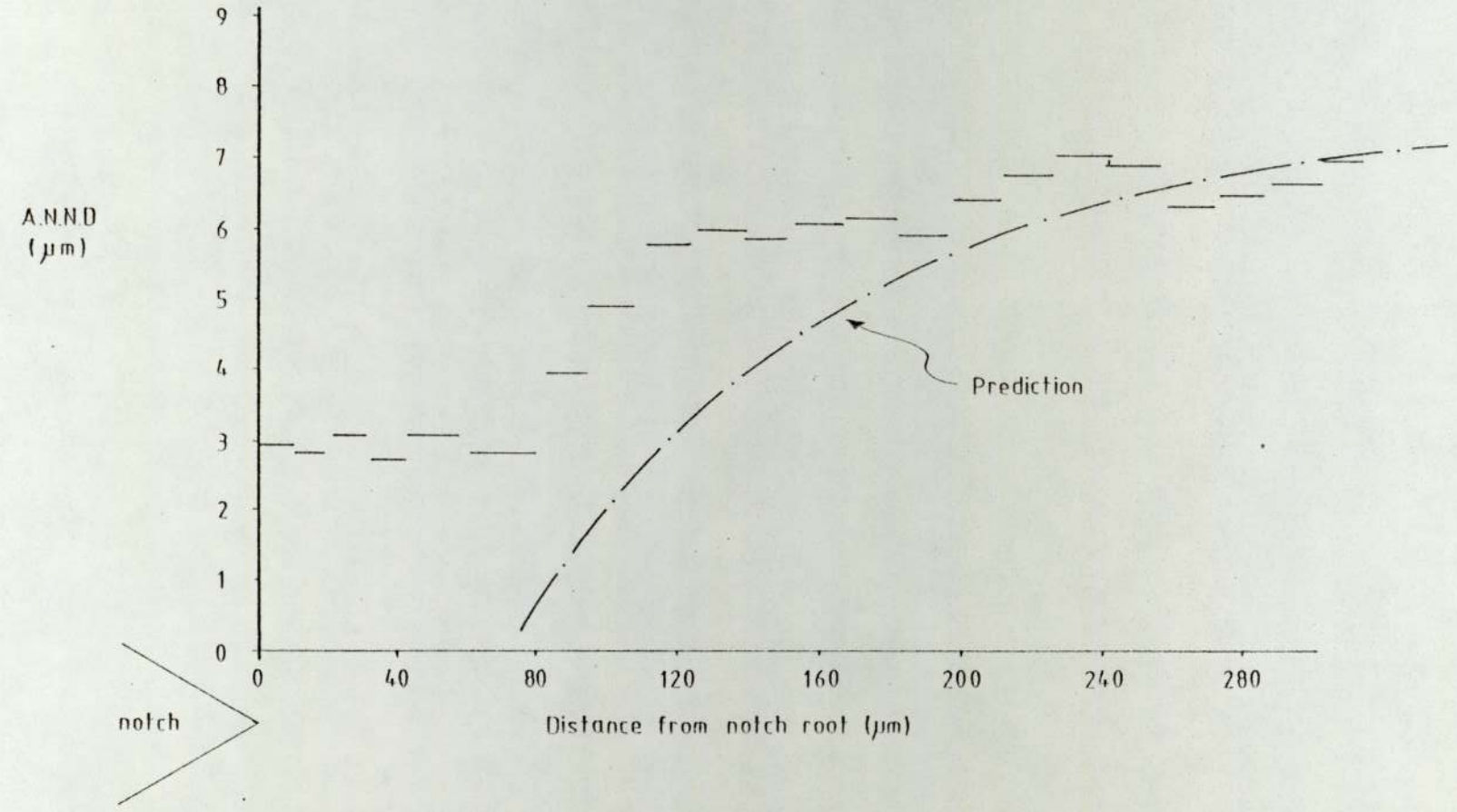

Sub-notch damage Notch H3-1

Fig. 40f

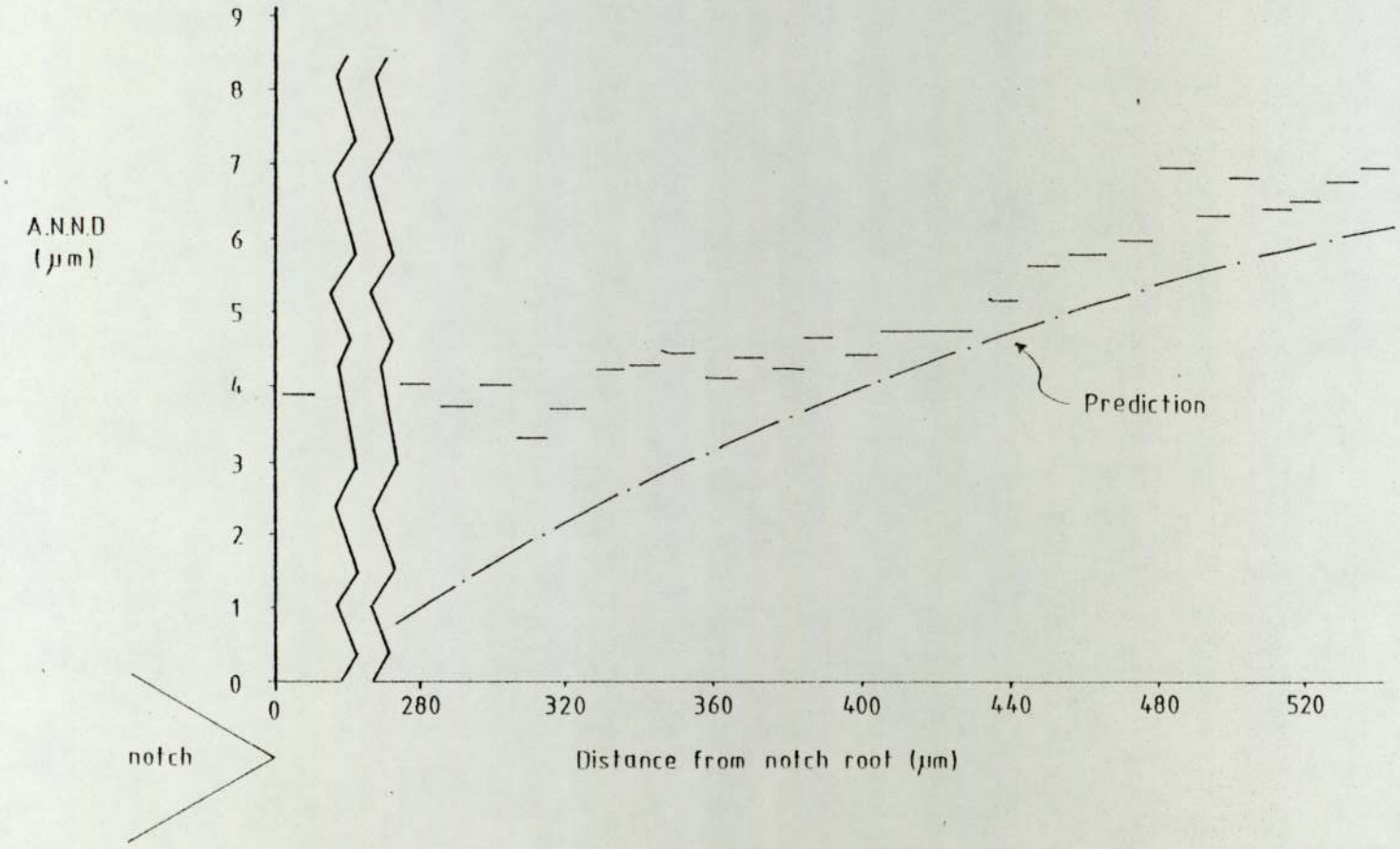

Fig 41a

Uniaxial stress-strain curve

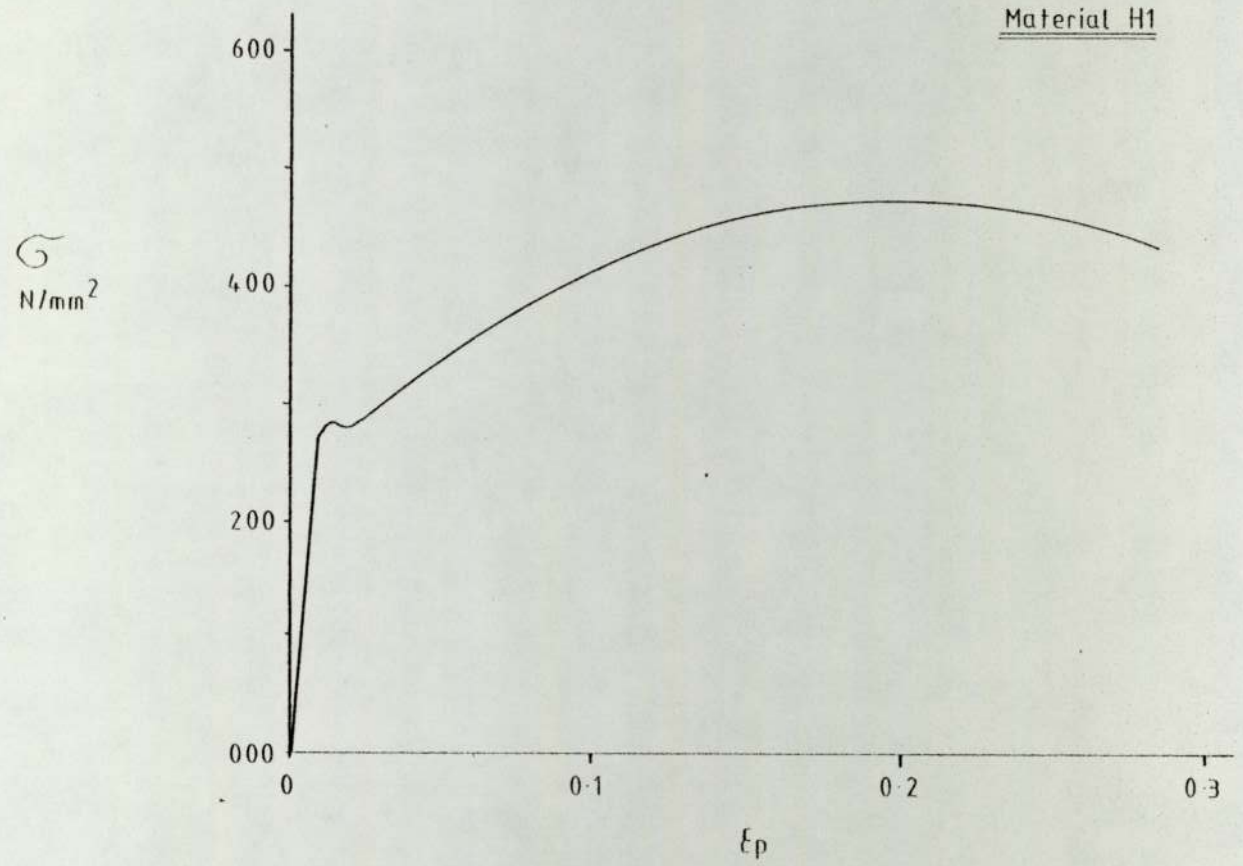

Fig. 41b

Uniaxial stress-strain curve

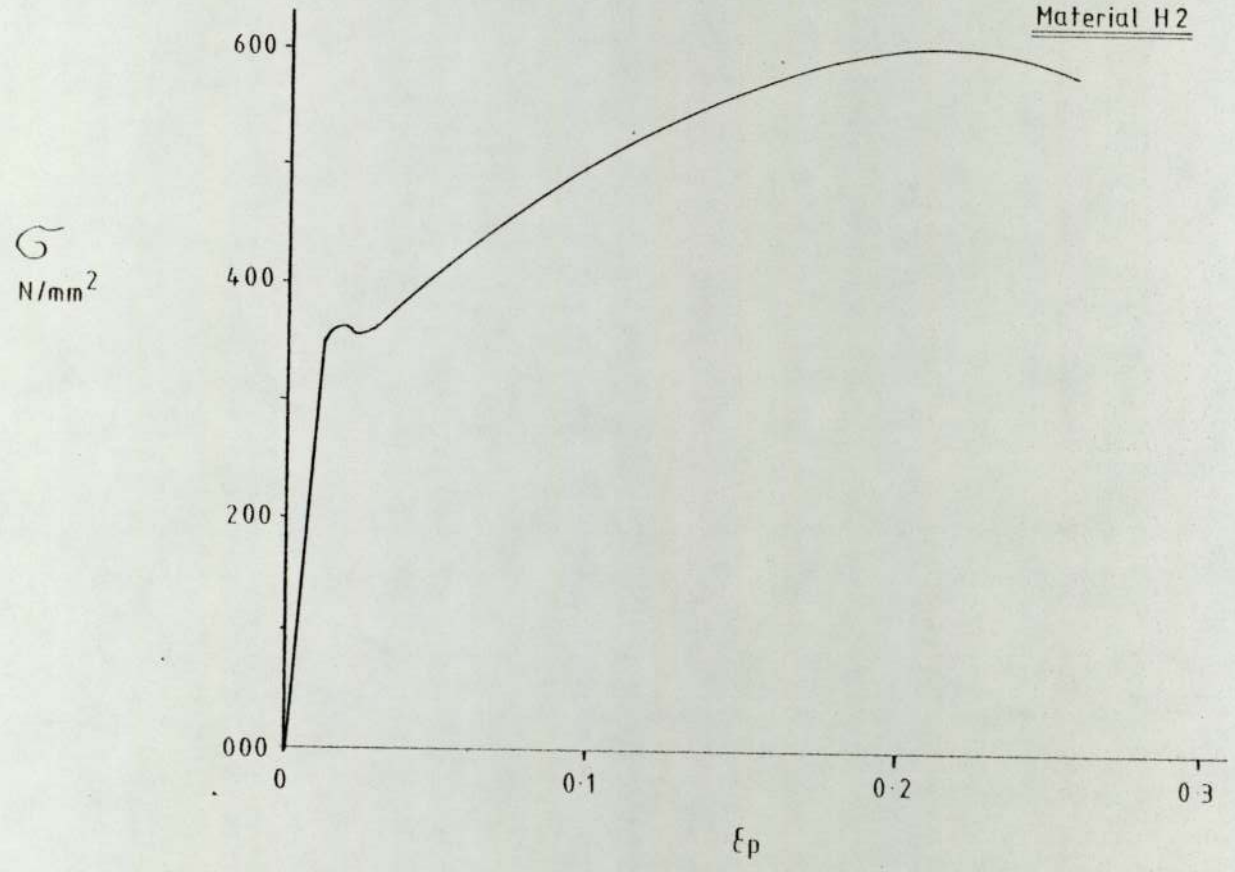

Fig. 41c

Uniaxial stress-strain curve

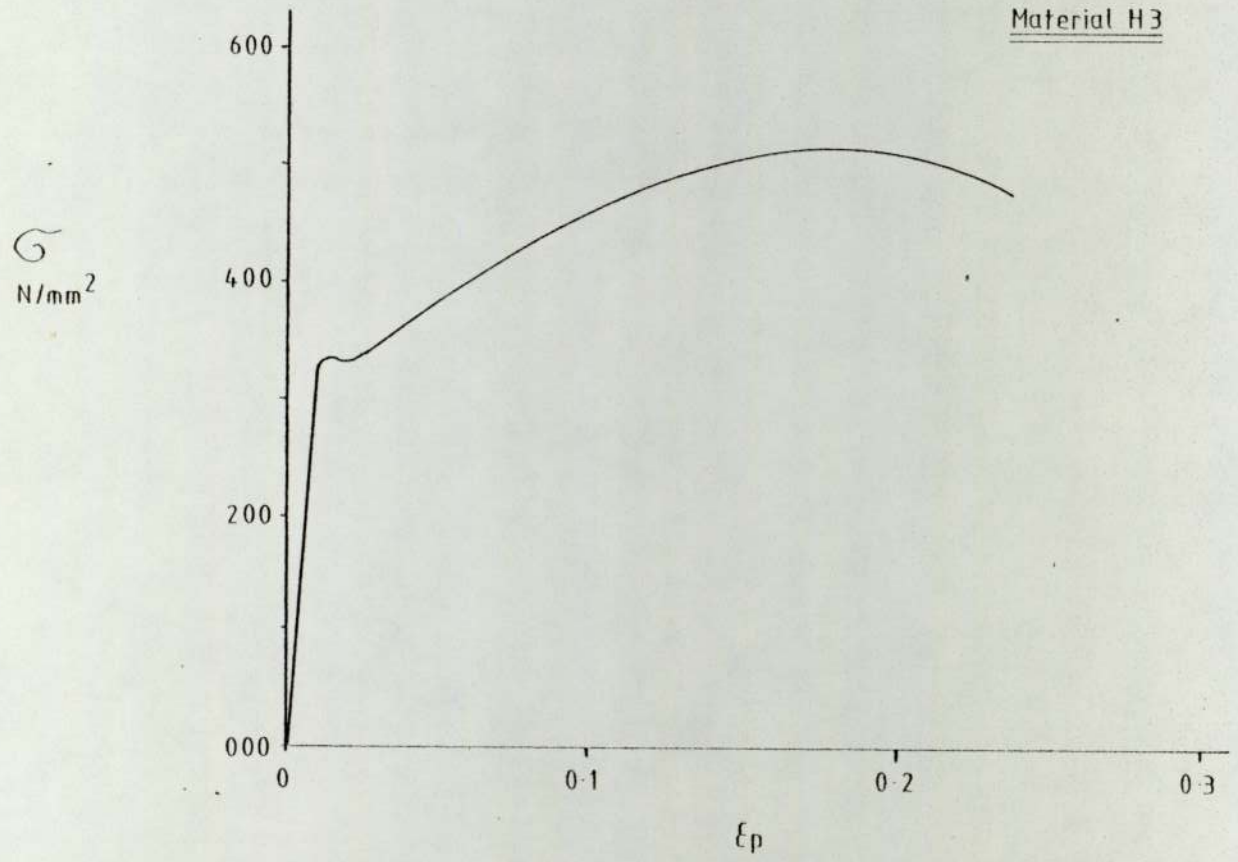

Fig. 41d

Uniaxial stress-strain curve

Material 50D

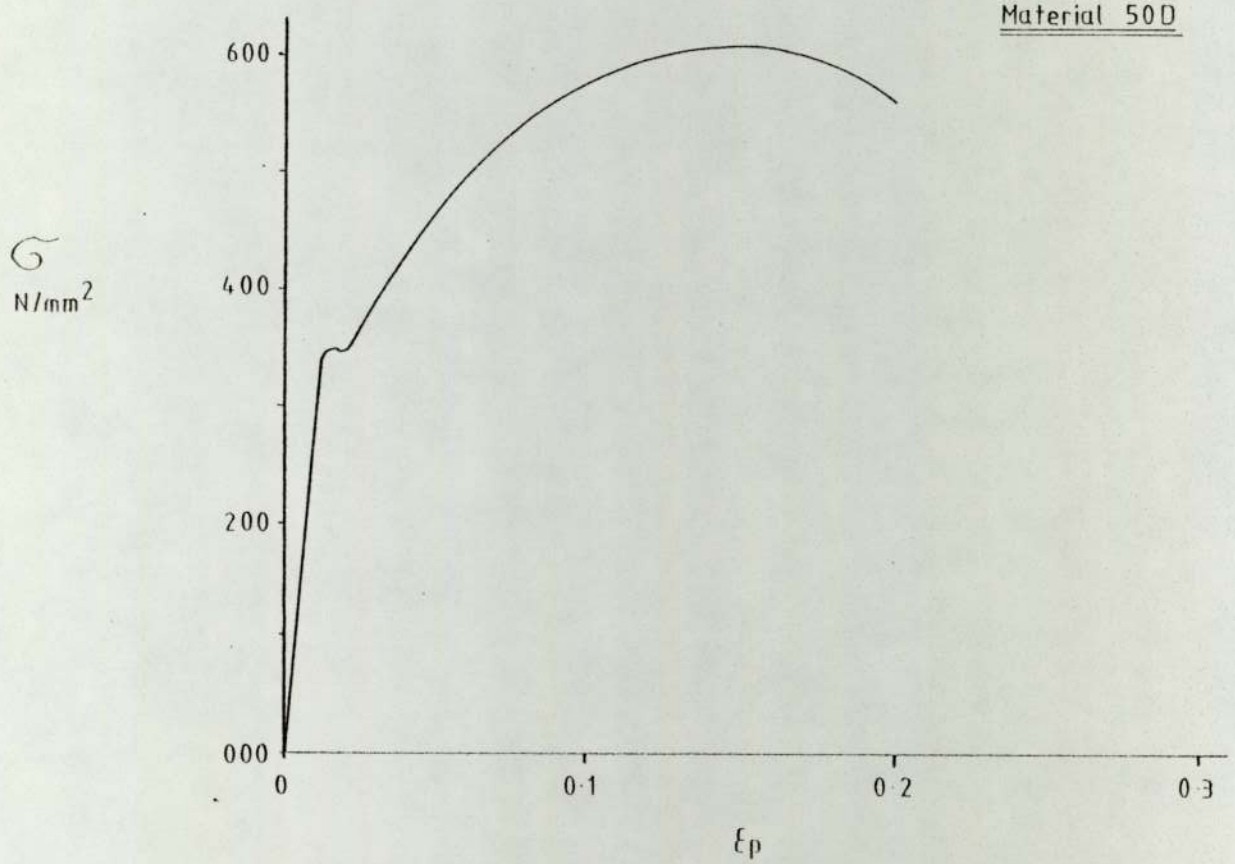

Fig. 42a

Strain profile for S 05

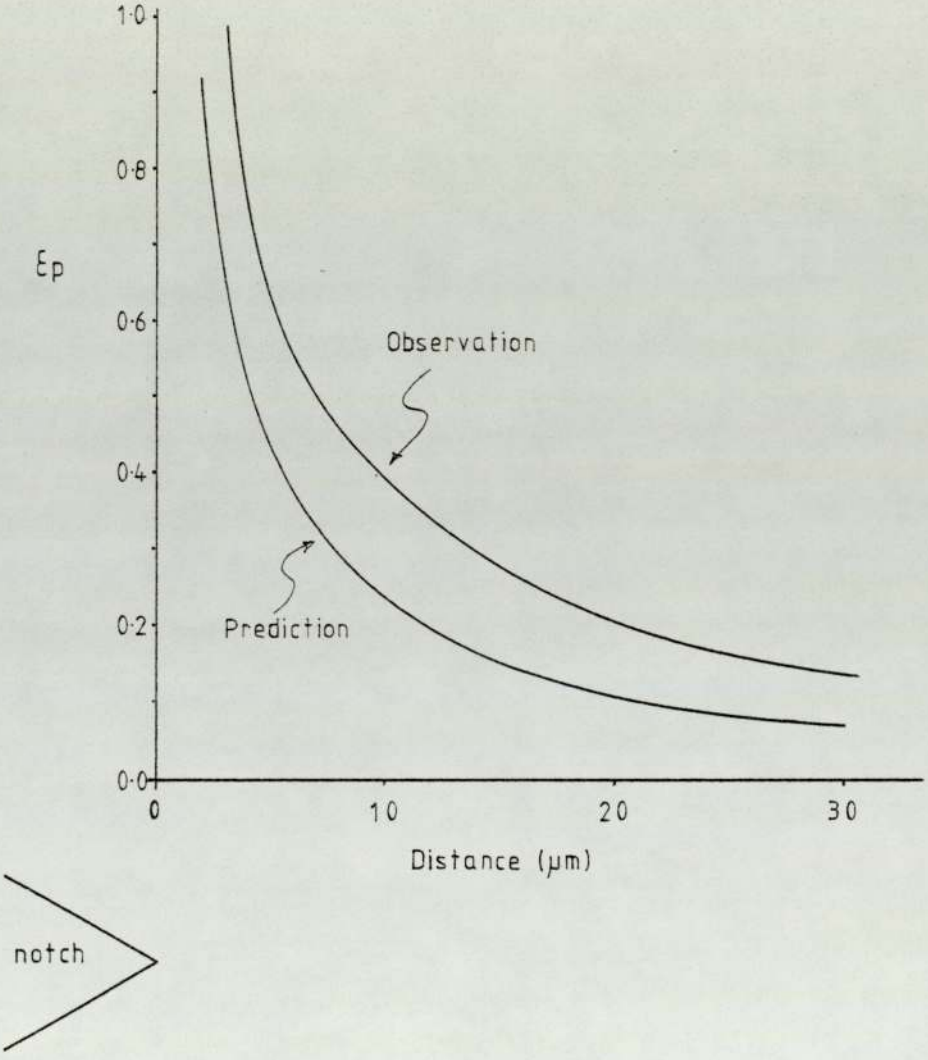

Fig 42b

Strain profile for S 30

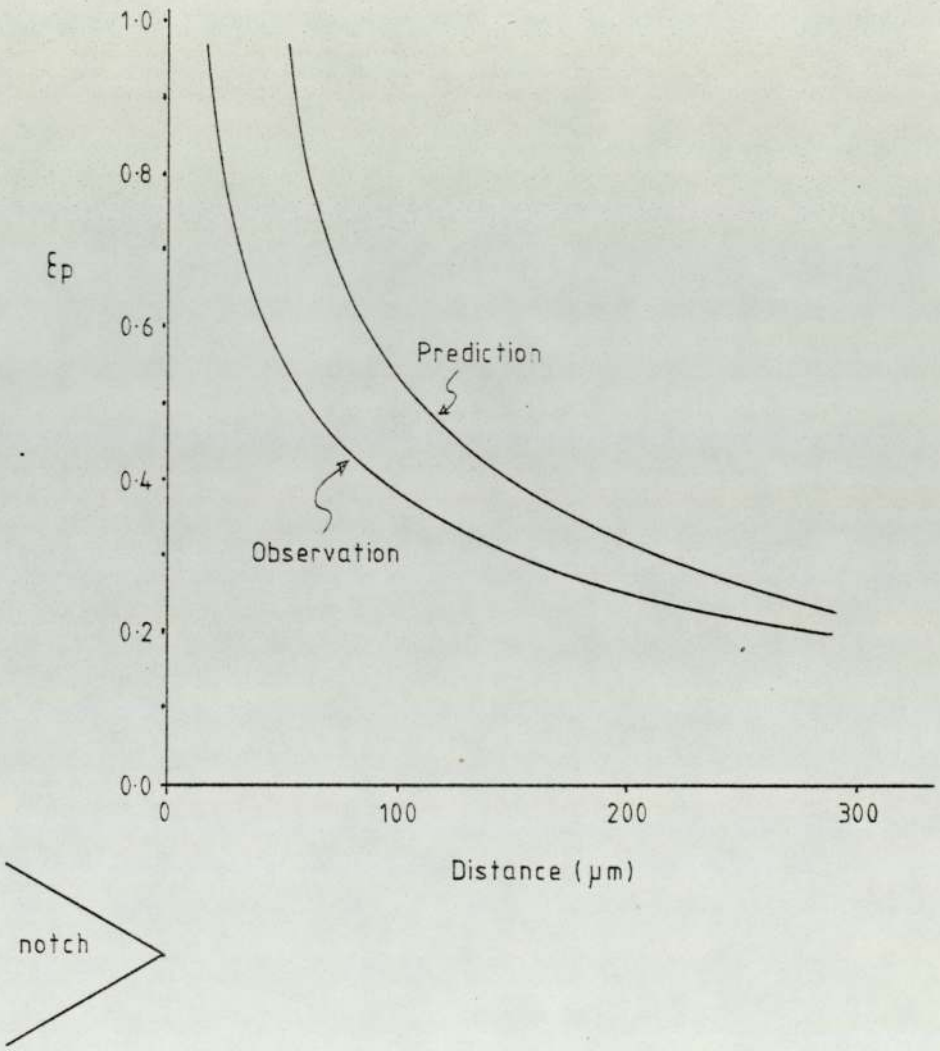

Fig. 42c

Strain profile for S40

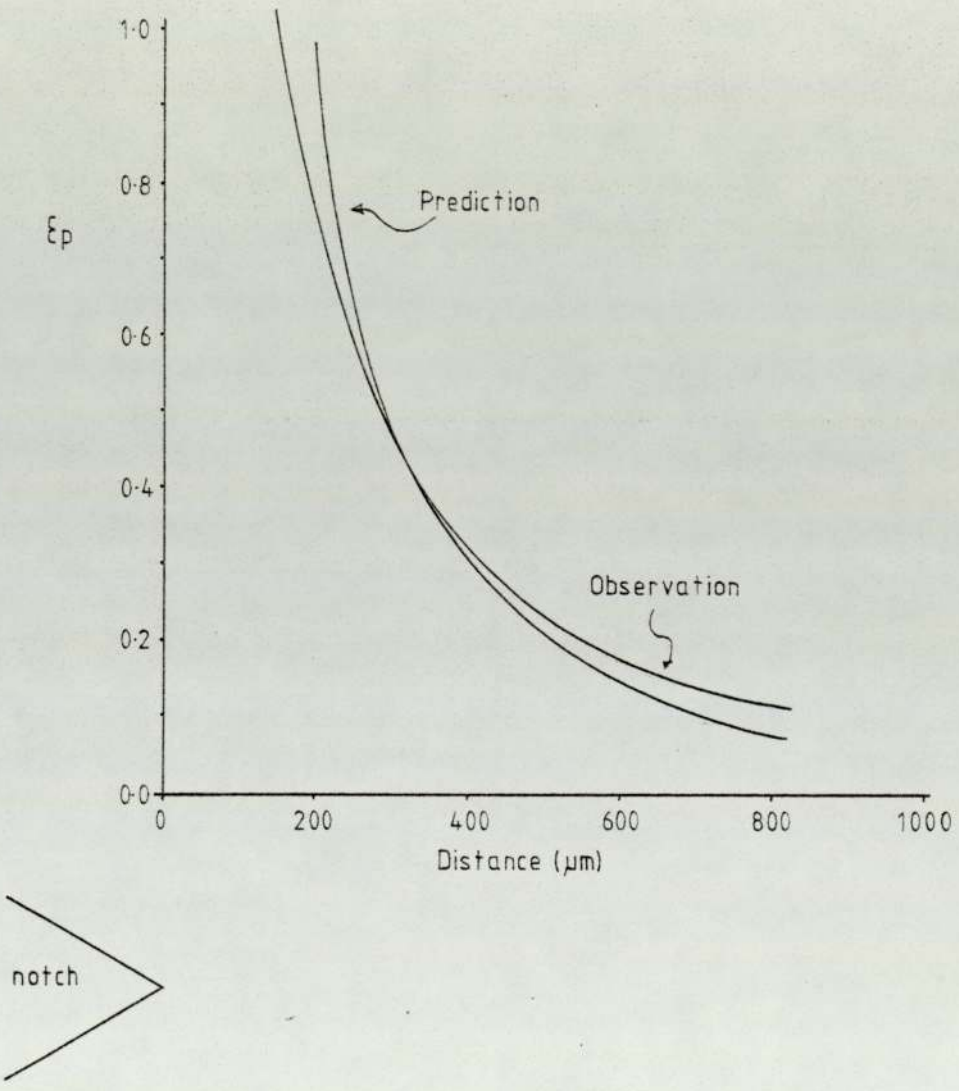

Fig. 43

Broken open bend specimen

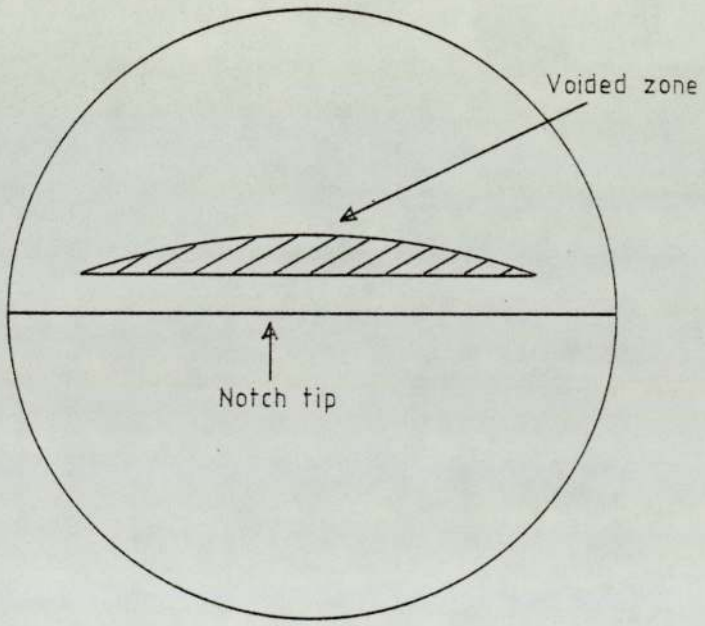

Fig. 44

Sheet aluminium specimen

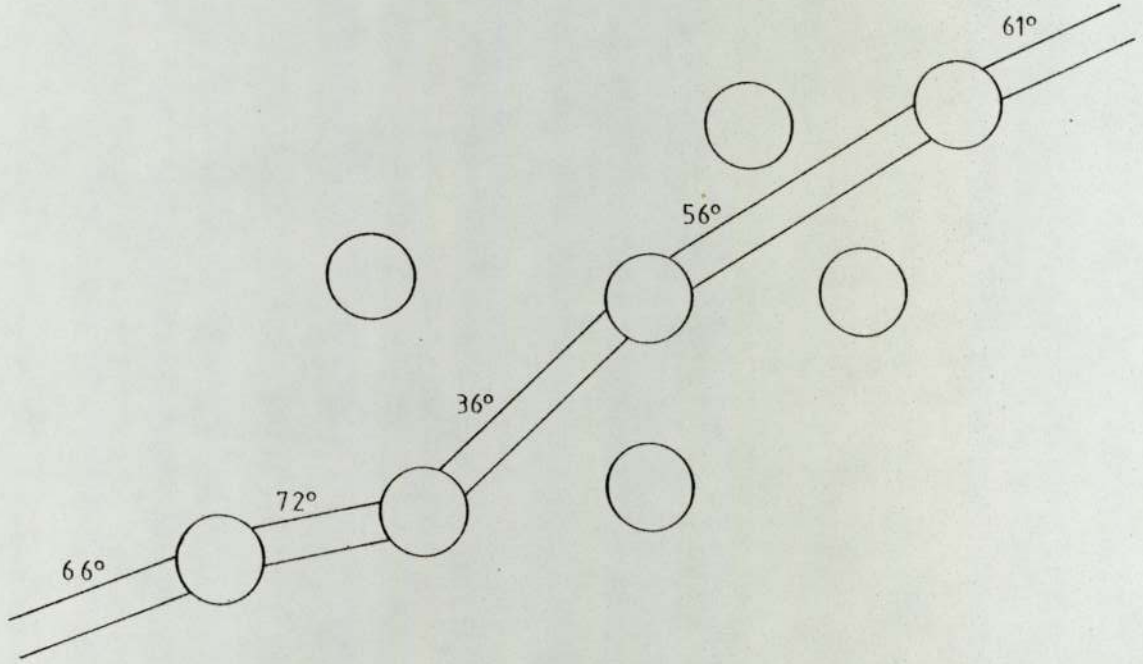

Fig. 45

Stress state dependence

of

B.S. 4360 50D

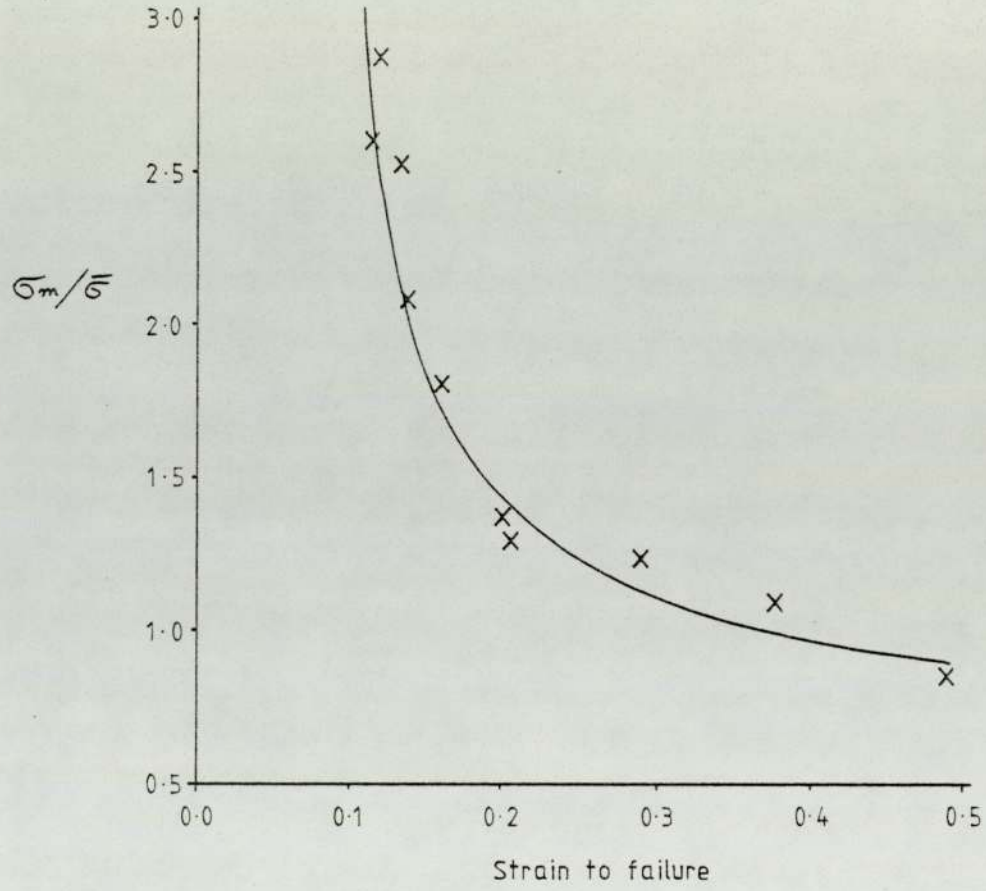

Fig. 46

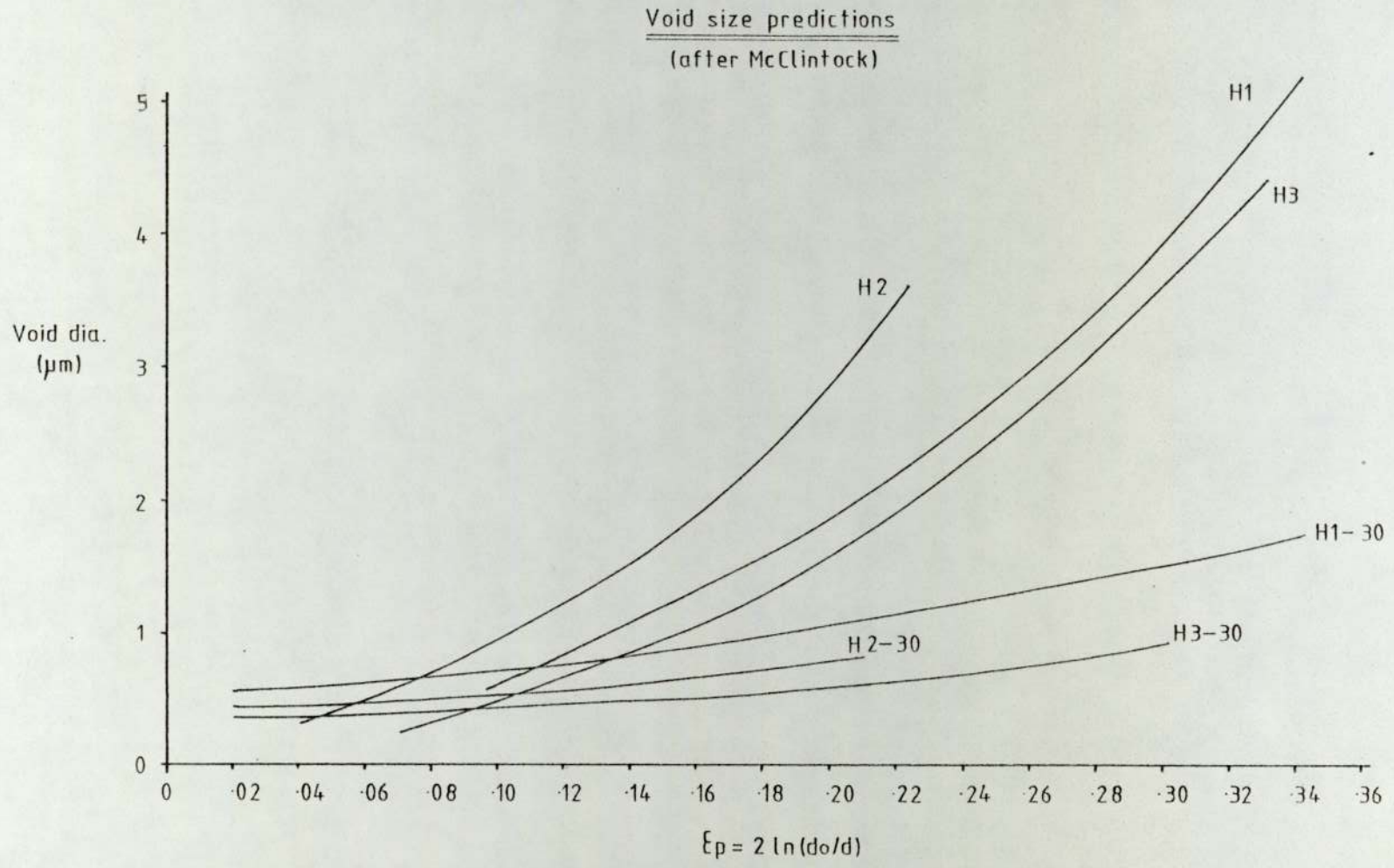
Void size predictions
(after McClintock)
Void dia.
(μm)
5
4
3
2
1
0
H1
H3
H2
H1-30
H2-30
H3-30
0
·02
·04
·06
·08
·10
·12
·14
·16
·18
·20
·22
·24
·26
·28
·30
·32
·34
·36
εp = 2 ln(do/d)

Fig. 47

Position of maximum triaxiallity

Neubers plastically relaxed solution

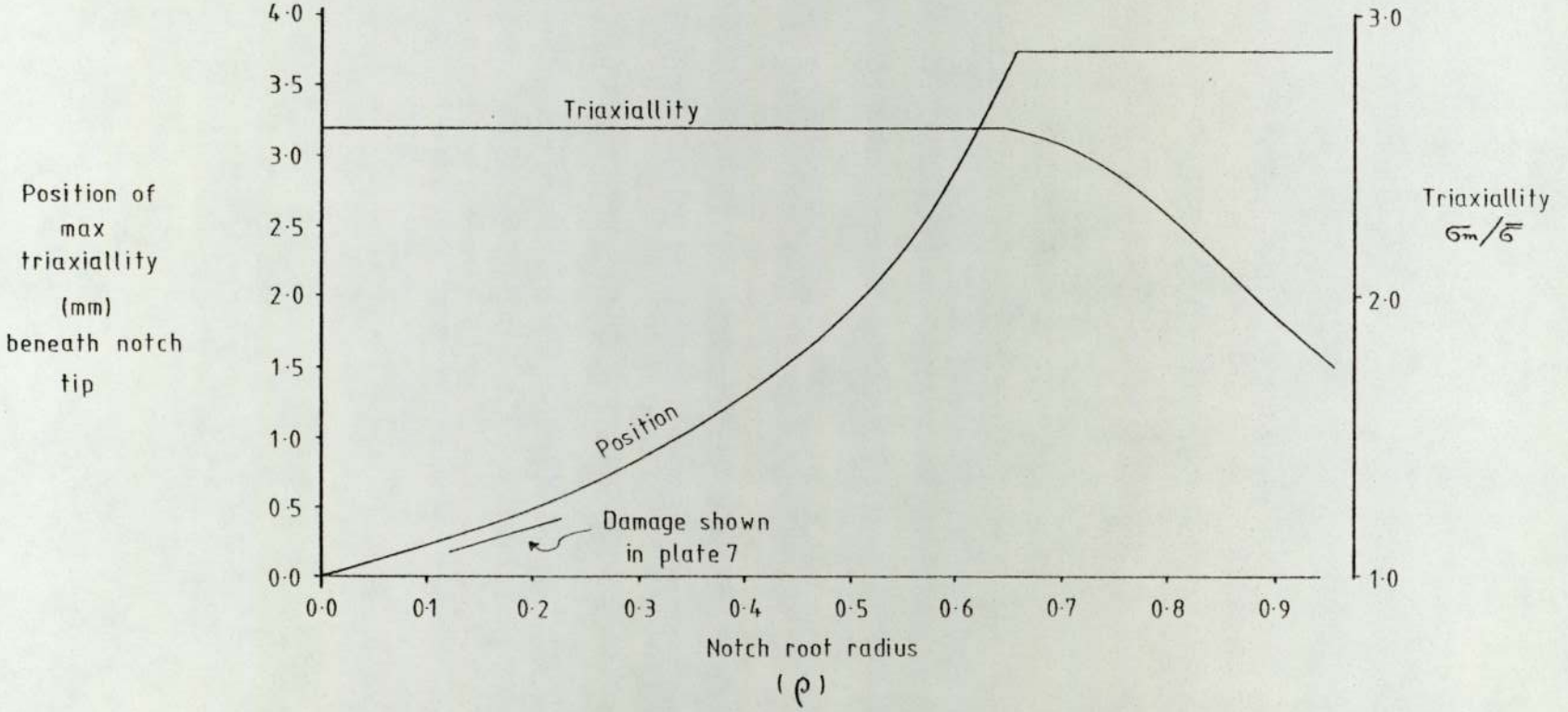

TABLE 1a

Stress strain data for mild steel multi notch specimen

Notch	$\bar{\varepsilon}_p$ $2\ln(d_o/d)$	σ N/mm^2
1	0.172	625
2	0.108	586
3	0.100	551
4	0.091	532
5	0.077	518
6	0.070	496
7	0.050	501
8	0.045	489
9	0.041	476
10	0.036	450
11	0.025	441
12	0.000	---

TABLE 1b

Stress strain data for H1 multi notch specimens.

Notch	$\overline{\varepsilon}_p$ $2\ln(do/d)$	ρ (mm)	σ N/mm^2
0	0.000	0.125	---
1	0.021	0.155	415
2	0.038	0.180	448
3	0.059	0.205	521
4	0.073	0.225	519
5	0.097	0.245	588
6	0.106	0.255	602
7	0.119	0.265	607
8	0.125	0.270	638
9	0.144	0.320	656
10	0.185	0.355	681
11	0.210	0.405	736
12	0.350	0.500	865

TABLE 1c

Stress strain data for H2 multi notch specimens

Notch	$\bar{\varepsilon}_p$ $2\ln(d_o/d)$	ρ (mm)	σ N/mm^2
1	0.216	0.370	963
2	0.135	0.275	873
3	0.129	0.255	827
4	0.119	0.230	795
5	0.073	0.200	765
6	0.039	0.185	706
7	0.106	0.240	817
8	0.092	0.220	797
9	0.070	0.195	748
10	0.054	0.180	713
11	0.029	0.160	678
12	0.000	0.125	---

TABLE 1d

Stress strain data for H3 multi notch specimen

Notch	$\bar{\varepsilon}_p$ $2\ln(do/d)$	ρ (mm)	σ N/mm^2
1	0.329	0.450	944
2	0.124	0.275	775
3	0.160	0.300	731
4	0.090	0.205	715
5	0.069	0.175	701
6	0.055	0.150	683
7	0.118	0.245	749
8	0.099	0.220	718
9	0.078	0.200	711
10	0.048	0.170	638
11	0.027	0.135	602
12	0.000	0.125	---

TABLE 1e

Stress strain data for H1 - 30 multi notch specimens

Notch	$\bar{\varepsilon}_p$ $2\ln(d_o/d)$	ρ (mm)	σ N/mm^2
1	0.349	1.010	875
2	0.135	0.743	710
3	0.120	0.697	682
4	0.104	0.668	659
5	0.104	0.653	640
6	0.097	0.642	618
7	0.081	0.628	582
8	0.072	0.601	538
9	0.056	0.565	507
10	0.048	0.545	491
11	0.031	0.505	444
12	0.000	0.425	---

TABLE 1f

Stress strain data for H2 - 30 multi notch specimens

Notch	$\bar{\varepsilon}_p$ · $2\ln(d_o/d)$	ρ (mm)	σ N/mm^2
1	0.080	0.650	788
2	0.088	0.675	777
3	0.088	0.665	743
4	0.105	0.710	741
5	0.064	0.585	697
6	0.050	0.550	671
7	0.198	0.905	931
8	0.126	0.760	854
9	0.111	0.725	823
10	0.102	0.705	781
11	0.084	0.655	748
12	0.072	0.620	727

TABLE 1g

Stress strain data for H3 - 30 multi notch specimens

Notch	$\bar{\varepsilon}_p$ $2\ln(do/d)$	ρ (mm)	σ N/mm^2
1	0.288	0.895	872
2	0.148	0.740	732
3	0.108	0.695	693
4	0.080	0.645	657
5	0.066	0.620	630
6	0.063	0.605	620
7	0.186	0.800	785
8	0.156	0.760	770
9	0.117	0.705	708
10	0.101	0.680	682
11	0.074	0.625	628
12	0.052	0.585	561

TABLE 2a

Marerial Mild steel

Notch	$\overline{\varepsilon}_p$ 2ln(do/d)	A.N.N.D. (μm)
1	0.171	4.96
2	0.108	14.3
3	0.100	15.50
4	0.091	17.17
5	0.077	19.16
6	0.070	18.60
7	0.050	22.0
8	0.045	23.80
9	0.041	26.23
10	0.036	28.62
11	0.025	29.50
12	0.000	30.20

$$A.N.N.D. = 31.5 - 158.9\,\varepsilon_p$$

TABLE 2b

Mareria1 - H1

Notch	ε_p 2ln(do/d)	A.N.N.D. (μm)
0	0.000	15.15
1	0.021	14.45
2	0.038	14.56
3	0.059	14.17
4	0.073	13.63
5	0.097	13.52
6	0.106	13.48
7	0.119	13.44
8	0.125	13.22
9	0.144	12.79
10	0.185	11.70
11	0.210	11.43
12	0.350	9.77

$$A.N.N.D. = 15.01 - 15.63\,\varepsilon_p$$

TABLE 2c

Material - H2

Notch	ε_p 2ln(do/d)	A.N.N.D. (μm)
1	0.216	8.00
2	0.135	11.07
3	0.129	11.24
4	0.119	11.80
5	0.073	13.18
6	0.039	14.44
7	0.106	12.03
8	0.092	12.42
9	0.080	13.63
10	0.045	14.12
11	0.029	15.03
12	0.000	16.10

$$A.N.N.D. = 16.04 - 37.22\ \varepsilon_p$$

TABLE 2d

Material - H3

Notch	$\bar{\varepsilon}_p$ 2ln(do/d)	A.N.N.D. (μm)
1	0.329	7.04
2	0.124	9.15
3	0.160	8.99
4	0.090	9.48
5	0.069	9.84
6	0.055	10.26
7	0.118	9.23
8	0.098	9.58
9	0.078	9.64
10	0.048	9.87
11	0.027	10.34
12	0.000	10.61

$$A.N.N.D. = 10.54 - 10.66\,\bar{\varepsilon}_p$$

TABLE 2e

Material H1-30

Notch	ε_p $2\ln(do/d)$	A.N.N.D. (μm)
1	0.349	9.99
2	0.135	12.24
3	0.120	12.44
4	0.140	13.23
5	0.140	13.27
6	0.097	13.36
7	0.081	13.68
8	0.072	13.43
9	0.056	14.03
10	0.048	14.21
11	0.031	13.98
12	0.000	14.90

$$A.N.N.D. = 14.62 - 13.97\ \varepsilon_p$$

TABLE 2f

Material H2-30

Notch	ε_p $2\ln(do/d)$	A.N.N.D. (μm)
1	0.080	12.89
2	0.088	12.55
3	0.088	12.30
4	0.105	12.05
5	0.064	13.50
6	0.050	13.73
7	0.198	8.88
8	0.126	11.24
9	0.111	11,72
10	0.102	12.17
11	0.084	12.91
12	0.072	13.66

$$A.N.N.D. = 15.64 - 34.16\ \varepsilon_p$$

TABLE 2g

Material H3-30

Notch	ε_p 2ln(do/d)	A.N.N.D. (μm)
1	0.288	7.55
2	0.148	8.90
3	0.108	8.99
4	0.080	9.54
5	0.066	9.62
6	0.063	9.83
7	0.186	8.65
8	0.156	8.74
9	0.117	9.29
10	0.101	9.64
11	0.074	9.70
12	0.052	9.88

$$A.N.N.D. = 10.36 - 9.78\,\varepsilon_p$$

TABLE 3a

Material H1

Notch	ε_p $2\ln(d_o/d)$	Void Dia. Range (μm)
0	0.000	0.519 - 0.688
1	0.021	0.447 - 0.695
2	0.038	0.509 - 0.703
3	0.059	0.446 - 0.680
4	0.073	0.514 - 0.713
5	0.097	0.522 - 0.729
6	0.160	0.458 - 0.733
7	0.119	0.504 - 0.720
8	0.125	0.482 - 0.753
9	0.144	0.490 - 0.788
10	0.185	0.482 - 0.856
11	0.210	0.496 - 0.863
12	0.350	0.502 - 1.255

TABLE 3b

Material H2

Notch	ε_p $2\ln(d_o/\dot{d})$	Viod Dia. Range (um)
1	0.216	0.321 - 0.833
2	0.135	0.288 - 0.582
3	0.129	0.304 - 0.515
4	0.119	0.282 - 0.500
5	0.073	0.280 - 0.430
6	0.039	0.327 - 0.402
7	0.106	0.306 - 0.494
8	0.092	0.316 - 0.445
9	0.070	0.297 - 0.458
10	0.054	0.315 - 0.410
11	0.029	0.329 - 0.395
12	0.000	0.315 - 0.390

TABLE 3c

Material H3

Notch	ε_p 2ln(do/d)	Void Dia. Range (μm)
1	0.329	0.272 - 1.083
2	0.124	0.308 - 0.572
3	0.160	0.280 - 0.615
4	0.090	0.293 - 0.515
5	0.069	0.327 - 0.505
6	0.055	0.307 - 0.510
7	0.118	0.307 - 0.557
8	0.095	0.305 - 0.536
9	0.078	0.318 - 0.523
10	0.048	0.271 - 0.501
11	0.027	0.298 - 0.491
12	0.000	0.305 - 0.475

TABLE 3d

Material H1 - 30

Notch	ε_p $2\ln(d_o/d)$	Void Dia. Range (μm)
1	0.349	0.503 - 1.033
2	0.135	0.515 - 0.725
3	0.120	0.482 - 0.708
4	0.104	0.513 - 0.702
5	0.104	0.429 - 0.675
6	0.097	0.510 - 0.691
7	0.081	0.527 - 0.675
8	0.072	0.588 - 0.700
9	0.056	0.503 - 0.666
10	0.048	0.521 - 0.652
11	0.031	0.529 - 0.666
12	0.000	0.482 - 0.665

TABLE 3e

Material H2 - 30

Notch	ε_p 2ln(do/d)	Void Dia. Range (μm)
1	0.080	0.326 - 0.433
2	0.088	0.329 - 0.441
3	0.088	0.295 - 0.416
4	0.105	0.297 - 0.449
5	0.064	0.286 - 0.416
6	0.050	0.311 - 0.400
7	0.198	0.292 - 0.610
8	0.126	0.322 - 0.503
9	0.111	0.271 - 0.458
10	0.102	0.301 - 0.449
11	0.084	0.302 - 0.424
12	0.072	0.328 - 0.441

TABLE 3f

Material H3 - 30

Notch	ε_p 2ln(do/d)	Void Dia. Range (μm)
1	0.288	0.322 - 0.758
2	0.148	0.313 - 0.558
3	0.108	0.280 - 0.533
4	0.080	0.274 - 0.501
5	0.066	0.323 - 0.516
6	0.063	0.278 - 0.491
7	0.186	0.302 - 0.603
8	0.156	0.317 - 0.575
9	0.117	0.292 - 0.525
10	0.101	0.293 - 0.520
11	0.074	0.321 - 0.502
12	0.052	0.289 - 0.496

TABLE 4

Uniaxial Tensile Data

Material	Yield Stress (N/mm^2)	U.T.S. (N/mm^2)	Strain to Failure ln(l/lo)
H 1	278	462	0.28
H 2	365	601	0.22
H 3	326	510	0.24
BS 4360 50 D	349	601	0.20

TABLE 5

Impact Results (Charpy)

Material	Impact Resistance (Joules at 20°C)	
H 1	208	
	236	218
	212	
H 2	136	
	126	
	147	139
	148	
H 3	242	
	244	
	220	240
	236	
	262	

TABLE 5 (cont.)

Material		Impact Resistance (Joules at 20°C)
BS 4360 50D		
	3*	256
	2*	80
	1*	43
	1*	40

** 3*, 2*, 1* refer to the notch orientations with respect to the rolling direction of the original plate.

Notch 3 is in the short transverse direction

Notch 2 is in the long transverse direction

Notch 1 is in the longditudinal ditection

(see plate 8)

TABLE 6

Single circumferentially notched bar with varying notch profiles.

Notch	ρ (mm)	ε_ρ $2\ln(d_o/d)$	$\sigma_m/\bar{\sigma}$
S 05	0.15	0.118	2.92
S 10	0.19	0.116	2.71
S 15	0.23	0.132	2.53
S 20	0.39	0.138	2.10
S 30	0.55	0.160	1.81
S 40	1.02	0.200	1.37
S 50	1.10	0.206	1.32
S 100	2.50	0.292	1.25
S 150	3.25	0.376	1.11
S 250	5.70	0.482	0.84

TABLE 7

Carbide diameters

Material	Min. Dia (µm)	Max. Dia (µm)
H 1	0.438	0.716
H 2	0.276	0.462
H 3	0.278	0.533

Plate 1

Multi-notch tensile specimen

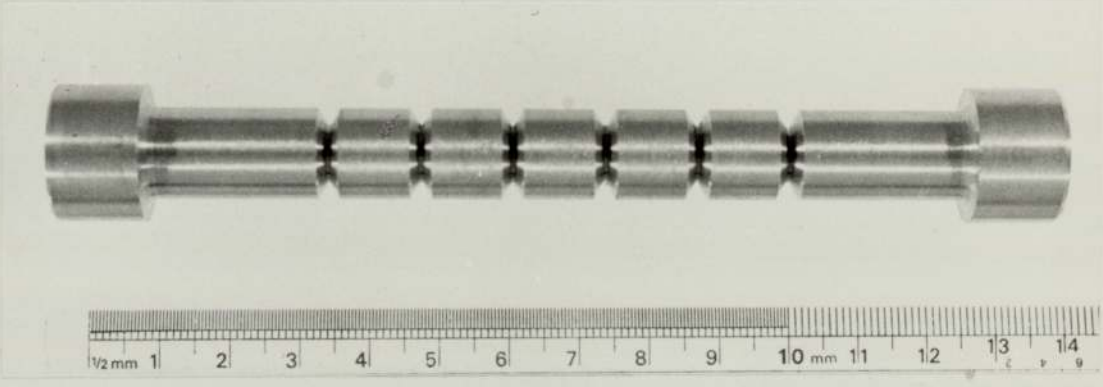

Plate 2

X 200

Parallel bar at fracture

Plate 3

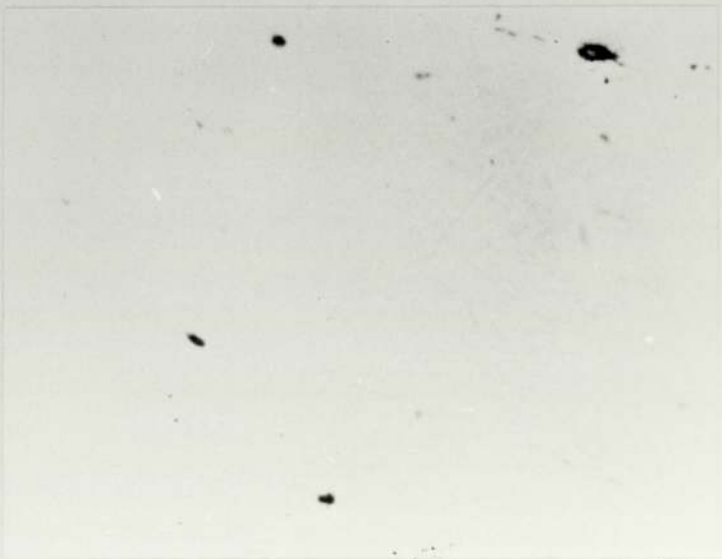

X 200

Parallel bar just before fracture

Plate 4

Single notch fracture surface

X 625

Plate 5

Multi-notch fracture surface

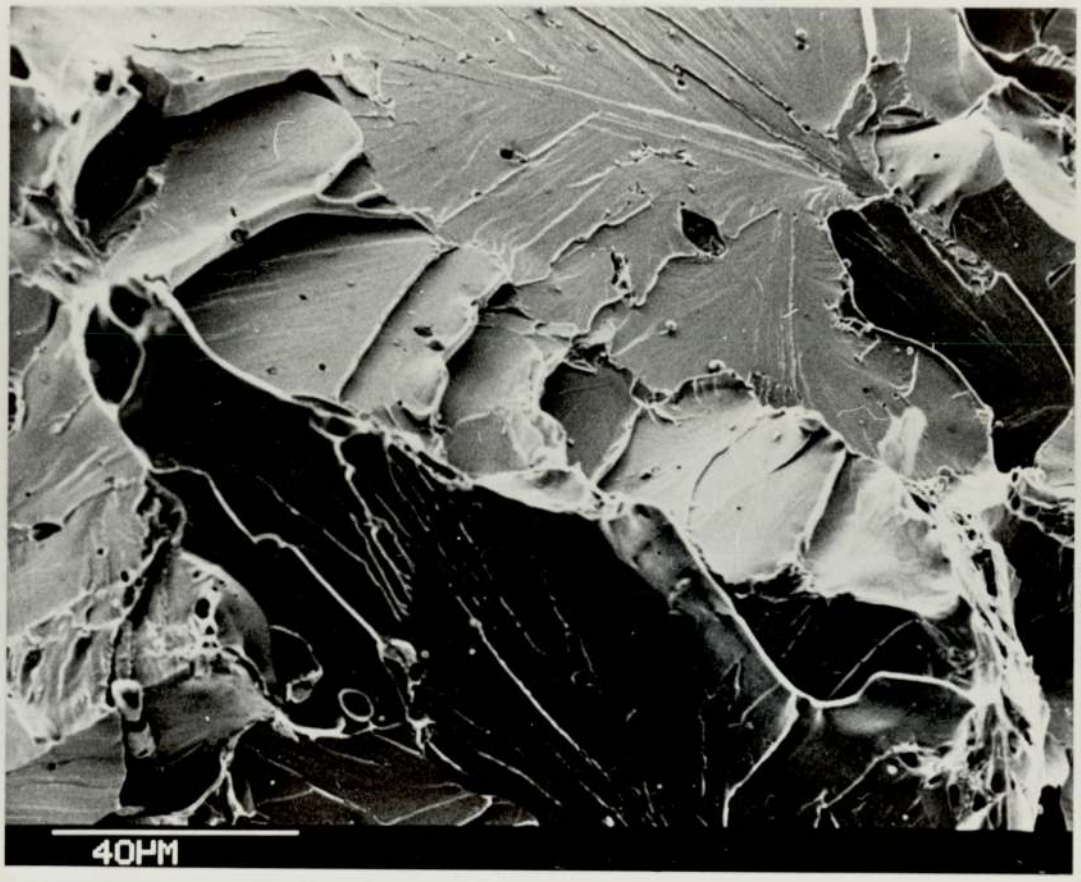

X 850

Plate 6

Notch damage H3-5

X 500

Before fracture initiation

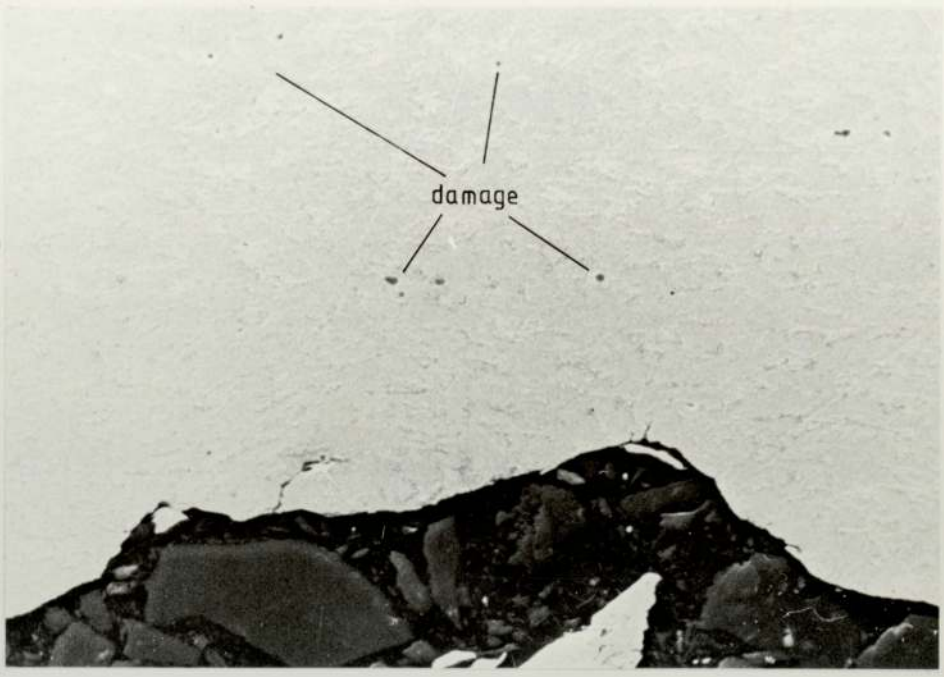

X 500

After initiation

X 500

"50 D" impact fracture surface

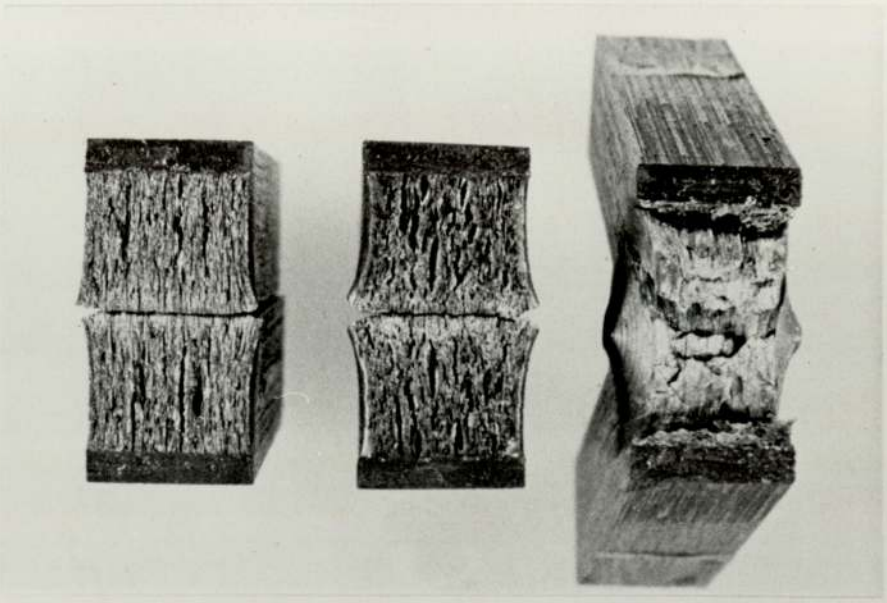

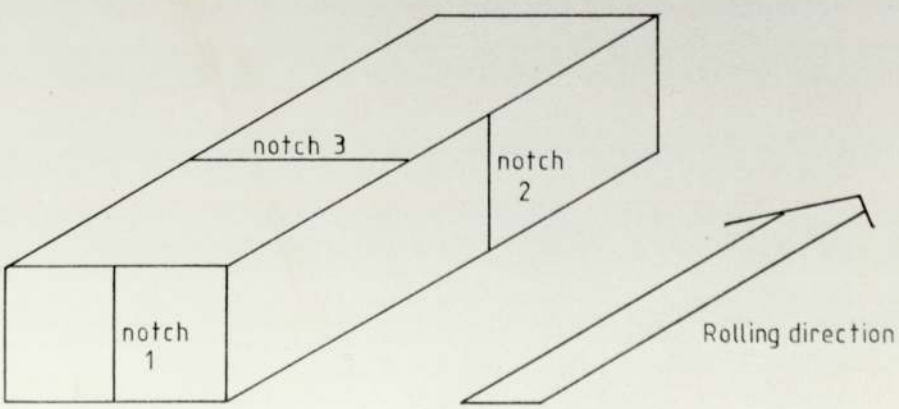

Plate 9

"50 D" notched bar fracture

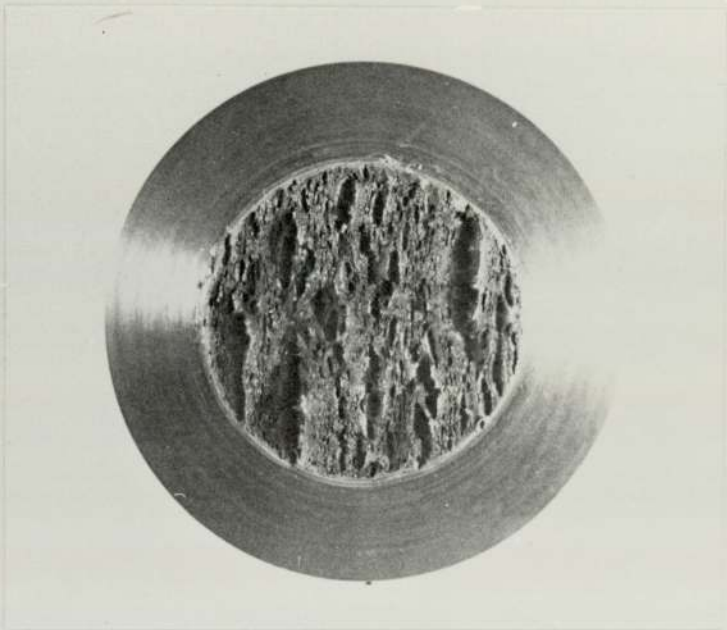

X 5

Plate 10

Strain concentration beneath a notch

X 50

Direction of tension

3 point bend fracture surface

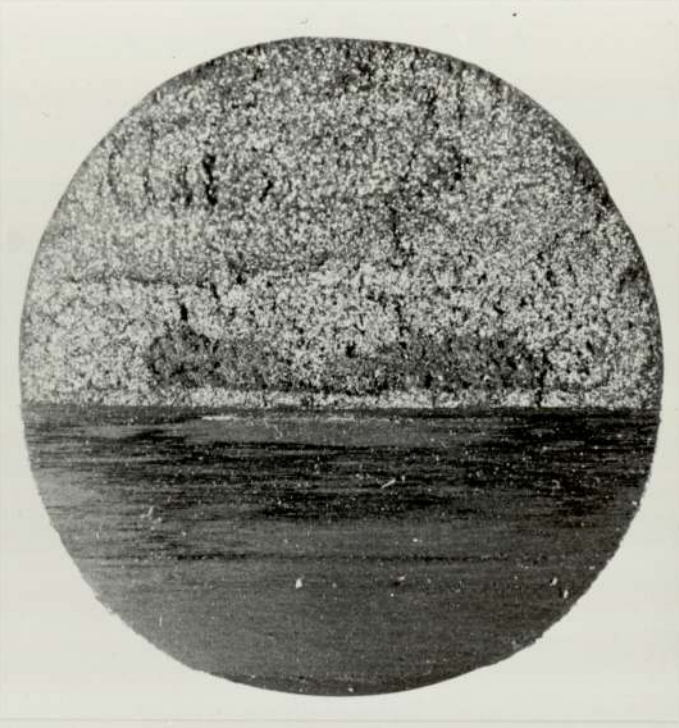

X 3

Plate 12

H1

X 30K

H2

X 30K

H3

X 30K